REPUBLIC OF TÜRKİYE
ADANA ALPARSLAN TÜRKEŞ SCIENCE AND TECHNOLOGY UNIVERSITY

GRADUATE SCHOOL
AERONAUTICAL AND SPACE SCIENCES DEPARTMENT

INVESTIGATION OF ICE ACCRETION EFFECTS ON AERODYNAMIC PERFORMANCE OF NACA 2415 AIRFOIL AT LOW REYNOLDS NUMBER

REMZİ CAN YILMAZ

M.Sc.

ADANA 2024

REPUBLIC OF TÜRKİYE
ADANA ALPARSLAN TÜRKEŞ SCIENCE AND TECHNOLOGY UNIVERSITY

GRADUATE SCHOOL
AERONAUTICAL AND SPACE SCIENCES DEPARTMENT

INVESTIGATION OF ICE ACCRETION EFFECTS ON AERODYNAMIC PERFORMANCE OF NACA 2415 AIRFOIL AT LOW REYNOLDS NUMBER

REMZİ CAN YILMAZ

M.Sc.

THESIS ADVISOR
ASST. PROF. DR. HÜRREM AKBIYIK

ADANA, 2024

ÖZET

DÜŞÜK REYNOLDS SAYISINDA BUZ BİRİKİM ETKİSİNİN NACA 2415 KANAT PROFİLİNİN AERODİNAMİK PERFORMANSINA ETKİSİNİN ARAŞTIRILMASI

Remzi Can YILMAZ

Yüksek Lisans, Havacılık ve Uzay Mühendisliği Anabilim Dalı

Danışman: Dr. Öğr. Üyesi Hürrem AKBIYIK

Ağustos 2024, 75 sayfa

Bu tez, üç farklı buz birikiminin NACA 2415 kanat profilinin aerodinamik performansı üzerindeki etkilerini incelemektedir. Buzlanma ortamları, buzlanma türleri, buzlanmanın kanat profili ve uçak bileşenleri üzerindeki etkileri ve buzlanma önleme ve buz çözme teknikleri hakkında genel bilgiler verilmektedir. $Re=1.2\times10^5$'te, ana kanat profilinin yanı sıra glaze buzlanma, rime buzlanma ve horn buzlanma oluşmuş kanat profilleri için deneyler gerçekleştirilmiştir. Bu çalışma için kuvvet ve hız ölçümleri ile yağ ve duman-tel akış görselleştirme teknikleri uygulanmıştır. Kuvvet ölçümleri için seçilen hücum açısı -7° ile 23° arasında değişmektedir. Ayrıca kuvvet ölçümleri sonuçlarından hız ölçümleri ve akış görselleştirme deneyleri için 0°, 4°, 8°, 13°, 14°, 17° ve 20° olmak üzere yedi farklı hücum açısı seçilmiştir. Sonuçlar, buzla birleşen kanat profillerinin C_{Lmax} değerinin beklendiği gibi azaldığını gösterdi. Maksimum kaldırma katsayısında GIA, RIA ve HIA modellerinde sırasıyla %20, %23 ve %88 oranında azalma gözlendi. GIA, RIA ve HIA kanat profilleri için $\alpha = 0°$'de sürükleme katsayılarındaki artış sırasıyla %14, %4 ve %307 idi. Stall sonrası GIA kanat profilinin kaldırma katsayısında ani bir artış gözlemlendi. Ayrıca hız ölçümlerinde GIA, RIA ve ana kanat profilleri için çift tepe davranışı kaydedilmiştir.

Anahtar Kelimeler: buz oluşumu, horn buzlanma, glaze buzlanma, rime buzlanma, aerodinamik performans

ABSTRACT

INVESTIGATION OF ICE ACCRETION EFFECTS ON AERODYNAMIC PERFORMANCE OF NACA 2415 AIRFOIL AT LOW REYNOLDS NUMBER

Remzi Can YILMAZ
M.Sc., Department of Aeronautical and Space Sciences
Supervisor: Asst. Prof. Dr. Hürrem AKBIYIK
August 2024, 75 pages

This thesis examines the effects of three distinct ice accumulations on the aerodynamic performance of the NACA 2415 airfoil. A brief discussion is provided of icing environments, icing types and the icing effects on the airfoil and also on the aircraft components. Besides, some necessary information is provided for icing prevention (anti-icing) and de-icing techniques. The experiments are carried out for the base airfoil as well as glaze, rime, and horn ice accumulated airfoils at $Re=1.2\times10^5$. For this study, force and velocity measurements are taken. Additionally, the oil and smoke-wire flow visualization techniques are also performed. The selected range of angle of attack for force measurements is defined as -7° to 23°. Additionally, considering the results of force measurements, seven distinct angles of attack values including 0°, 4°, 8°, 13°, 14°, 17° and 20° are chosen for velocity measurements and flow visualization experiments. Results showed that, C_{Lmax} of ice accreted airfoils are decreased as expected. 20%, 23% and 88% of decrease in maximum lift coefficient is observed in the GIA, RIA and HIA models, respectively. An increase in drag coefficients at $\alpha = 0°$ for the GIA, RIA and HIA airfoils is observed to be around 14%, 4% and 307%, respectively. A sudden increase in lift coefficient of the GIA airfoil is observed at post-stall. Moreover, a double-peak behavior is noted for the GIA, RIA airfoil and also for base airfoil in velocity measurements.

Keywords: ice accretion, horn ice, glaze ice, rime ice, aerodynamic performance

Dedication

To all researches who willing to study in this field.

ACKNOWLEDGEMENTS

I would like to thank my respected supervisor, Asst. Prof. Dr. Hürrem AKBIYIK, from the Faculty of Aeronautics and Astronautics, Alparslan Türkeş Science and Technology University, whose worthy guidance, and professional attitude are appreciable in completing this thesis. It was a great privilege and honor to work and study under his guidance. He pushed me along this road and gave me the impression that I could always do better. Words alone cannot express my thanks to him for his supports.

I would like to thank my esteemed colleagues Prof. Dr. Yahya Erkan AKANSU and Res. Asst. Mahi Bilge BİLGİN, Res. Asst. Beyza Betül TANRIKULU and colleagues in my department for their supports in the preparation of this thesis. I am also thankful to my friends Erçin LEVENT, Kartal KOÇDER, Sarp ŞIRA and Ayhan ASLAN for keeping me motivated throughtout this journey.

I am grateful for my parents whose constant love and support keep me motivated and confident. I would like to thank my father Özcan YILMAZ, my mother Nimet BALİ, my brother Rüzgar Baran YILMAZ who always supported me during my studies. My accomplishments and successes were possible because they believed in me.

TABLE OF CONTENTS

ÖZET **i**

ABSTRACT **ii**

Dedication **iii**

TABLE OF CONTENTS **v**

LIST OF FIGURES **vii**

LIST OF TABLES **x**

LIST OF ABBREVIATIONS **xi**

LIST OF SYMBOLS **xii**

1. INTRODUCTION **1**

1.1. Aerodynamic Performances 1

1.2. Problems During Flight 2

1.3. Effects of Icing on Aircraft 3

1.4. Icing Environment 4

1.4.1 Icing in Clouds 4

1.4.2 Icing Associated with Frontal Systems 6

1.5. Types of Icings 7

1.5.1 Glaze Ice 8

1.5.2 Rime Ice 9

1.5.3 Horn (Mixed) Ice 10

1.6. Harms of Icing on Aircraft 11

1.6.1 Nose 11

1.6.2 Powerplant 12

1.6.2.1 Nacelle 13

1.6.2.2 Engine 13

1.6.3 Measurement Devices 14

1.6.4 Airfoil 15

1.7. Solution to Icing Problems on Aircraft 15

1.7.1 Passive Anti-Icing and Deicing Systems 16
1.7.2 Active Anti-Icing and Deicing Systems 18
1.8. Realistic Approach for Icing Effects on Airfoil Aerodynamic Performance 19
2. LITERATURE REVIEW 21
2.1. Wind Turbines 21
2.2. Airfoils 24
2.3. UAVs 27
3. MATERIALS AND METHODS 33
3.1. Experimental Setup 33
3.1.1 Airfoil Selection 35
3.1.2 Production of Test Models 35
3.1.3 Force Measurement System 38
3.1.4 Flow Visualization 40
3.1.4.1 TiO_2 Based Surface Flow Visualization Technique 41
3.1.4.2 Smoke-Wire Flow Visualization Technique 42
3.1.5 Velocity Measurement System 43
3.1.6 Uncertainty Analysis and Repeatability 44
3.1.7 Blockage and Aspect Ratios 44
4. RESULTS AND DISCUSSIONS 45
5. CONCLUSIONS 68
6. FUTURE WORKS AND RECOMMENDATIONS 70
REFERENCES 71
APPENDIX 1

LIST OF FIGURES

Figure 1. Cumulus and stratus cloud forms [5] 5
Figure 2. Icing with fronts [6] 7
Figure 3. The temperature range associated with aircraft icing ranges from -40 to 0°C [6]..... 8
Figure 4. Clear or glaze ice forming around the leading edge of the wing [6] 9
Figure 5. Glaze or clear ice accumulation on the surface of airfoil 9
Figure 6. Rime ice accumulation on the surface of the airfoil 10
Figure 7. Horn ice contamination on the surface of the airfoil 10
Figure 8. Example of thin ice ridges forward of the pitot probes [11] 11
Figure 9. Rime ice accumulated on the fuselage nose [6] 12
Figure 10. Ice accretion in the engine inlet [13] 13
Figure 11. Ice accumulation on engine fan blades [15] 14
Figure 12. Icing on a Pitot tube [16] 15
Figure 13. Black paint on the blades of HAWT [26] 16
Figure 14. Superhydrophobic coating on airfoil [28] 17
Figure 15. Diagram showing the process of the anti-icing system using engine bleed air through a piccolo tube in a wing [39] 18
Figure 16. Sketch of a DBD plasma actuator [36] 19
Figure 17. Icing experiment setup 20
Figure 18. Ice shapes from icing experiments from left to right; (a) glaze ice, (b) rime ice, and (c) horn ice shapes at 0° attack angle 20
Figure 19. Ice accumulated on the blades at the end of the tests: (a) test 1, view from the pressure side; (b) test 2, view from the suction side; (c) test 2, view from the pressure side; (d) test 3, view from the pressure side [44] 21
Figure 20. Ice accreated blade profiles at the end of tests: (a) test 4, view from pressure side; (b) test 5, side view and from pressure side; (c) test 6, view from suction side; (d) test 6, view from pressure side [44] 22
Figure 21. Impacts of thickness and airfoil profile on ice profile [45] 23
Figure 22. Snapshots of the dynamic ice accumulation process under various icing circumstances on the pressure side of the DU96-W-180 airfoil. (a) rime ice accumulated airfoil; (b) mixed ice accumulated airfoil; (c) glaze ice accumulated airfoil; (d) zoomed-in snaps [46] 24

Figure 23. Cast and smoothed ice shapes [49] 25
Figure 24. Effects of ice casting on the aerodynamic performance of test models with Ma = 0.21 and Re=7.5×10^6 [49]........ 26
Figure 25. Photographs and drawings of ice shapes 290 and 296 [50] 27
Figure 26. Predicted ice shape over the test models for Re=5×10^4, drop size is 20 μm and icing duration is 5 min (a) −5°C air temperature and 1.0 g/m^3 of LWC, (b) −5°C air temperature and of 1.5 g/m^3 LWC, (c) −5°C air temperature and 2.0 g/m^3 LWC, (d) −3°C air temperature and 1.0 g/m^3 LWC, (e) −2°C air temperature and 1.0 g/m^3 LWC [56] 29
Figure 27. Prediction of ice accretion on the IM wing for 49.1 m/s of airspeed, AoA of 0°, drop size is 25 μm, and −2°C air temperature at three different spanwise locations: (a) 80% of the semispan, (b) 50% of the semispan, and (c) 20% of the semispan from the airfoil root [57].. 30
Figure 28. (a) Ice shapes obtained from the experimental data and (b) ice shapes from LEWICE [58] 31
Figure 29. Comparison of the experimental and numerical results of the lift and drag coefficients against AoA at a Reynolds number of 4×10^5 for ice shapes from LEWICE [58]32
Figure 30. Open suction low-speed wind tunnel in Niğde Ömer Halisdemir University 33
Figure 31. Traverse system, rotary unit, and load cell 34
Figure 32. MiniCTA software to adjust the angle of attack of the test models........ 34
Figure 33. Vertically placed test model in the wind tunnel test section........ 35
Figure 34. a) NACA2415 base airfoil, b) glaze ice accumulated airfoil, c) rime ice accumulated airfoil, and d) horn ice accumulated airfoil 36
Figure 35. Creality Ender S1 3D printer and its software interface 36
Figure 36. ATI DAQ Software for calibrating force data 38
Figure 37. (a) Schematic of the force measurement setup and (b) test model in the wind tunnel test section 39
Figure 38. Open suction low-speed wind tunnel for flow visualization and velocity measurement experiments 40
Figure 39. From left to right; titanium dioxide powder, oleic acid, and SAE 30 pump oil 42
Figure 40. Smoke-wire flow visualization setup 43
Figure 41. C_L vs. AoA graph for three repeated runs of the base model and literature 45
Figure 42. Drag coefficients of base model and literature versus angle of attack 46
Figure 43. Average L/D ratio vs. AoA of the base model........ 46

Figure 44. Lift coefficients of glaze ice accumulated airfoil and base airfoil against the AoA 47
Figure 45. C_D of the GIA and base models versus AoA 48
Figure 46. L/D ratios of the base and GIA airfoils to the attack angle 48
Figure 47. C_L vs. α graph of the RIA and base models 49
Figure 48. C_D vs. angle of attack for the RIA and base models 50
Figure 49. L/D ratio vs. attack angle of the RIA and base airfoils... 50
Figure 50. Lift coefficients of the HIA and base models against attack angle........................ 51
Figure 51. The drag coefficients of the HIA and base models against attack angle 52
Figure 52. Lift-to-drag ratios of the HIA and base airfoils to AoA 52
Figure 53. Smoke-wire experiments of the base model at different attack angles starting from (a) 0°, (b) 4°, (c) 8°, (d) 13°, (e) 14°, (f) 17°, and (g) 20°.. 53
Figure 54. Smoke-wire experiments of the GIA model at different attack angles starting from (a) 0°, (b) 4°, (c) 8°, (d) 13°, (e) 14°, (f) 17°, and (g) 20°.. 54
Figure 55. Photographs of smoke-wire experiments of the RIA model at different attack angles starting from (a) 0°, (b) 4°, (c) 8°, (d) 13°, (e) 14°, (f) 17°, and (g) 20° 55
Figure 56. Smoke-wire experiments of the HIA model at different attack angles starting from (a) 0°, (b) 4°, (c) 8°, (d) 13°, (e) 14°, (f) 17°, and (g) 20°.. 56
Figure 57. Wake profile of the test models at an angle of attack of 0° 57
Figure 58. Wake profile of the test models at 4° attack angle.. 57
Figure 59. Wake profile of the test models at 8° attack angle.. 58
Figure 60. Wake profile of the test models at 13° angle of attack 59
Figure 61. Wake profile of the test models at 14° angle of attack 60
Figure 62. Wake profile of the test models at 17° angle of attack 61
Figure 63. Wake profile of the test models at a 20° angle of attack 62
Figure 64. Oil flow visualization results of the baseline model at α = 8° 62
Figure 65. TiO_2 oil flow visualization of base model at different angles of attack................. 63
Figure 66. TiO_2 oil flow visualization of the GIA model at different attack angles 64
Figure 67. TiO_2 oil flow visualization of HIA model at different attack angles..................... 65
Figure 68. TiO_2 oil flow visualization of the RIA model at different attack angles 66

LIST OF TABLES

Table 1. Operating and geometrical properties of this thesis 37

LIST OF ABBREVIATIONS

A/C	: Aircraft
ADR	: Air data reference
AoA	: Angle of attack
AR	: Aspect ratio
C_D	: Drag coefficient
C_L	: Lift coefficient
C_{Lmax}	: Maximum lift coefficient
CTA	: Constant Temperature Anemometer
DBD	: Dielectric barrier discharge
GA	: General aviation
GIA	: Glaze ice accumulated
HAWT	: Horizontal axis wind turbine
HIA	: Horn ice accumulated
LE	: Leading edge
LSB	: Laminar separation bubble
LWC	: Liquid water content
L/D	: Lift-to-drag ratio
Ma	: Mach number
NLF	: Natural laminar flow
Re	: Reynolds number
RIA	: Rime ice accumulated
SLD	: Supercooled large droplets
TE	: Trailing edge
UAV	: Unmanned aerial vehicle

LIST OF SYMBOLS

α	: Angle of attack
α_{stall}	: Stall angle
C	: Celcius
F	: Fahrenheit
^{o}	: Degree
ρ	: Density
μ	: Dynamic viscosity
μm	: Micrometer
u	: Uncertainty
U_o	: Free stream velocity
U_∞	: Free stream velocity

1. INTRODUCTION

1.1. Aerodynamic Performances

Aircraft performance is one of the key aspects in aircraft (A/C) design since it is a measure of the capability of the A/C to perform a specified mission. Tasks related to the flight path, as well as tasks that require control, stability and handling can all be categorized as flight performance. In the early years of aviation, generating sufficient lift for an aircraft was a significant performance issue that was resolved by employing multi-wing arrangements on aircraft. Furthermore, by switching from thin to thick airfoils, the ongoing lift problem was resolved and adequate stability and controllability for flying were attained. Consequently, when the fundamental problems of flying were solved, aircraft designers turned their attention to improve aircraft performance. Significant improvements in aircraft performance were made possible by advancements in all areas of aircraft design, such as aerodynamics, propulsion, and structures. One of the key components of continuous efforts to improve aircraft performance is drag reduction. Moreover, a significant factor in drag reduction is the decrease in airfoil drag. The development of airfoils and aircraft in the early days of aviation was mostly dependent on trial and error. The starting of 1920s saw the beginning of organized and methodical airfoil development which was mostly through experimental methods and techniques. In the following years, Tollmien and Schlichting developed the stability hypothesis that demonstrates a connection between the pressure gradient and stability of laminar boundary layer. Tollmien and Schlichting's hypothesis provided a theoretical foundation for the creation of natural laminar flow (NLF) airfoils, which have noticeably lower airfoil drag.

Laminar airfoils have demonstrated their potential to reduce drag in a number of applications and areas. Studies have shown that a relatively smaller friction drag was observed in the laminar boundary layer when compared to the turbulent boundary layer. Nevertheless, in addition to free-stream turbulence, the laminar boundary layer is susceptible to the effects of vibration, noise, and surface roughness. Over the decades, some of the reports have shown that a number of gliders and aircraft have suffered a loss in glide performance in turbulent air. Since many general aviation (GA) and unmanned aerial vehicles (UAV) frequently operate under turbulent atmospheric conditions, this conclusion necessitates further investigation. Furthermore, atmospheric turbulence can affect an aircraft flying at high altitudes, because it can also be observed in or near jet streams. Additionally, previous studies have shown that one of the significant concerns in aviation is the impact of severe atmospheric turbulence or gusts on aircraft.

The lift-to-drag ratio (L/D) is a measure of aerodynamic performance. Using L/D, a decrease in lift or increase in drag, as well as a combination of both can indicate a loss of aerodynamic performance. Surface roughness is one of the important aspects in laminar flow principles since it effects the laminar boundary layer and causes a laminar-turbulent transition that leads to an increase in drag. Thus, in particular, surface contamination by snow, frost, insects or raindrops poses a risk factor for the NLF airfoils. Moreover, the aerodynamic performance of airfoils is severely affected by icing, which causes geometrical modifications on the airfoil.

1.2. Problems During Flight

An aircraft's operational performance is affected by the atmosphere as well as other factors like air density, runway conditions, rain, icing, frost, and consistent wind. While the wind is the most major influencing factor in terms of range, air density, wind and runway condition all have a considerable impact on takeoff and landing performance. Although, tailwinds can be an issue during takeoff and landing, they can also be advantageous since less thrust is required, resulting in less fuel consumption. Conversely, headwinds can cause aircraft to consume more fuel, especially if they are stronger than expected.

Temperature is an atmospheric condition that affects the aircraft performance as well as the oil and hydraulic fluid of aircraft. Oil and hydraulic fluids can become viscous under extreme cold conditions, which impairs their performance. In extreme heat scenarios, these fluids may overheat or evaporate. Moreover, in cold weather aircraft provide more lift, and engines are more efficient since cold air is denser. Conversely, in hot weather, the air is less dense; therefore, aircraft produce less lift and engine efficiency is reduced.

Humidity is another factor that can affect the performance and structure of aircraft. When metal components of aircraft are exposed to high moisture levels in the air, rust and corrosion can form. If this process is not carefully monitored and managed with, it can cause permanent harm to the components. An increase in the humidity in the air makes it less dense, which might affect aircraft performance at critical takeoff and landing conditions.

Rain is one of the conditions that can affect the flight performance and structure of an A/C. Rain affects the physical structure of aircraft. Furthermore, the constant rain might cause the metallic components of the airplane to corrode, thus hastening the aging process. Additionaly, rain-soaked runways may reduce the aircraft's tire-to-ground traction. This can pose a challenge for landing since it can take the aircraft longer to stop on the runway, which could result in runway excursions. In terms of aerodynamic performance, water droplets stuck to the wings have the ability to change the wing geometry and disturb the surrounding airflow, which reduces lift generation and increases drag on aircraft.

The aerodynamics of an aircraft can be dramatically changed by ice accumulation on its surface. The wings are the main component of the aircraft in order to generate lift. Ice formation can affect the flow on the wings surface. Consequently, lift generation can be affected, thereby reducing the aerodynamic performance of the aircraft. Aircrafts sometimes have de-icing and anti-icing systems installed to prevent or delay ice buildup on the wings; nevertheless, this adds another level of complication to maintenance procedures during winter. Furthermore, ice and low temperatures may additionally impact the engine performance of the aircraft. Ice can interfere with the precise air-fuel balance that jet engines need to run properly, resulting in power reductions or even engine failure.

1.3. Effects of Icing on Aircraft

Ice accretion on an aircraft in flight causes a loss of aerodynamic efficiency, increase in vibration and thereby reducing the flight safety. Several investigations have been conducted to analyze the effects of ice on airfoil surface and have been presented in various studies. According to these studies, ice accretion affects the weight, lift, and drag forces acting on the airfoil, as well as the pitching moment [1]. One of the first experiments on the impact of ice accretion on the performance of the NACA64150 airfoil was conducted in the Lewis Icing Research Tunnel and was documented by Gray [2]. The most complete of these tests was reported by Gray [2] and Gray and von Glahn [3]. In these tests, well-documented data on ice accretion and airfoil performance were presented for a NACA65A004 airfoil. Lift, drag, and pitching moment changes due to ice accretion were measured using a tunnel balance system.

Gray subsequently, used these data and additional NACA data to create an empirical equation that predicted the rise in drag caused by ice accumulation. After this study, until the present NASA program began in the late 1970s, not much icing research was conducted or published. In order to collect aerodynamic data, testing airfoils with ice accretions experimentally is a challenging task. Icing conditions are difficult to assess while in flight since they change dramatically as the aircraft moves through and out of clouds. Shedding or sublimation frequently takes place after the ice has been gathered before the shape can be documented. It is quite challenging to instrument an airfoil for accurate aerodynamic data collecting under icing conditions, especially during flight, even in the absence of shedding. Although the icing conditions can be carefully regulated in an icing wind tunnel, it might be challenging to operate the instrumentation for precise results. In order to avoid these issues, tests involving simulated ice forms are conducted. The ice shape is typically acquired from an icing wind tunnel or a flight test to simulate the ice. Moreover, it is important to replicate the overall form of the ice accretion as well as the surface roughness.

1.4. Icing Environment

1.4.1 Icing in Clouds

Regulations in the Appendix of FAR 25 require an aircraft to be approved to fly in the stratus clouds with water droplet diameters up to 40 μm and cumulus clouds with droplet diameters up to 50 μm. Although icing in layer clouds is often less severe than in the cumulus clouds, it can still be hazardous if the cloud contains high water content. Moreover, exposure to the icing state can be prolonged due to extensive distribution of stratus clouds in the horizontal plane. If cumulus clouds are embedded in stratus layer, the icing becomes more severe. The temperature range between 0°C and -10°C is where structural icing is most likely to occur. It is still conceivable, although less likely, between -10°C and -20°C. The researchs suggest that icing is strongest close to the summit of stratiform clouds. Typically, icing layers do not extend more than 3000 feet vertically, and even if the aircraft is still in clouds, a mere few thousand feet of altitude change could remove it from the icing conditions [4].

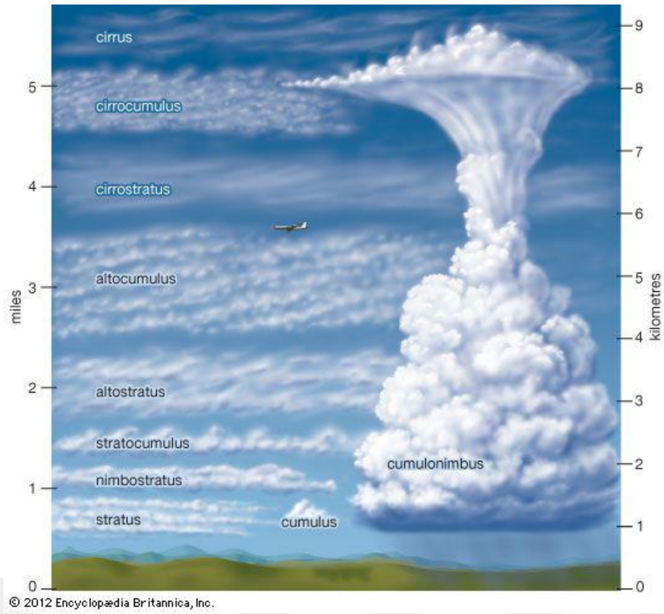

Figure 1. Cumulus and stratus cloud forms [5]

The icing regions in cumulus clouds are long and thin in the horizontal direction. In the upper parts of heavy cumulus clouds that are developing to the mature cumulonimbus stage, severe icing is likely to occur, especially when the temperature is between 0°C and -25°C. However, the cloud's horizontal expanse is constrained, limiting the amount of time that aircraft can be exposed. Compared to stratiform clouds, the zone of potential icing in cumuliform clouds is larger vertically but smaller horizontally. Moreover, icing in cumuliform clouds is more unpredictable since many of the elements that help with icing heavily depend on the stage at which the particular cloud is developing. When it comes to small supercooled, icing intensities can vary from often trace to occasionally light or moderate in cumulus congestus and cumulonimbus. In a mature cumulonimbus, icing is typically limited to updraft regions, whereas in a dissipating thunderstorm, it is restricted to a shallow layer at the freezing level. Icing in cumuliform clouds is usually clear (glaze) to mixed.

The cumulus types include thunderstorms, which have the potential to produce extremely dangerous icing conditions in their thunderhead anvils. High liquid water content (LWC) in orographic and wave clouds can cause ice events with extended exposure periods. Ice particles apperent in cirrus clouds at high, cold altitudes have the potential to be hazardous because they can melt and re-freeze on aerodynamic surfaces. Cloud water droplets are typically 20 micrometers in size; therefore, they are small enough to allow droplets to remain in place even in the presence of relatively small airflows. Since top of the clouds have the highest LWC, they are also most prone to excessive icing. Figure 1 illustrates the clouds described above.

1.4.2 Icing Associated with Frontal Systems

The most common type of aviation icing is cloud icing, though advancing fronts can produce enough moisture to cause an icing hazard. Approximately 5% of the drop in the atmospheric layer between 10 and 200 m consists of supercooled large droplets (SLD). According to the World Meteorological Organisation, a SLD is a droplet with a diameter exceeding 50 microns. Since the cloud structure in frontal regions and regions of intensive low-pressure systems is complicated, it is challenging to accurately simulate frontal icing conditions using an idealized model. Typically, frontal clouds are more prone to ice than different kinds of clouds. In general warm fronts are associated to the largest horizontal area of icing, and cold fronts are linked to the strongest icing. Moreover, warm frontal icing can happen below the frontal surface as well as above it. In the frigid air beneath the front, freezing rain or drizzle frequently causes moderate to severe clear icing. The former scenario is typically seen when the ambient temperature atop of the frontal inversion is above 0°C. In areas where cloud temperatures are below 0°C, icing ahead of the warm frontal region is typically limited to a layer that is less than thickness of 3,000 feet. Research findings suggest that within the range of 100-200 miles ahead of the warm front, there can be a probability of moderate icing, typically mixed icing, or clear icing. Furthermore, this was especially apparent for warm fronts moving quickly and actively. Up to 300 miles in front of the warm front, light rime ice was observed in the altostratus.

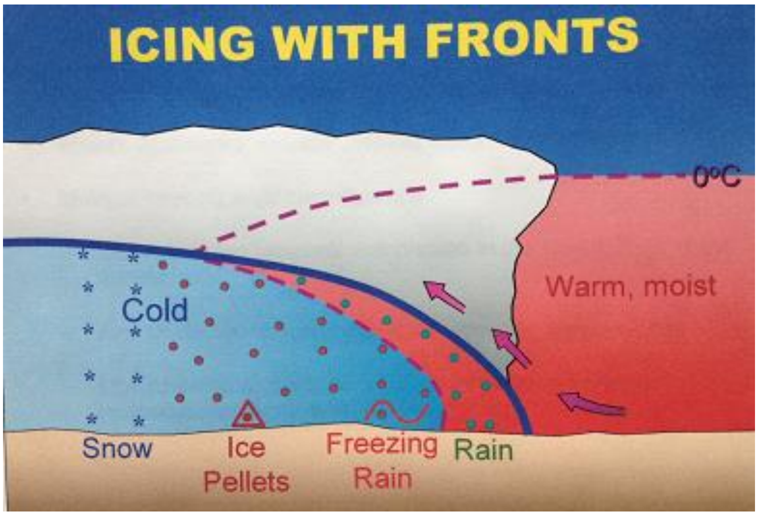

Figure 2. Icing with fronts [6]

Cold front-related icing is typically inconsistent, whereas warm front-related icing is usually widespread. It has a less horizontal extent, and is present in localized regions of moderate icing. Supercooled cumuliform clouds are usually the sole regions with clear ice within 100 miles of the cold front. The concentration of clear ice is typically highest just above the frontal zone. Moreover, the vast layers of supercooled stratocumulus clouds that usually lie behind cold fronts are common places for encountering light ice. Warm front icing is more similar to that found in stratiform clouds of the prevalent affront variety of cold front cloud-shield. Other varieties of frontal icing are those that occur when occluded or stationary fronts resemble either a warm or cold front, based on which type of front is most comparable. Cold, deep, low-pressure regions with widely dispersed frontal systems are often linked to moderate icing conditions.

1.5. Types of Icings

Icing can accumulate on aircraft surfaces while the aircraft is both on the ground and during flight. While the aircraft is on the ground, rain or snow falling on the aircraft surfaces produces some ice types such as snow, slush, clear ice or can be combination of all. During flight, supercooled water droplets in metastable condition inside the clouds causes ice accumulation on aircraft surfaces. When a supercooled water droplet strikes the surface of an aircraft, the impact with the surface breaks the internal stability of the supercooled water droplet and increases its freezing temperature which is known as aerodynamic heating. Additionally, due to aerodynamic and surface adhesion forces, the droplets can collect into a thin film of water and flow back along the aircraft surface [7].

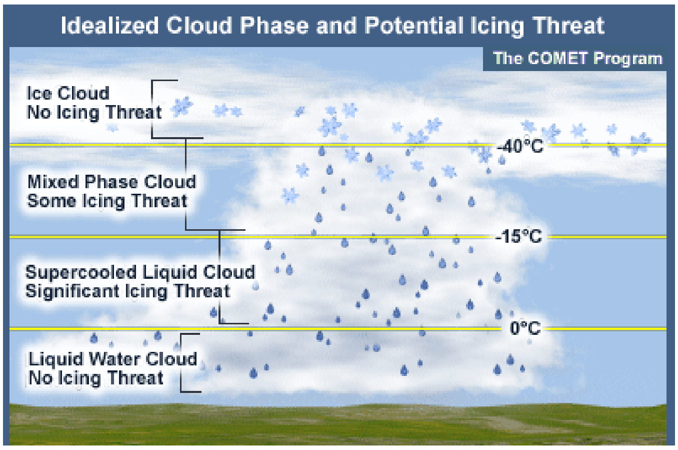

Figure 3. The temperature range associated with aircraft icing ranges from -40 to 0°C [6]

Ice accumulation on aircraft surfaces is generally classified as glaze (clear), rime and mixed (horn) ice [8]. The type and shape of ice that forms on an aircraft surface depends on the atmospheric parameters of temperature, pressure and velocity as well as meteorological parameters of the water droplet diameter, liquid water content, and icing time [9].

1.5.1 Glaze Ice

Glaze or clear ice forms around the aircraft surface between temperatures of -18°C and 0°C when aircraft fly in areas such as freezing rain and cumuliform clouds where a high quantity of large supercooled water droplets are observed. Glaze ice forms when a small amount or no amount of supercooled water droplets freeze on impact. Due to aerodynamic heating, the surface temperature of aircraft increases, and water droplets spread out and combine together before freezing. Hence, no air is trapped in the ice, resulting in transparent solid sheet of glaze (clear) ice with a density of 0.917 kg/m^3 [8].

Figure 4. Clear or glaze ice forming around the leading edge of the wing [6]

Glaze ice affects the aerodynamic performance of an aircraft due to a decrease in lift by altered geometry of the wing camber and destabilization of the flow around the surface, an increase in drag, weight of ice accumulated on the surface, and vibration due to unequal loading around the wings [6]. Increase in exposure time to icing during flight can result in the formation of two glaze ice horns from stagnation point, which causes aerodynamic performance penalties and may result in aircraft stall [7].

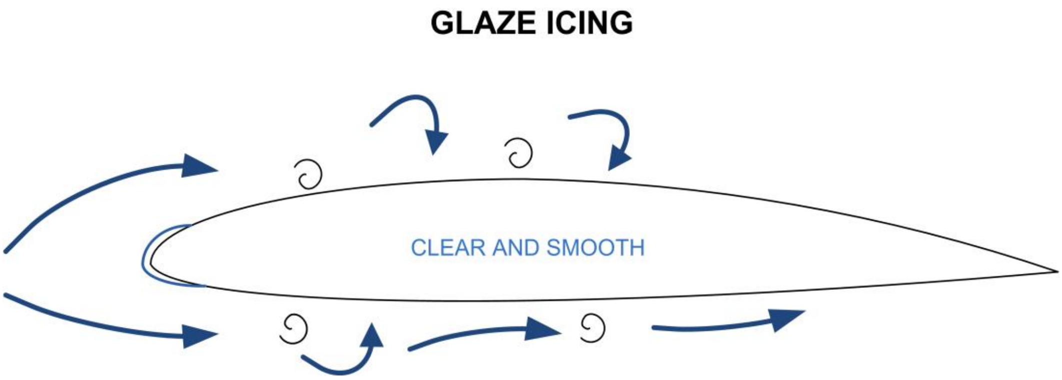

Figure 5. Glaze or clear ice accumulation on the surface of airfoil

1.5.2 Rime Ice

Rime ice is observed at lower temperatures between -40°C and -10°C when supercooled water droplets in stratiform clouds freeze upon impact on the surface without spreading from the point of impact. Consequently, the droplets stay in spherical shape and air is trapped between the surface and the frozen droplets. Hence, rime ice gains its characteristic opaque, milky-white appereance.

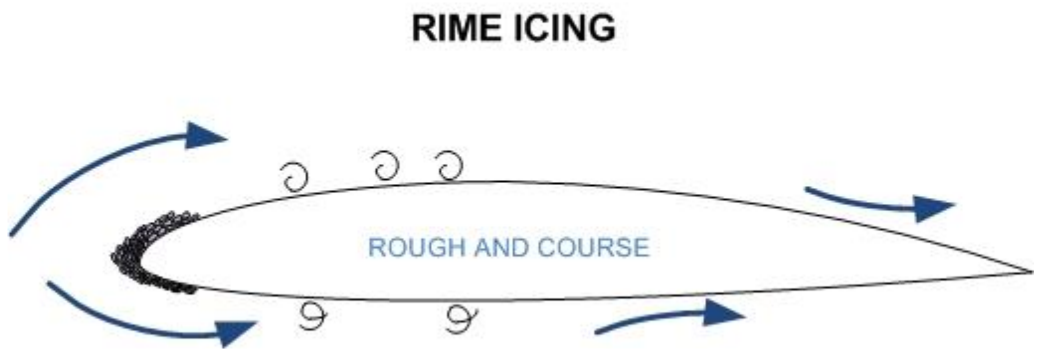

Figure 6. Rime ice accumulation on the surface of the airfoil

Rime ice generally forms around the leading edge (LE) of the wing with a streamlined shape. Rime ice has a rough and coarse surface, which increases the drag acting on the wings due to surface roughness and early boundary-layer transition [1].

1.5.3 Horn (Mixed) Ice

Generally referred to as mixed ice in the literature, horn ice is a mixture of both rime and glaze ice, which is commonly encountered during flight [9]. It is characterized by larger protuberances, known as horns. Moreover, the horn ice exhibits the characteristics of both rime and glaze ice. Glaze ice characteristics are observed at the center of the horn ice, which is surrounded by thin, feather-like shapes known as rime feathers. Horn ice can severly alter the airfoil geometry, causing it to move stagnation point to the ice.

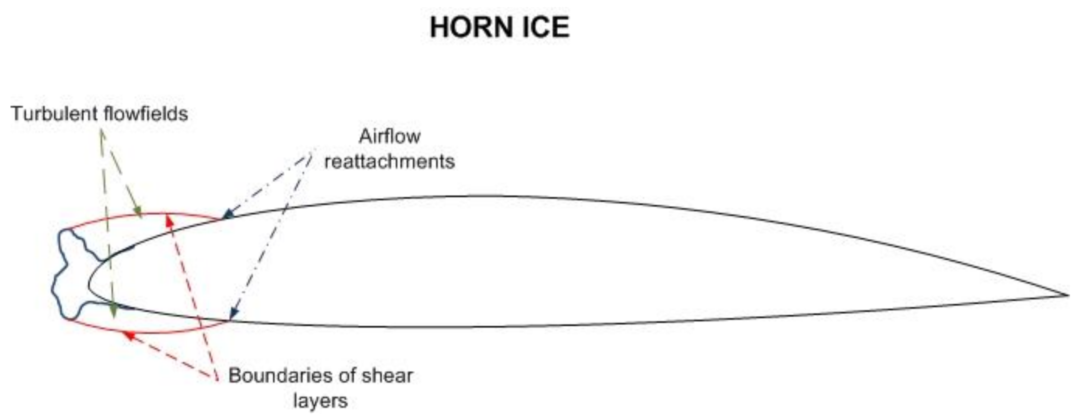

Figure 7. Horn ice contamination on the surface of the airfoil

Downstream of the horn, a large separation bubble can form on the surface of the airfoil and may change the pressure distribution, a decrease in lift, increase in drag, and change in the stall characteristics [10]. Usually, the reattachment of the transitioned turbulent flow due to early boundary-layer transition occurs on the surface of the airfoil at low angles of attack, causing loss of lift as well as significant increase in drag.

1.6. Harms of Icing on Aircraft

Ice accretion can occur at various locations on an aircraft during flight such as the wing leading edge, engine nacelles, propellers, and windshields. Accumulated ice can significantly affect the aerodynamic performance of the aircraft and cause structural damage due to ice shedding [8]. Moreover, the safety of flight may be compromised by the accumulation of ice on non-lifting parts of aircraft, such as nacelles, landing gear, antennae, and probes.

1.6.1 Nose

One of the potential icing problem that can occur on the A/C fuselage nose is ice ridges. Ice accumulation for an extended period of time spent on the ground in cold weather is the primary cause of the ice ridges covering the aircraft’s lower nose fuselage. A study of in-service occurences over the previous 6 reveals that most incidents involving ice ridges occured on the day’s first flight. Events that have been reported also indicate that ice ridges could come loose throughout the flight or might stay fixed to the lower nose fuselage during flight. The air data reference (ADR) of the affected probe or probes may provide airspeed data that are lower than the actual airspeed due to airflow disturbances caused by ice ridges ahead of the pitot probe on the lower nose fuselage.

Figure 8. Example of thin ice ridges forward of the pitot probes [11]

The location, form, and quantity of the ice ridges will determine how they affect the measured airspeed. Moreover, both a large ice ridge and a series of thin ice ridges can have major impacts on airspeed reading. Theoretically, ice ridges may potentially have an impact on static ports or angle of attack (AoA) sensors due to airflow disruption; however, in-service data indicate that there is rarely an impact on AoA readings and static pressures.

Figure 9. Rime ice accumulated on the fuselage nose [6]

1.6.2 Powerplant

Aircraft powerplants are susceptible to damage and/or reduced performance as a result of ice accumulation on engine instruments, icing that causes engine stall and flameout, and disruption of engine flow distribution. In 2020, an aircraft accident caused by ice accumulation on a powerplant occurred in the neighborhood of Bergen, Norway. The DHC8-300 faced severe icing conditions on January 20, and as it approached Bergen, both engines failed sequentially [12]. The engines were restarted by the automatic ignition system, but the aircraft lost all power for a brief period of time. It was determined that ice had formed on the engine air intakes, separated, and either entered the combustion chamber partially melted, resulting in a flameout or sufficiently interfered with airflow into the engine to cause it to stall.

1.6.2.1 *Nacelle*

Ice accumulation on the engine nacelle is one of the main reasons of a decrease in engine performance. The location and kind of the contamination, as well as whether the engines are operating at the time of exposure, determine which part of the engine is impacted. Although ice intake poses a serious risk, airflow interruption due to ice accumulation on the compressor and fan blades can also cause harm, including flameout, engine damage, and thrust loss.

Figure 10. Ice accretion in the engine inlet [13]

Preston and Blackman presented an experimental case to measure the effects of engine cowl icing on aerodynamic performance [14]. Results showed that a 10% increase in drag on the ice acculumated aircraft compared to the clean aircraft.

1.6.2.2 *Engine*

Internal icing issues in reciprocating engines are mainly caused by carburetor icing, as there is small air intake. On the other hand, a huge volume of supercooled water droplets is ingested since gas turbines require a large air intake. Consequently, this can occasionally result in significant icing issues with the fan spinner, inlet guide vanes, front bearing housing of non-fan, first row of compressor vanes and stator blades. Instrumentation for turbine engines measures the pressure and temperature differential through the engine and is positioned toward the forward and aft sections of the engine. Since these instrumental readings are the basis of the power setting, this differential is significant.

Figure 11. Ice accumulation on engine fan blades [15]

In the event that excessive amounts of ice are allowed to accumulate on the fan blades at low thrust levels, excessive ice accretion may cause damage to the blade tips by shedding ice. The above may occur when high thrust is applied later. In addition, engine core damage may result from ice buildup. Ice accumulation on the intake ring has the potential to break off and be ingested by the engine, causing damage that could lead to partial loss of thrust as well as flameout. Ice buildup on the compressor blades can disturb the airflow into the compressor, leading to compressor stall or surge. The safety of flight may be compromised by false flight deck instrument indications caused by ice-contaminated engine probes [12].

1.6.3 Measurement Devices

Ice accumulation in the pitot tube can cause unreliable instrument readings due to reduced ram air pressure. As part of the pitot-static system, the majority of modern aircrafts also feature an external static pressure port. The airspeed, rate of climb, altimeter, and other instruments on the system become less reliable when ice accumulates on the static pressure port. Moreover, ice buildup on the radio antenna may lead to structural distortion, increasing drag, and vibrations that could cause an aircraft’s communications system to malfunction. The radio performance of an aircraft has historically suffered from ice build up on radio antennas. In contrast, no negative impacts of ice development on modern radio equipment and aerials have been reported.

Figure 12. Icing on a Pitot tube [16]

1.6.4 Airfoil

The primary impact of ice accretion on the wing and tail is the decrease in C_{Lmax}; a 40% reduction in the rime ice acculumation is not out of the ordinary. If accreted at a high angle of attack, the glaze ice may actually enhance C_L, but its performance is poor at low attack angles. The particular ice accumulation may also affect the angle of attack for zero lift. Furthermore, this change in the AoA may be caused by the ice form modifying the camber of the airfoil or by the additional roughness thickening of the boundary layer on the surface of the airfoil. The rise in drag force ranges widely, from essentially no increase to increases of 500% or higher in specific situations.

1.7. Solution to Icing Problems on Aircraft

The accumulation of ice on A/C can result in significant aerodynamic penalties or problems in mechanical parts. Thus, ice accretion can affect the safety of flight. Steuernagle et al. stated that ice accretion during flight play a significant role in aircraft accidents due to weather conditions [17]. To prevent or reduce the effects of such important weather induced phenomena, anti-icing and de-icing systems are widely used. Anti-icing denotes as prevention of ice accumulation on the surface of an aircraft during flight whereas the de-icing refers to removal of the acculumated ice on the aircraft surface. The de-icing system is activated after a small amount of ice accumulated on a surface where such ice thickness does not significantly affect the aerodynamic performance. Hence, ice detection on a surface plays a critical role.

One of the ice detection methods uses a probe that vibrates ultrasonically at a nominal resonant frequency. As the ice accumulates on the probe, the mass of ice reduces the resonant frequency. As the frequency drops to a certain value of the ice thickness, the ice detection system actives the de-icing process. Another ice detection method includes optical detectors mounted on the wings and fuselage of the aircraft. Optical ice detectors measure the ice thickness on a surface by amount of light reflected from the surface [18]. Furthermore, anti-icing systems are classified into two categories; passive and active.

1.7.1 Passive Anti-Icing and Deicing Systems

Passive anti-icing systems are mainly used to reduce the power required for anti-icing of surfaces since they require no external energy and are commonly applied to surface such as black paint or coating [18], ice-phobic coatings [19,20], and superhydrophobic coatings [21,22].

Figure 13 shows the black paints on the blades of horizontal axis wind turbine (HAWT). Black paint or coating provides ice protection with an ice-phobic coating by using solar energy to heat the surface during daylight. Although, Laakso et al. [23] reported that black paint can be sufficient when the accretion on surface is light, this method is usually not adequate to prevent icing on the surface [24]. Furthermore, the application of black paint on wind turbine blades may harm the polymer composite material since these materials are sensitive to high surface temperatures [25].

Figure 13. Black paint on the blades of HAWT [26]

Ice-phobic coatings have low ice adhesion, which, in turn, may help remove ice from a surface by reducing the shear force needed. Such coatings allow low quantity of ice to form on the surface that can be shed by overcoming ice-surface adhesion forces with the help of external forces, for example aerodynamic forces or gravity. Anderson and Reich conducted an experimental investigation in a wind tunnel on the performance of ice-phobic coating [19]. Results showed that rather than coating surface, tunnel and cloud conditions are the only parameters that affect the shape and amount of ice accumulated on the surface.

Over the past decades, superhydrophobic coatings have been a topic of interest for anti-icing applications. When applied to an aerodynamic surface, a superhydrophobic coating acts as a water-repellent surface with low liquid water adhesion. Hence, the water droplet that forms on such surfaces had a contact angle greater than 150° and a low contact angle hysteresis smaller than 10°. The droplets stay in spherical form owing to minimal contact area between the surface and the droplets. Furthermore, such droplets may be removed from the surface by shear flow, thus, the accumulation of water on the surface of the airfoil is reduced or prevented. Consequently, freezing of water on the surface is prevented [27]. Kraj and Bibeau conducted qualitative tests to investigate ice accumulation and adhesive forces. Results stated that icephobic and hydrophobic coatings are generally more effective under rime and glaze icing conditions, respectively [21].

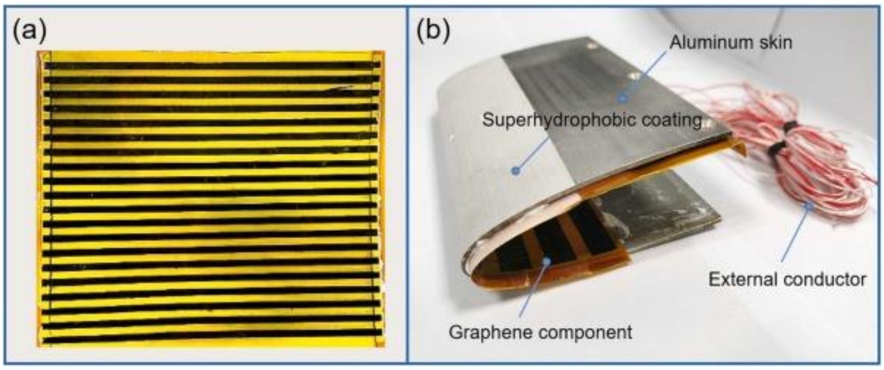

Figure 14. Superhydrophobic coating on airfoil [28]

Although passive anti-icing systems have advantages such as inexepnsive and no energy requirement, many studies have concluded that passive systems alone are not sufficient to solve the icing problems.

1.7.2 Active Anti-Icing and Deicing Systems

In contrast to passive anti-icing systems, active anti-icing system require an external energy supply, such as pneumatic, thermal or chemical supply. Active anti-icing systems include bleed air [29,30], electro-thermal [31-34], DBD plasma actuators [35-37] and pneumatic boots as de-icing systems [38].

Bleed air is a thermal anti-icing and de-icing method in which hot bleed air from engine compressor is used as a warm air supply to prevent or reduce icing on aircraft wing and engine inlets. The hot air from the compressor is diverted to ice accumulated location by interconnecting ductwork.

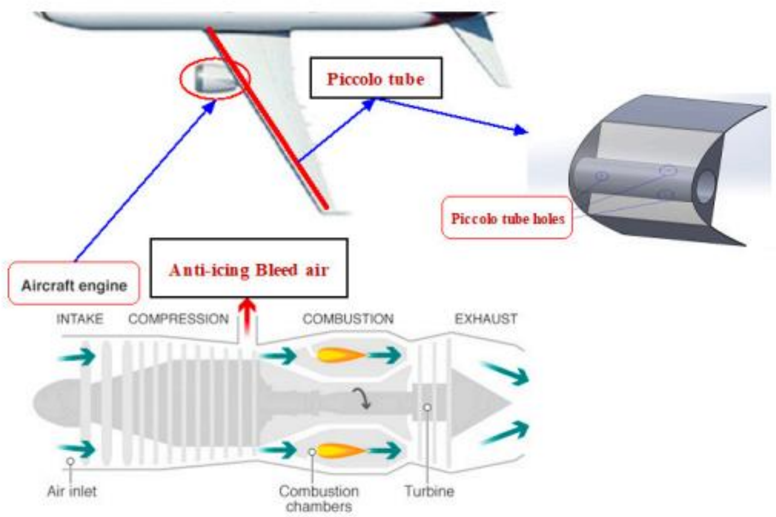

Figure 15. Diagram showing the process of the anti-icing system using engine bleed air through a piccolo tube in a wing [39]

Moreover, piccolo tubes or narrow gap passages are used to transfer thermal energy from hot air. Warm air is discharged from interconnecting ductwork to tubes and passages, where it is transferred to ice accumulated locations [7].

For certain parts of aerial vehicles, such as propellers, nose, rotors and hubs, thermal anti-icing systems are not viable as icing solutions. In such cases, electro-thermal heaters, such as electrothermal pads, can be applied to the surfaces for anti-icing purposes. The application of electrothermal pads can break the bonds between the surface and ice by creating a film of water. Thus, the accumulated ice can be removed by aerodynamic forces.

In recent years, DBD plasma actuators have been extensively used for flow control applications, such as drag reduction, lift augmentation, and flow separation control [40]. The DBD plasma actuators are mainly composed of a thin dielectric layer that separates two metal electrodes, as shown in Figure 16. Recently, researchers have focused on the thermal effects of DBD plasma actuators for use in anti-icing systems. Meng et al. conducted an experimental investigation to confirm the performance of a DBD plasma actuator as an anti-icing system [41]. Furthermore, for short period of time the temperature of gas in the discharge volume was increased to 1000 K in the study of [42].

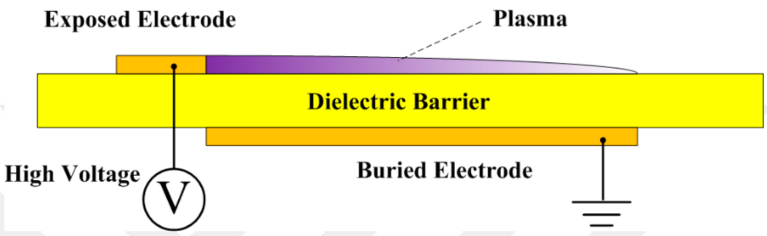

Figure 16. Sketch of a DBD plasma actuator [36]

One of the most commonly used systems for deicing is pneumatic boots. Pneumatic boots can break the bonds between ice and the surface by bending and shearing stresses caused by inflation. Hence, the ice breaks into smaller parts and is removed by aerodynamic forces [43].

1.8. Realistic Approach for Icing Effects on Airfoil Aerodynamic Performance

Aerodynamic performance measurements are occasionally performed in icing tunnels for a number of reasons. The difficulty of covering the entire model with a homogeneous icing cloud inside an icing tunnel, as the homogeneous ice cloud is not as big as the cross-sectional area of the tunnel. In consequence of this, if the airfoil model is semi-span the ice buildups taper off at one end. On the other hand, the ice accumulation on the full-span model tapers off on both ends. Consequently, the ice formations that taper off from the airfoil model are likely to have an impact on force measurement of aerodynamic performance, which are conducted throughout the entirety of the model. Furthermore, the ice and water over the surface of the airfoil model foul the pressure taps, which greatly affects the pressure measurements in the icing tunnel. Turbulence values in an icing tunnel are generally higher than in a wind tunnel. Increased turbulence in the icing tunnel can modify the boundary layer of the flow surrounding the model, thus it affects the airfoil's aerodynamic performance.

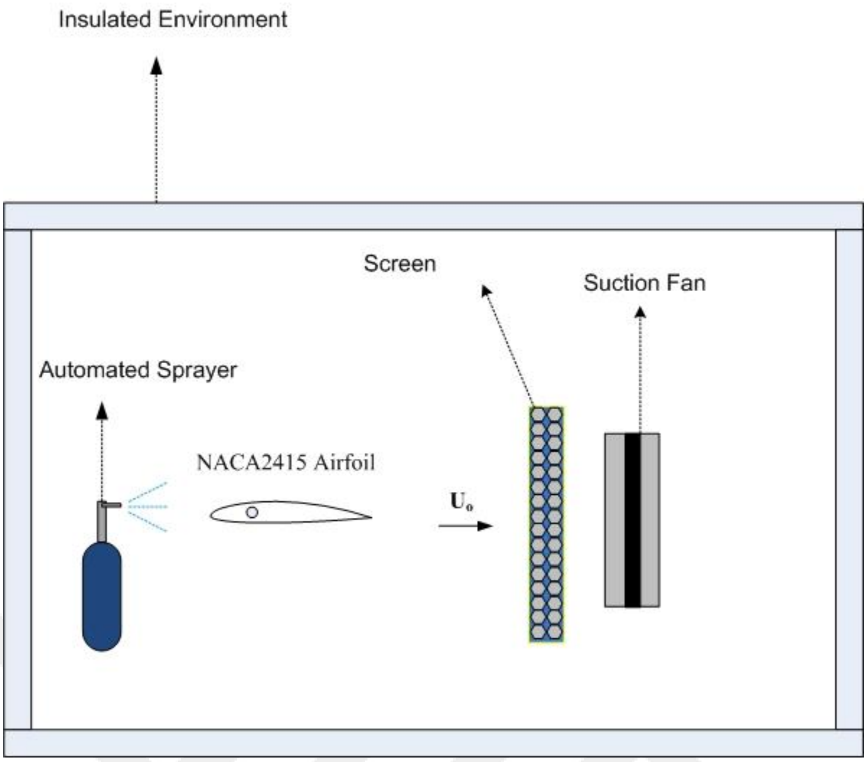

Figure 17. Icing experiment setup

To address these issues, records were made of the ice shapes accreted on the NACA 2415 airfoil, as shown in Figure 18. These ice shapes were 3D-printed and attached to the base airfoil along the entire span. As shown in Figure 17, an ice production system in an insulated environment is presented and used to produce the ice shapes shown in Figure 18. The red shapes in Figure 18 represent smoothed ice accumulations used in the experiments. Other ice formations are partially formed structures.

Figure 18. Ice shapes from icing experiments from left to right; (a) glaze ice, (b) rime ice, and (c) horn ice shapes at 0° attack angle

2. LITERATURE REVIEW

2.1. Wind Turbines

Over the last decades wind turbines have been a topic of interest since wind energy is an alternative source of clean energy. High-potential wing energy sites are generally located on the north side of the Earth, and at these northern locations, problems due to icing are usually encountered [44]. Ice accumulation on wind turbine rotor blades can cause significant aerodynamic performance penalties that lead to a loss generated power or to a complete loss of power production [23]. Moreover, ice accretion can give rise to heavy vibrations due to uneven ice loading over wind turbine blades [25]. Hochart et al. conducted an experimental investigation to evaluate the impact of glaze and rime icing on the aerodynamic performance of NACA 63415 airfoil [44]. The chord and span of the NACA 36415 airfoil were chosen as 0.2 and 0.5 m, respectively.

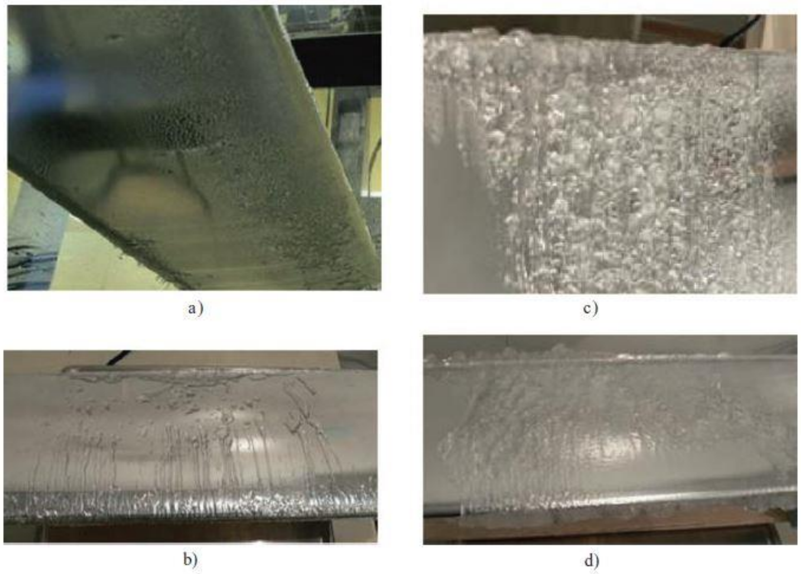

Figure 19. Ice accumulated on the blades at the end of the tests: (a) test 1, view from the pressure side; (b) test 2, view from the suction side; (c) test 2, view from the pressure side; (d) test 3, view from the pressure side [44]

Their results showed that, glaze, and rime ice accumulated mostly on the leading edge and partially on the pressure side of the airfoil. Horn shape observed on the accumulated rime ice, which increased the surface roughness. The total masses of glaze and rime ice accreted on the airfoil surface were 709 and 434 kg, respectively. In terms of total airfoil mass, glaze and rime ice represents the 11% and 6.7% of total airfoil mass, respectively. For both icing cases, lift reduction of 40%. Consequently, an increase in drag and decrease in lift led to a reduction in torque.

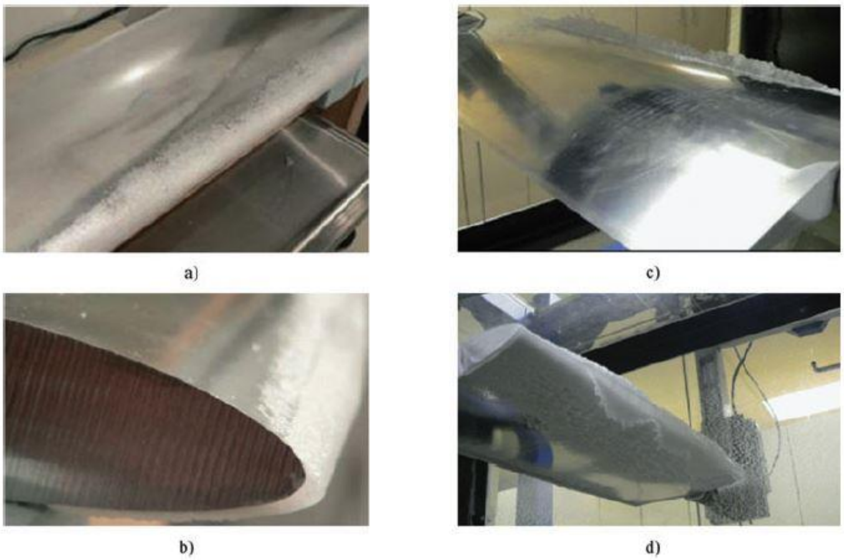

Figure 20. Ice accreated blade profiles at the end of tests: (a) test 4, view from pressure side; (b) test 5, side view and from pressure side; (c) test 6, view from suction side; (d) test 6, view from pressure side [44]

Moreover, this torque reduction was observed to be more significant on the outer third of the rotor blade. The authors suggested that, the heat energy and equipment cost can be reduced by covering the outer third of the blade with a de-icing system while still maintaining sufficient aerodynamic performance. Etemaddar et al. performed a numerical investigation to monitor the effects of ice accumulation on the aerodynamic performance of seven different profiles at Reynolds number of 2×10^6 [45]. The investigated profiles are cylindrical, DU40A17, DU35A17, DU30A17, DU25A17, DU21A17, and NACA64618. Such profiles were selected to show the effects of ice on the different thickness to chord ratio.

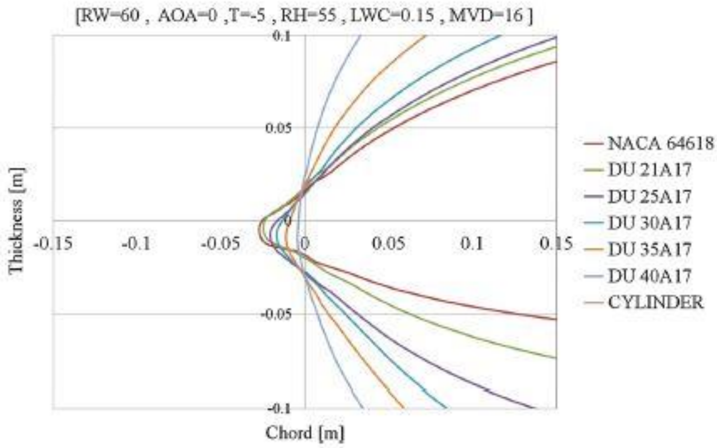

Figure 21. Impacts of thickness and airfoil profile on ice profile [45]

The experimental results indicated that 0.35 thickness to chord ratio suggested as maximum thickness to chord ratio that is prone to icing. The authors stated that any value bigger than such maximum thickness is saved from effects of heavy icing. The aerodynamic performance analysis of the blade profiles showed that the reduction in performance is mainly due to the increase in drag in the linear region of the lift curve. The difference in the lift coefficients of the ice accumulated and clean airfoils increased with increasing AoA. On the other hand, the difference in drag coefficients between the base airfoil and ice accreted airfoil reduces as AoA increases. Another experimental study was performed by Gao et al. to observe the dynamic ice accretion process on the DU96-W-180 airfoil under several icing conditions at -10°C. Three different LWC levels, 0.3 g/m^3, 1.1 g/m^3 and 3.0 g/m^3 represent rime, glaze, and mixed ice conditions, respectively [46]. The airfoil thickness-to-length ratio, chord, and span of the selected airfoil were 0.18, 152.4 mm and 400 mm, respectively. Although Reynolds number of 4.2×10^5 chosed for experiments, the authors stated that such Reynolds number is smaller than of real wind turbine blades. Furthermore, it has been reported that the Reynolds number effect of DU airfoils is relavitely less than that of NACA airfoils.

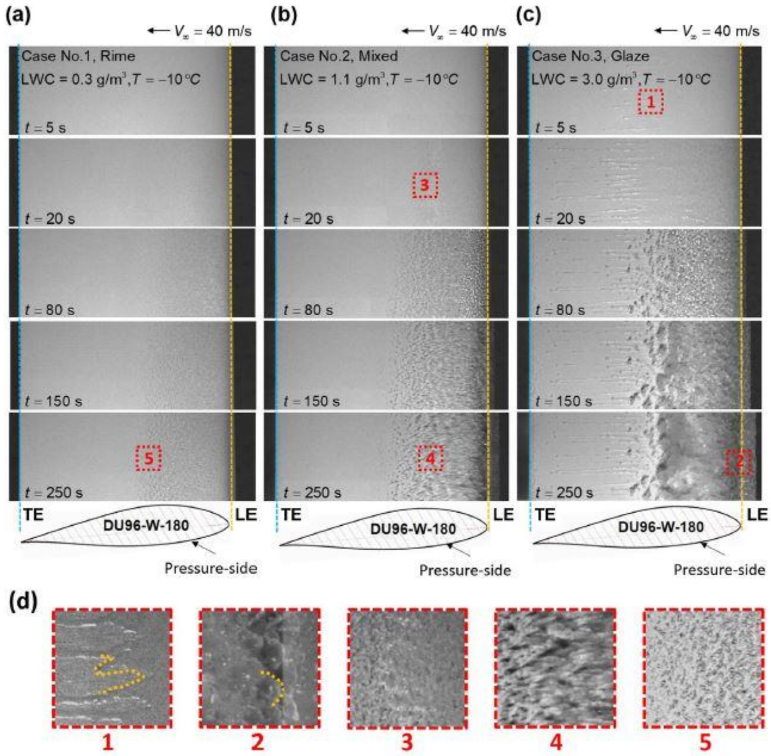

Figure 22. Snapshots of the dynamic ice accumulation process under various icing circumstances on the pressure side of the DU96-W-180 airfoil. (a) rime ice accumulated airfoil; (b) mixed ice accumulated airfoil; (c) glaze ice accumulated airfoil; (d) zoomed-in snaps [46]

The experimental results showed that the life cycle of dynamic ice accretion under rime and glaze ice conditions can be divided into two and three categories, respectively. Furthermore, the ice film length was calculated under both icing conditions. For all three icing conditions, the ice film length covered 40% chord length of the pressure side of the test models. Additionally, under glaze icing, the ice film covers 80% of the chord length of the airfoil. A linear increase in ice thickness was observed during the dynamic ice accretion process.

2.2. Airfoils

Contamination of the aerodynamic surfaces of aircraft such, as tails and wings, as well as inlets, nacelles etc. can cause serious deterioration in the effectiveness aerodynamic performance. Ice accretion on these surfaces is one of the most common contaminations that observed in aviation and can endanger flight safety. Therefore, it is critical to evaluate the effects of icing on the aerodynamic performance of aircraft. Several studies have been conducted to investigate the effects of ice accumulation on the aerodynamic performance of airfoils and aircraft. One of the early investigations into the effects of icing on NACA 0012 airfoil aerodynamics as well as on repeatability of the accumulated ice shape was performed by Shin and Bond at the NASA Lewis Icing Research Tunnel [47]. The airfoil chord and span were determined as 53.34 cm and 1.83 m, respectively, at a fixed AoA of 4°. Experimental results indicated that a -26.11°C, repeatability of the ice shape was very adequate. Also, as the ice shape was altered from glaze to rime ice, the repeatability of this ice shape was improved. Moreover, the authors came to the conclusion that airfoil drag and repeatability of ice shape are unaffected by increases in airspeed or the amount of time that ice accumulates. Another experimental investigation was conducted by Chung and Addy to observe the aerodynamic effects of ice accumulation on the NLF-0414 airfoil [48]. The test airfoil had a span and chord length of 0.91 m both. Maximum lift coefficients of 6 minute glaze ice and 22.5 minute glaze ice were reduced by 35% and 45%, respectively, as confirmed in test results. Additionally, for the two ice cases a reduction in stall angle by 35% and 65% was observed, respectively. Moreover, the authors noted that the impacts of Reynolds number and Mach number on aerodynamic performance are typically mitigated by glaze ice accumulation on the airfoil. Addy et al. conducted an experimental investigation to evaluate the aerodynamic performance of a GLC-305 business jet airfoil affected by icing [49]. The chord and span of airfoil were 91.44 cm (36 in) for both. 4 different ice cases were chosen, depending on the exposure time of the airfoil to icing as well as the angle of attack.

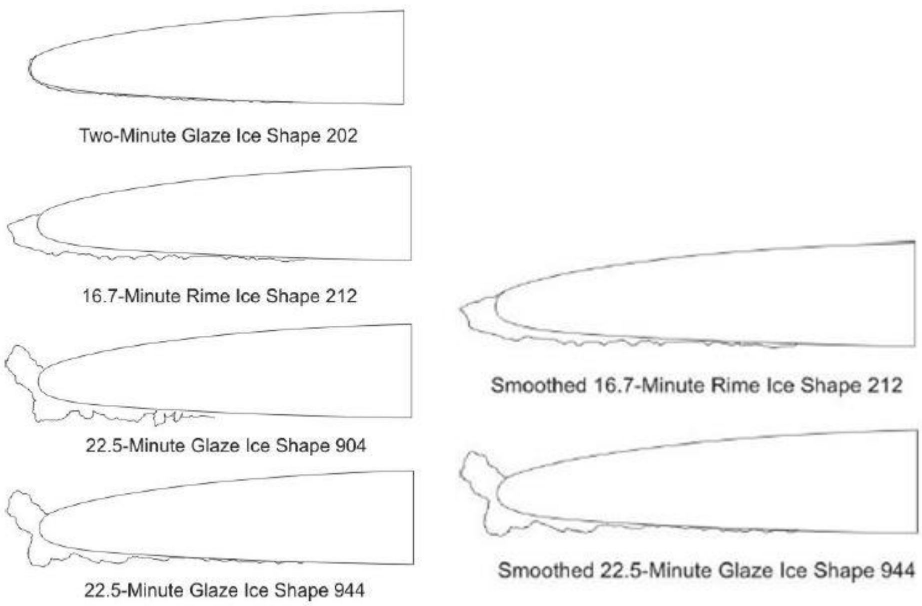

Figure 23. Cast and smoothed ice shapes [49]

For the experiments, both Mach number and Reynolds number ranged from 0.12 to 0.18 and 3.0×10^6 to 10.5×10^6, respectively. Results stated that the 2-minute glaze and 16.7-minute rime ice accumulation cases showed similar lift coefficients and degradation in maximum lift coefficient by 22% at Mach number of 0.21 and Re = 7.5×10^6. Moreover, at the same Ma and Re numbers, two glaze ice cases accumulated in 22.5 minutes with AoAs of 4° and 6° showed almost identical lift coefficients.

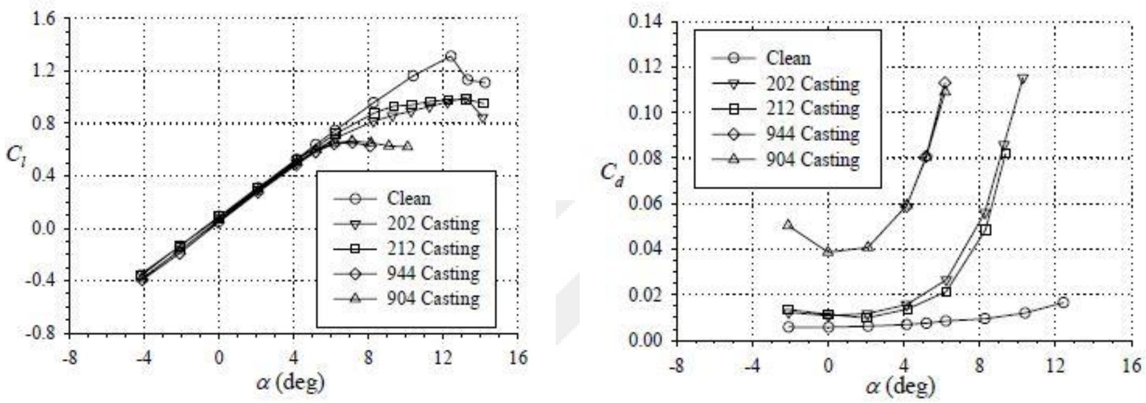

Figure 24. Effects of ice casting on the aerodynamic performance of test models with Ma = 0.21 and Re=7.5×10^6 [49]

A reduction of 48% in the maximum lift coefficient was also observed for these two cases. Broeren et al. carried out an experimental investigation to demonstrate aerodynamic performance penalties due to ice accumulation on the NACA 23012 airfoil [50]. A pneumatic deicer was used to create icing under various cloud conditions in FAR 25 Appendix C at 0° and 4° AoA. Intercycle and residual ice accumulations were created by deicer was made into a mold that later converted into castings for use in experimental tests. The chord and span of airfoil was selected as 0.91 m both. Additionally, the Reynolds number and Mach number was 6.5×10^6 and 0.27 at nominal values, respectively. Moreover, the experimental tests included 4 different icing cases as well as 60- and 80-grit sandpapers that applied on the leading edge of the airfoil.

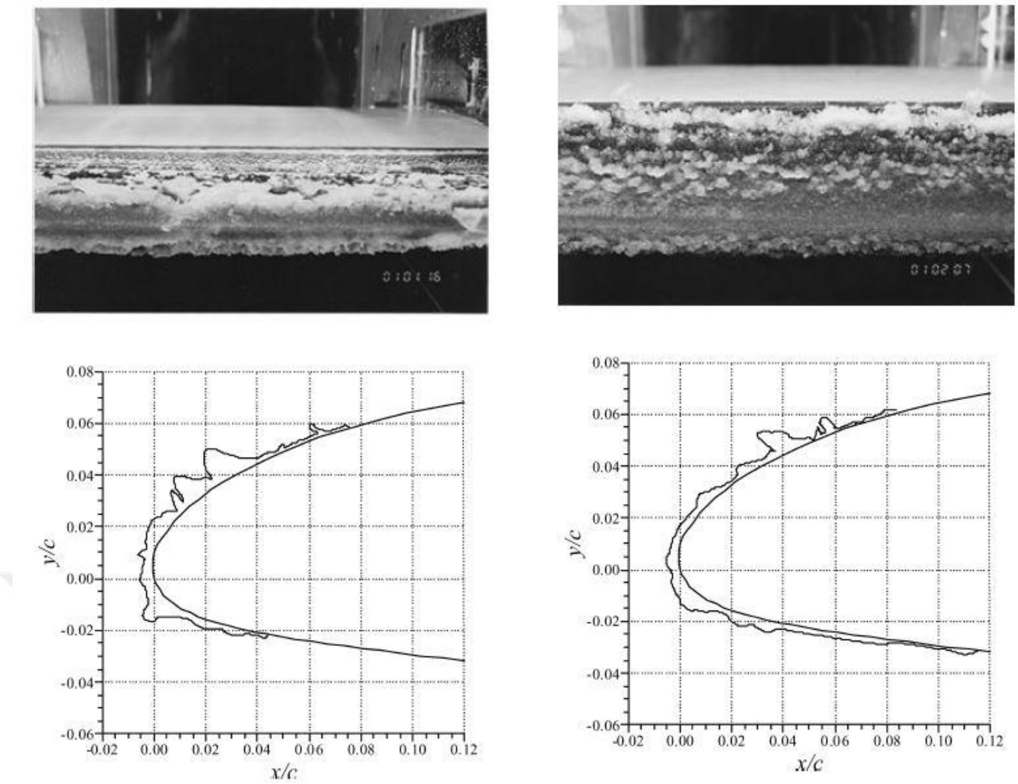

Figure 25. Photographs and drawings of ice shapes 290 and 296 [50]

Results showed that a reduction in the maximum lift coefficient by 60% was observed in comparison with base airfoil to iced airfoil, and the stall angle was reduced from 17° to 9°. Also, ice accumulated airfoil's minimum drag coefficient measured as 0.026 whereas clean airfoil had 0.007. For the sandpaper case, the maximum lift was reduced from 1.8 to 1.2 with a reduction of 33%, and the minimum drag coefficient increased from 0.007 to 0.011.

2.3. UAVs

UAVs have been widely used all around the world in various fields, such as military, defence, and civil aviation, including photography, mapping, surveying, and shadow detection [51]. Especially, in recent years, due to the increase in the popularity of UAVs, the number of studies about UAVs and their aerodynamic performance have substantially increased, demonstrating the capabilities of UAVs in several applications and regions of the world. Moreover, in colder regions of the globe, such as northern regions, potential applications of UAVs include determining the surface temperature over water and ice, measuring sea-ice thickness, and ice reconnaissance [52]. However, because of the weather conditions on this cold regions, UAVs are prone to ice accumulation due to the higher quantity of supercooled water droplets below atmospheric altitudes of 10 km compared to altitudes above 10 km [53]. Although, several UAVs cruise over 10 km, they are exposed to icing layers below 10 km altitude due to takeoff, climb, descend, and landing during flight. Cold weather can affect the battery life of UAVs, resulting in loss of endurance and range [54]. Moreover, UAVs are usually designed to be lightweight; hence, de-icing and anti-icing systems are often not installed, making them prone to ice accretion on their surface. Ice accumulation can cause critical structural problem and aerodynamic performance penalties. Commonly used composite materials in UAVs have lower thermal conductivity and a slower heat transfer rate during solidification which results in water runback on the surface of the UAV and creates a complex ice structures [55]. Avery and Jacob performed a numerical simulation to evaluate low altitude icing conditions on MARIA, a small UAV [10]. They used LEWICE codes to simulate ice accumulation. The cloud modeling was simulated on the Oklahoma State University High Performance Computing Center *Cowboy* supercomputer. The simulation results showed that the high water content increases ice thickness. According to the results, the ice thickness was more sensitive to a decrease in temperature than to an increase in liquid water content. Szilder and McIlwain studied the influence of Reynolds number on the ice accumulation process on the NACA 0012 airfoil [56]. A change in the ice profile was observed from simulation results as surface of the airfoil covered with glaze ice changed to a feathery rime ice profile at water droplet impact locations as the Reynolds number decreased.

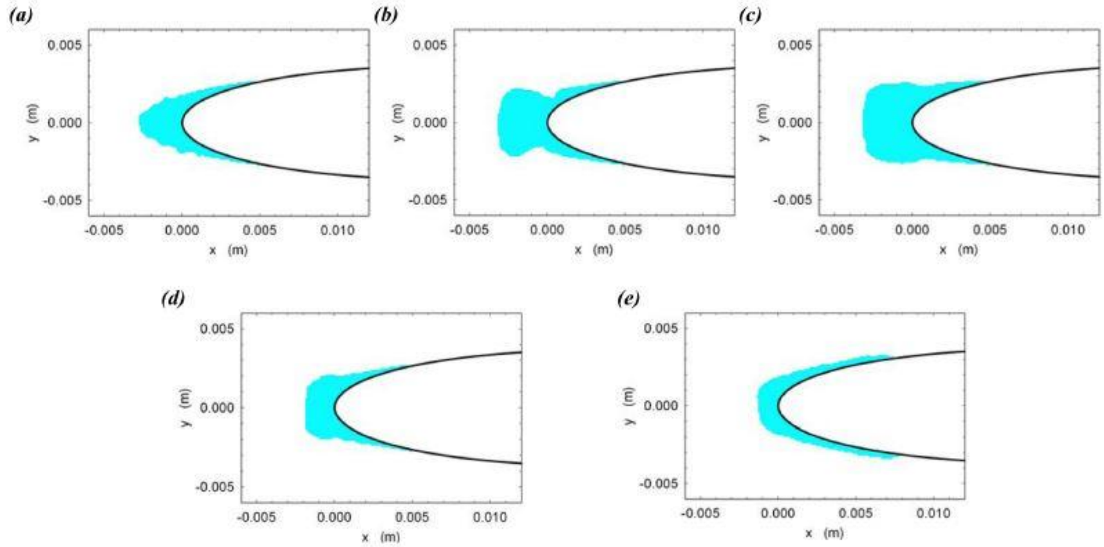

Figure 26. Predicted ice shape over the test models for Re=5×10^4, drop size is 20 μm and icing duration is 5 min (a) −5°C air temperature and 1.0 g/m^3 of LWC, (b) −5°C air temperature and of 1.5 g/m^3 LWC, (c) −5°C air temperature and 2.0 g/m^3 LWC, (d) −3°C air temperature and 1.0 g/m^3 LWC, (e) −2°C air temperature and 1.0 g/m^3 LWC [56]

Although, the mass of the ice reduces due to the decrease in Reynolds number, the relative ice accretion size on the surface of the airfoil increases significantly. Consequently, the deterioration of aerodynamic performance due to ice accretion at low Reynolds numbers may be more serious. A numerical study on the aerodynamic penalties due to ice accretion on the HQ309, SD7032, and SD7037 airfoils was performed by Szilder and Yuan [57]. The chord length of the airfoils was 0.47 m. Their results showed that although the aerodynamic performance of the HQ309 airfoil under rime and glaze ice conditions showed smaller differences at an AoA lower than 9°, as the AoA increases from 9°, rime ice accumulated on the surface of the airfoil caused a significant degradation in its aerodynamic performance when compared to the glaze ice condition.

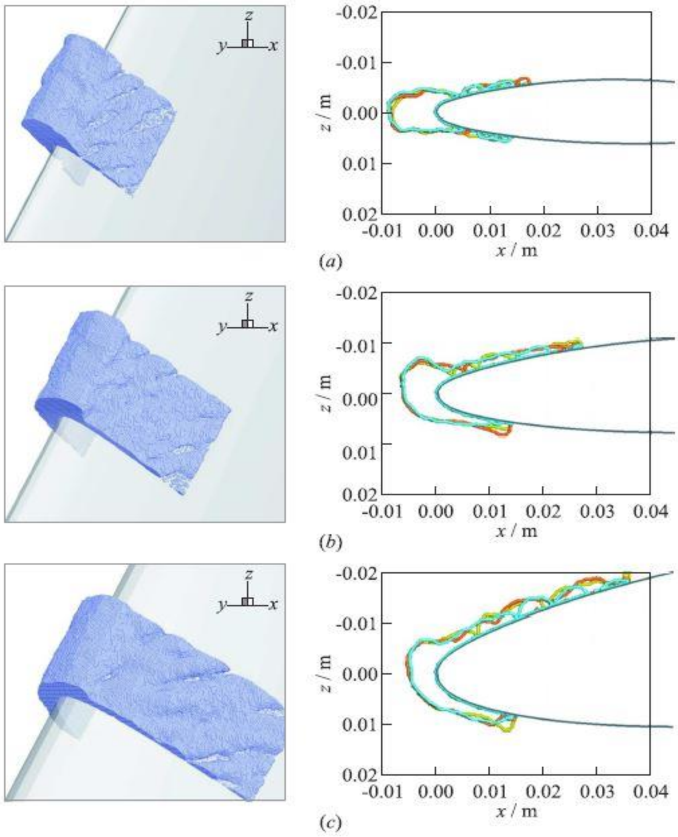

Figure 27. Prediction of ice accretion on the IM wing for 49.1 m/s of airspeed, AoA of 0°, drop size is 25 μm, and −2°C air temperature at three different spanwise locations: (a) 80% of the semispan, (b) 50% of the semispan, and (c) 20% of the semispan from the airfoil root [57]

Furthermore, prediction of the ice accumulation of the tested airfoils indicated that the largest ice accretion was observed on the suction side of the HQ309 airfoil whereas smallest was observed for SD7037 airfoil. The aerodynamic analysis showed that at cruise in icing conditions, HQ309 performed the best aerodynamic performance compared to SD7037. The opposite behavior was observed at stall conditions. Hann et al. conducted both experimental and numerical investigations on the effects of icing on the aerodynamic performance of a NREL S826 airfoil with a chord length of 0.45 m [58]. The experiments were conducted at Reynolds numbers of 2×10^5, 4×10^5 and 6×10^5 and AoA ranging from -7.5° to 17.5° in a wind tunnel with a test section of 1.8×2.7×12 m. The ice cases for the study were simulated in LEWICE and then created with a 3D printer for the experiments. For the numerical cases, IWT and LEWICE ice samples were selected. According to the LEWICE ice-shapes simulation results, in the case of horn accumulated airfoil, the lift was decreased by 26% and drag was increased by 330% at $\alpha = 0°$. For the rime and glaze ice cases at zero angle of attack, the reduction in lift was 15-16% and increase in drag was 40-60% which both showed comparable penalties.

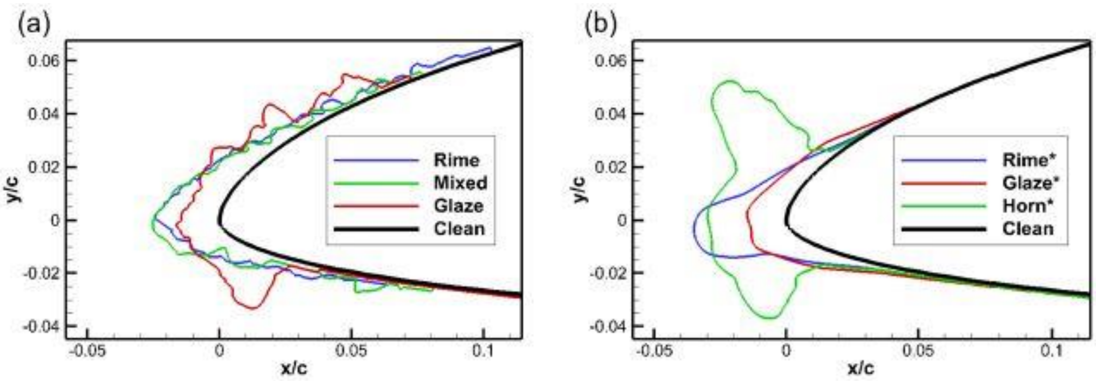

Figure 28. (a) Ice shapes obtained from the experimental data and (b) ice shapes from LEWICE [58]

Results of the IWT ice shapes showed that the highest degradation in the aerodynamic performance was observed for the glaze ice case. A 26-31% reduction in lift and a significant increase in drag by 220-290% was examined at zero attack angle. However, the stall angle of glaze accreted airfoil was unaffected. Furthermore, the rime ice accumulated airfoil exhibited a lower degree of degradation in aerodynamic performance than the glaze ice case. A decrease in lift and increase in drag by 17-19% and 100-190% respectively. Moreover, authors stated that an unexpected behavior in the stall region of rime ice cases where a sudden increase in lift at 11° attack angle up until stall angle especially at lower Reynolds numbers was observed. Also, a similar behavior of irregular lift increase was exhibited by mixed ice case in the stall region. Numerical results showed that, among all the ice cases, mixed ice has the lowest aerodynamic penalty by 15-18% decrease in lift and 80-130% increase in drag.

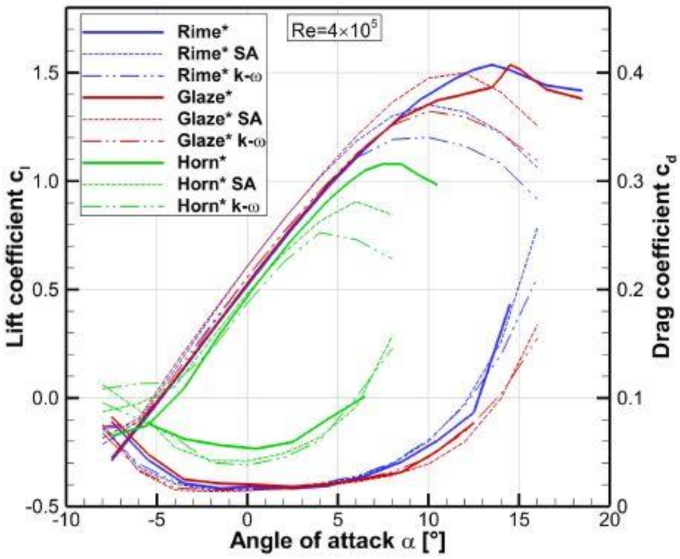

Figure 29. Comparison of the experimental and numerical results of the lift and drag coefficients against AoA at a Reynolds number of 4×10^5 for ice shapes from LEWICE [58]

Ice accumulation on an airfoil surface can change its mean camber, effective chord length, and surface roughness as well as alter its aerodynamic shape. These parameters due to ice accretion can cause separation of the flow over the surface of the airfoil as well early transition to turbulent flow from laminar flow. One effect of the ice accumulation on airfoils is a reduction in aerodynamic performance. Thus, it is crucial to comprehend how icing impacts an airfoil's aerodynamic efficiency. Although, a literature survey shows that several investigations have been conducted on the aerodynamic performance of ice accumulated UAV airfoils, it rather found scarce about the effects of ice accumulation on the aerodynamic performance of NACA 2415 at low Reynolds number with realistic approach; thus, it is necessary to investigate. This thesis investigates the aerodynamic performance degradation due to ice accumulations on the surface of NACA 2415 airfoil at a Reynolds number of 1.2×10^5 experimentally.

3. MATERIALS AND METHODS

3.1. Experimental Setup

The aerodynamic performance of a NACA2415 airfoil under various icing conditions was investigated in this thesis. Ice shapes were 3D-printed with PLA and was attached to the leading edges of the airfoils. Force measurement experiments were carried out in an open suction type low-speed wind tunnel as shown in Figure 30 with a test section of 57×57×100 cm located at the Deparment of Mechanical Engineering, Niğde Ömer Halisdemir University. The maximum speed of the wind tunnel near the center of the test section was about 20 m/s. The turbulence intensity was measured below 1% at maximum speed.

Figure 30. Open suction low-speed wind tunnel in Niğde Ömer Halisdemir University

Experiments were conducted at a Reynolds number of 1.2×10^5 based on the free-stream velocity and airfoil chord length (150 mm). Room temperature and pressure was calculated by using digital manometer. By using Engineering Equation Solver (EES), freestream velocity was calculated for a Reynolds number of 1.2×10^5. The desired free stream velocity is arranged by using a frequency inverter of the wind tunnel and a pitot tube.

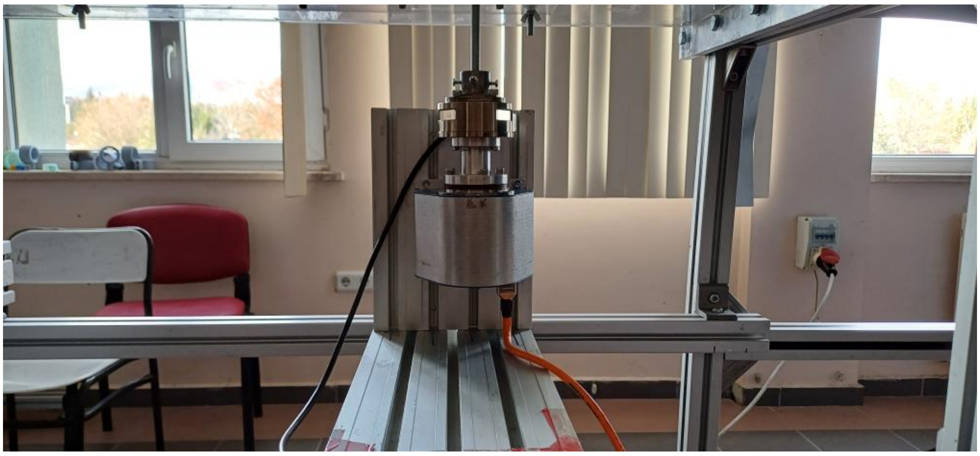

Figure 31. Traverse system, rotary unit, and load cell

A traverse system and computer-controlled rotary unit were used to change the angle of attack of the test models. MiniCTA software used to set the AoAs of the airfoils as shown in Figure 32.

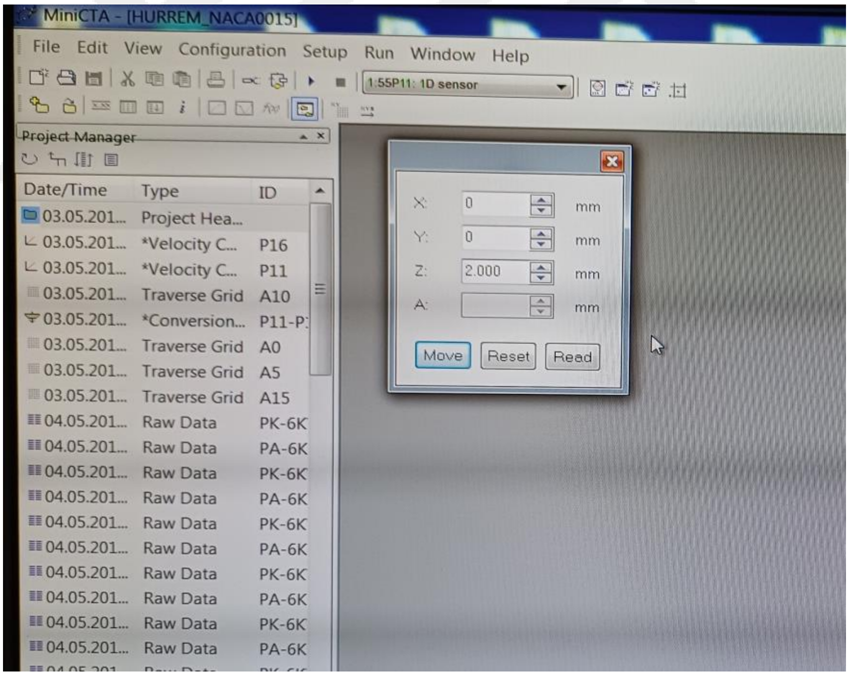

Figure 32. MiniCTA software to adjust the angle of attack of the test models

The test models were placed vertically in the test section to eliminate the effect of gravity on the force measurements. Two end plates were fixed at the top and bottom of the airfoil with a distance of 1-2 mm between them in order to block the vortices induced from both sides of the airfoil. Both end plates have 280-mm of Radius and 5-mm thickness.

Figure 33. Vertically placed test model in the wind tunnel test section

3.1.1 Airfoil Selection

The National Advisory Committee for Aeronautics (NACA) designed the NACA airfoils, which are airfoil shapes for aircraft wings. A string of numbers that come after the word "NACA" was used to characterize the geometry of the NACA airfoils [59]. The NACA 4-Digit code is defined as follows:

- The first number in 4 digit is the maximum camber as chord percentage.
- The second number in 4 digit indicates, in tens of percent of the chord, the maximum camber distance from the LE of the airfoil
- The latter two numbers represent the airfoil's maximum thickness expressed as a percentage of the chord.

According to the code above, NACA 2415 can be decoded as an asymmetrical or cambered airfoil with maximum camber of 2% camber or 0.02c located at 0.4c from the LE of the airfoil with a maximum thickness of 0.15c. NACA airfoils are widely used in the aviation and turbomachinery industries.

3.1.2 Production of Test Models

Airfoils and ice casings for the experiments were produced by a Creality Ender S1 3D printer with a printing material as 1.75 mm PLA+ (Poly Lactic Acid). Test models are produced by the additive manufacturing process in which PLA filaments are heated to a certain temperature and thereby added layer by layer to create the desired geometry. The printer nozzle has a diameter of 0.2 mm. Two different airfoil models were produced in terms of their dimensions. The printed models have a hole of 10 mm for the connection rod at the aerodynamic center of the airfoil.

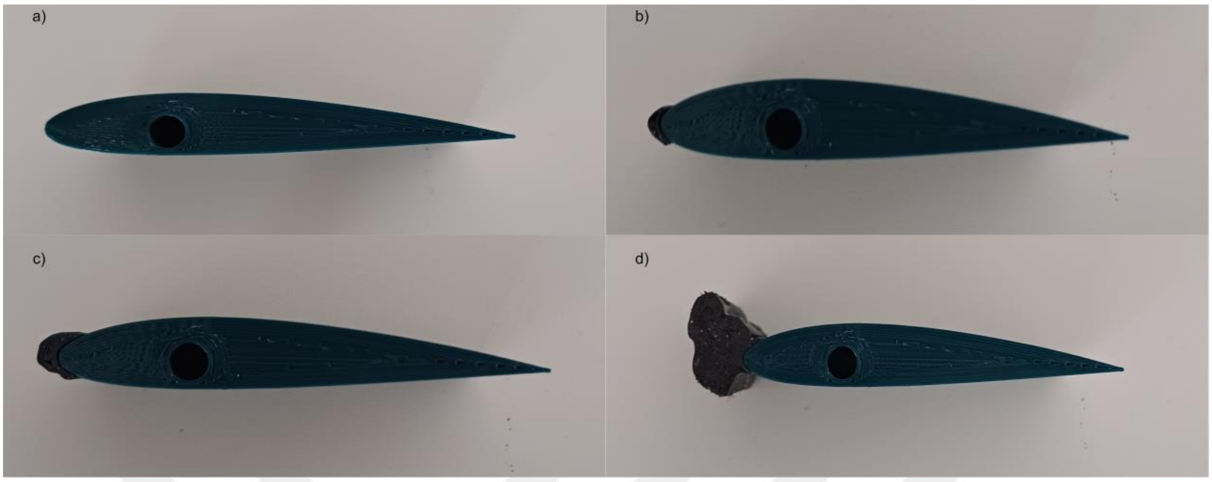

Figure 34. a) NACA2415 base airfoil, b) glaze ice accumulated airfoil, c) rime ice accumulated airfoil, and d) horn ice accumulated airfoil

For the force measurement experiments, the test models had chord and span lengths of 150 and 450 mm, respectively. Second, for flow visualization and velocity measurement experiments, the manufactured airfoils had chord and span lengths of 130 and 390 mm, respectively. The aspect ratio (AR) of the airfoils was maintained in all experiments. Ice shapes along the span were designed to be randomly produced for more realistic approach.

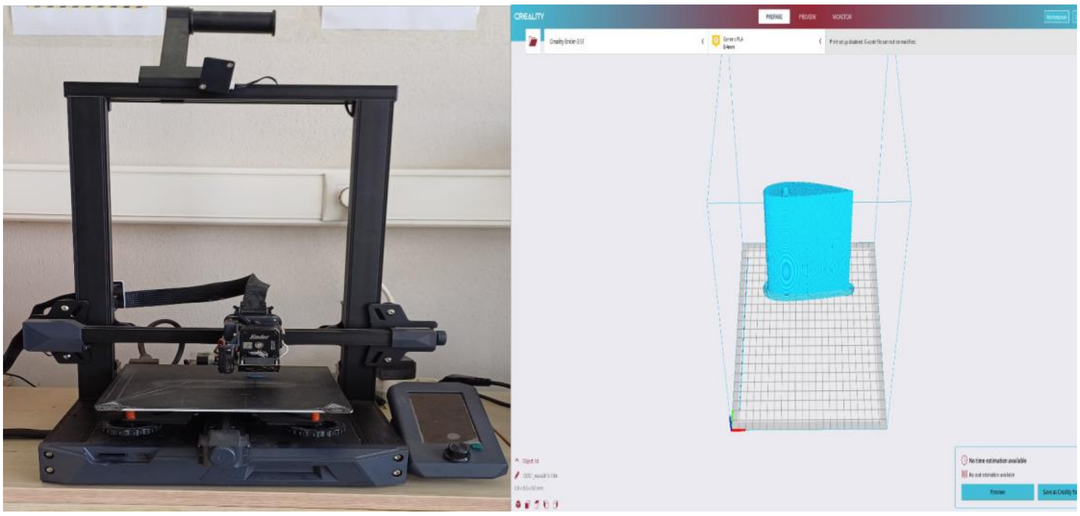

Figure 35. Creality Ender S1 3D printer and its software interface

The test models were divided into three parts due to the limitation of the 3D printer's maximum printing dimension. Later, the produced parts are merged with the adhesive. The airfoil surfaces were polished with sandpaper to create a smoother surface for flow visualization experiments. A 10 mm diameter connection rod goes through the aerodynamic center of the airfoil up to load cell to fix the airfoil inside the test section and calculate the aerodynamic forces acting on the models in the wind tunnel.

Table 1. Operating and geometrical properties of this thesis

Operating Properties				**Geometrical Properties**	
Force Measurement	$Re = 1.2 \times 10^5$	U_∞	14.48 m/s	Chord	150 mm
		μ	1.85×10^5 Pa s	Span	450 mm
	Overall number of data collected	20000		Wind tunnel cross-section length	57 cm × 57 cm × 120 cm
	Sampling Rate	1000 Hz			
Velocity Measurement	$Re = 1.2 \times 10^5$	U_∞	14.42 m/s	Chord	130 mm
		μ	1.85×10^5 Pa s	Span	390 mm
	Overall number of data collected	5000		Wind tunnel cross-section length	40 cm × 40 cm × 100 cm
	Sampling Rate	1000 Hz			
Endplate				Diameter	280 mm
				Thickness	5 mm
				Bevel angle	45°

3.1.3 Force Measurement System

An ATI 6-axis external load cell was used in the force measurement experiments to measure lift and drag forces. Force calibration was performed using the ATI DAQ software. To obtain consistent data, force calibrations were repeated at the start of each set of experiments. In addition, experimental data for each test were collected at a sample rate of 1000 Hz over 20 seconds which corresponds to 20000 data. Each force experiment was repeated 3 times for repeatability and to enhance the accuracy. The steps of the force experiments was listed below:

1. Adjust the angle of attack of the test model.
2. Calibrate the balance.
3. Turn on the wind tunnel.
4. Wait for the test speed and flow to be uniform.
5. Start data collection.
6. Turn off the wind tunnel after collection is finished.
7. Repeat the steps above through all attack angles.
8. Repeat the process three times for repeatability.

For the force measurement experiments, the AoA values of the test models ranged from -7 to 23°.

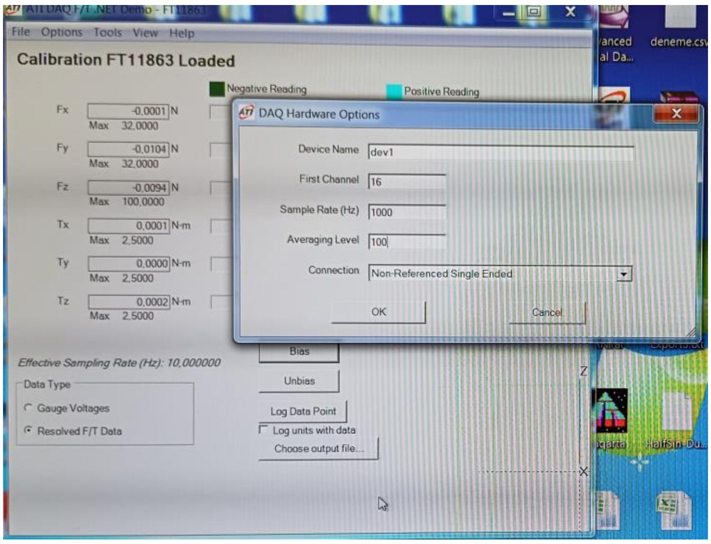

Figure 36. ATI DAQ Software for calibrating force data

Furthermore, the ATI DAQ software saves the force data in .xlsx format. Using *Microsoft Excel*, the mean lift and drag forces as well as lift and drag coefficients were calculated. General equations for calculating lift and drag coefficients are shown in E-1 and E-2:

$$C_L = \frac{F_L}{\frac{1}{2}\rho v^2 A} \tag{E.1}$$

$$C_D = \frac{F_D}{\frac{1}{2}\rho v^2 A} \tag{E.2}$$

Here, F_L and F_D are the lift and drag forces, respectively, ρ is density, v is the freestream velocity, and A is the airfoil area.

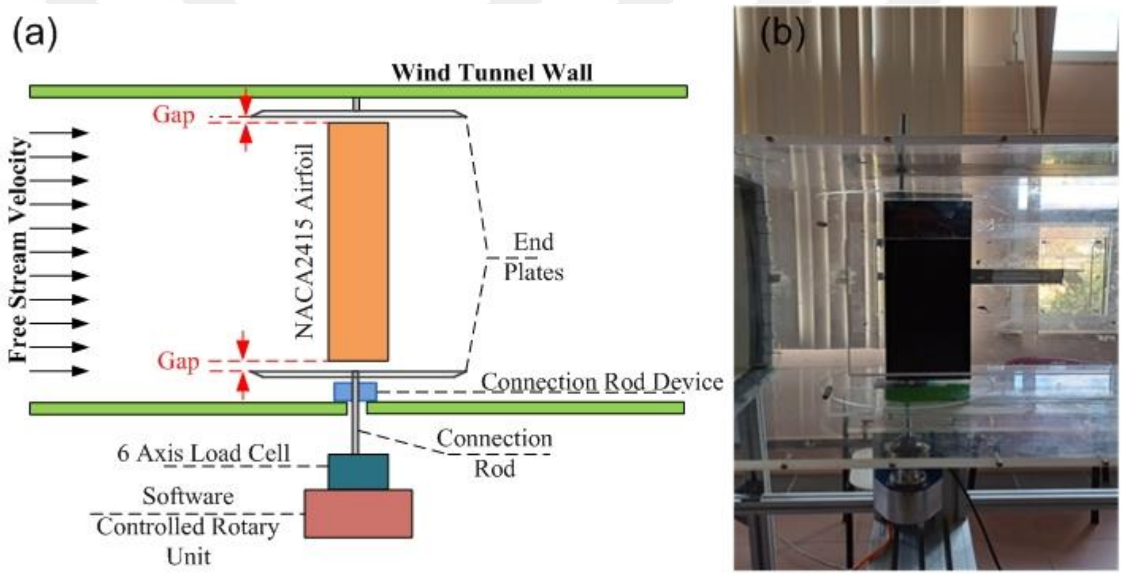

Figure 37. (a) Schematic of the force measurement setup and (b) test model in the wind tunnel test section

The setup for force measurement experiments consisted of a load cell, rotary unit, connecting rod, end plate, and test model as shown in Figure 37. The test models were placed vertically in the wind tunnel test section as seen in Figure 33, to avoid the effects of gravity on the force measurements. The connection rod was fixed inside the test airfoil through the aerodynamic center and connected to the 6-axis ATI load cell. The computer control rotary unit controls the angle of attack of the model using a software, as shown in Figure 32. The AoA values of the test models were arranged between -7 and 23° with an increment of 1°. The rotary unit has a sensitivity of approximately 0.2°. To create the interface effect, there was a small gap between the model and the endplate. According to Barlow et al., optimum gap limit is given by equation $g = s \times 0.005$ [60]. Where, "g" is gap between the endplate and test airfoil and "s" is the span of the test model. Thus, the gap between the model and endplate is approximately 2 mm.

3.1.4 Flow Visualization

Among the many accessible techniques in experimental fluid mechanics, flow visualization has been employed from the very beginning of fluid mechanics research to determine the location and sizes of the flow characteristics that being investigated. Since most fluids involved in the engineering applications, including air and water, are transparent, the flow visualization techniques are employed to show the patterns of flow of the fluids. Any flow visualization technique starts with the fundamental notion that a visible additive substance in small quantities can be separated from the visible main flow. In engineering, flow visualization is vital for flow analysis to comprehend and improve the flow characteristics, especially in complex, three-dimensional flows.

Figure 38. Open suction low-speed wind tunnel for flow visualization and velocity measurement experiments

The flow visualization experiments were carried out in an open suction-type low-speed wind tunnel with a test section of 40×40×100 cm located at the Propulsion and Flow Control Laboratory, Deparment of Aerospace Engineering, Adana Alparslan Türkeş Science and Technology University (ATÜ). The maximum speed of the wind tunnel near the center of the test section was about 40 m/s. The turbulence intensity in the wind tunnel was measured below 1% at maximum speed. For the flow visualization experiments, the test models were placed horizontally in the test section to better photograph the flow patterns over the surface of the airfoil.

3.1.4.1 *TiO_2 Based Surface Flow Visualization Technique*

Surface oil flow visualization is a comparatively simple technique which find great applicability in the wind tunnel testing. In this technique, the surface of the airfoil is covered with a thin layer of oil to photograph the flow events at the airfoil surface. The surface oil flow visualization technique is cheap and easy to apply, and it is a great tool to observe the flow topology on the airfoil surface. The mixture of oil should have the right consistency to successfully indicate the development of the boundary layer of the flow. Surface oil flows indicate the boundary of flow separation because the oil cannot penetrate the separation boundary.

According to Maltby and Keating, the oils widely used in the surface oil flow visualization technique are kerosene, light diesel oil, and light transformer oil [61]. For the experiments in this thesis SAE 30 pump oil was chosen as the oil medium. The pigment chosen for the flow visualization is TiO_2 or titanium dioxide powder. This pigment is white and opaque at the same time. Therefore, making it suitable for a dark background to get high contrast flow patterns. Thus, the airfoil surfaces for experiments were painted in matte black color. Oil paint additives are used to regulate the size of coagulation flocs. Additionally, linseed oil and oleic acid are typically used since they produce optimal outcomes. For surface oil flow visualization experiments in this thesis, oleic acid was selected as additive since it gives better results at low speeds.

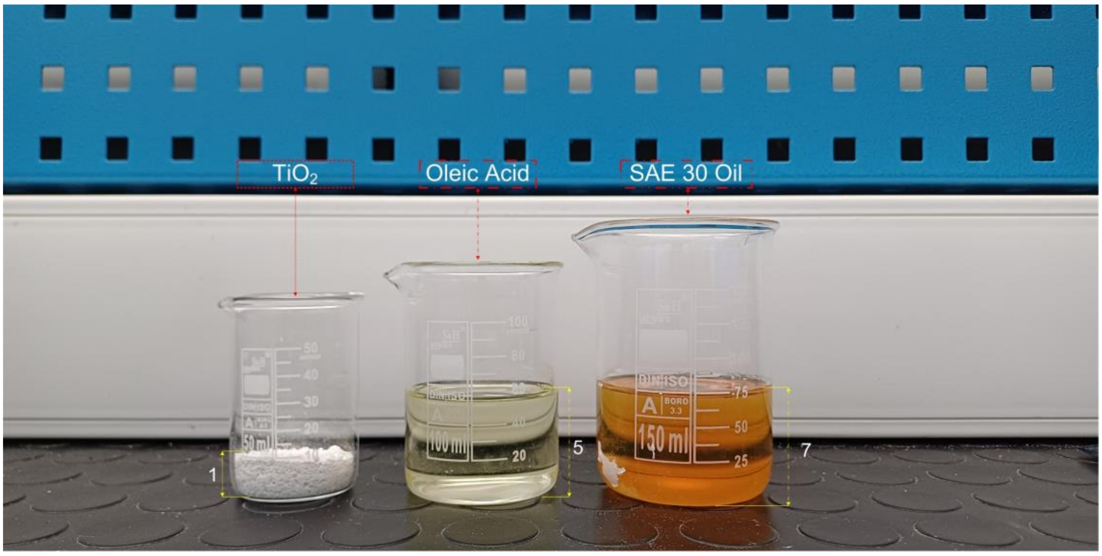

Figure 39. From left to right; titanium dioxide powder, oleic acid, and SAE 30 pump oil

The oil mixture for flow visualization used in the studies conducted by Sudhakar et al. [62] and Seyhan and Sarioglu [63] consists of TiO_2 powder, oleic acid, and SAE 60 pump oil at a ratio of 1:5:7. A survey of the literature reveals that there are no fixed oil mixture contents or ratios. Thus, oil mixture for flow visualization in this thesis consists of TiO_2 powder, oleic acid, and SAE 30 pump oil at a ratio of 1:5:7. The oil mixture was applied to both the suction and pressure sides with a paintbrush until both sides are covered with mixture uniformly. This process is repeated for each model. The wind tunnel was kept running until the oil mixture on both surfaces of test models was dry. Finally, the pressure and suction sides of the airfoil model are photographed. The imaging process was carried out by using a DJI Osmo Action 4 action camera with a resolution of 27 MP.

3.1.4.2 *Smoke-Wire Flow Visualization Technique*

Smoke-wire flow visualization is a great tool in experimental fluid mechanics for visualizing flow streamlines around test models. It is inexpensive, simple to use, and provides a clear picture of flow structures. Typically, a smoke-wire flow visualization system consists of a resistant wire, a weight to maintain tension in the wire, an electric current-generating DC power supply, a camera for recording, and a light source. For flow visualization experiments, the stainless steel resistant wire and liquid paraffin is selected as smoke-generating substance. The resistant wire was placed vertically before the test models. At regular intervals, liquid paraffin was poured onto the resistance wire and retained there like dew particles [63]. Applying voltage causes the wire to heat up quickly, allowing evaporated paraffin to produce smoke with high density while avoiding damage to the wire. A brief setup of the smoke-wire experiments is shown in Figure 40.

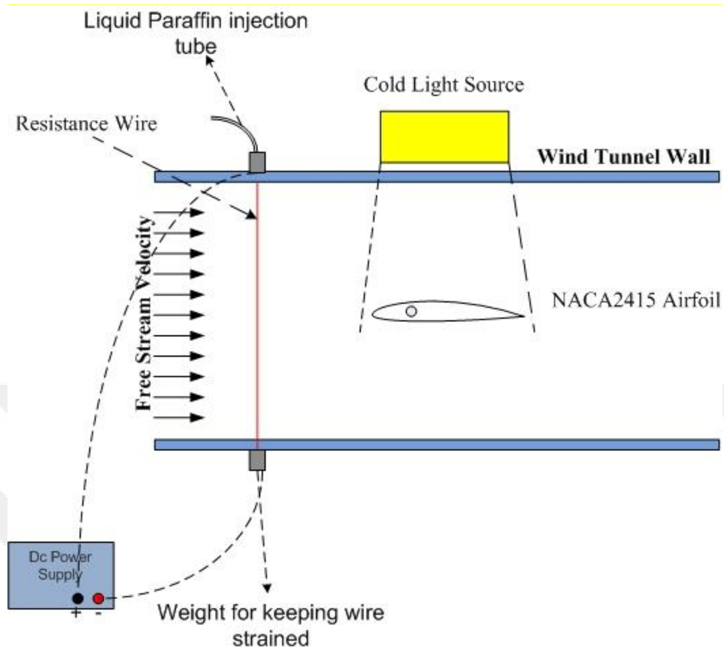

Figure 40. Smoke-wire flow visualization setup

The cold light source made it easier to visualize the streamlines or flow structures surrounding the test model formed by vaporized paraffin. The resultant flow structure is simultaneously captured by the camera.

3.1.5 Velocity Measurement System

The velocity fields for the base and ice accreted models were measured by a Multichannel Contant Temperature Anemometer (CTA) Dantec 54N81 hot-wire anemometry device. A 55P16 mobile hot-wire probe was used to measure both the freestream velocity and test model velocity. The hot-wire probe was placed on an automated traverse system to move vertically behind the test models. From each station, 5000 data are obtained at 1000 Hz for 5 seconds. To normalize the velocity distribution graphics, the velocity data obtained from the wake region of test models were divided into freestream velocity values. Velocity measurement calibration was performed using a pitot-static tube. Moreover, the anemometer output was fitted to a fourth-order polynomial with a highest linearization error of 0.9%. It is estimated that velocity measurement using a hot-wire anemometer have an uncertainty of approximately ±5.4%.

3.1.6 Uncertainty Analysis and Repeatability

The uncertainty of the measurement depends on the uncertainties of the calibration device, linearization, repeatability, the accuracy of the reference calibration device, and position of the probe. Applying the statistical analysis method reported in [64], it was determined that the uncertainty of the force measurement system was around ±3.2%. The uncertainties of the data acquisition card, load cell system, rotary unit-based attack angle arrangement, and interface effect equipment were all taken into account when determining the system uncertainty. Additionally, the velocity measurement using the hot-wire anemometer has an uncertainty of approximately ±5.4%. The uncertainties of dimensionless numbers such as Re, C_L, and C_D were measured about 5.5%, 6.8%, and 6.8%, respectively. The details regarding the uncertainty measurements are discussed in the Appendix.

3.1.7 Blockage and Aspect Ratios

The aspect ratio of the models throughout the experiments was kept constant at 3 AR. The blockage ratio is defined as the ratio of the frontal area of the test model to the area of the test section. For the NACA 2415 airfoil at 0° angle of attack, blockage ratio was around 5% in the Niğde Ömerhalisdemir University wind tunnel. When the blockage ratio is less than 10%, the blockage effects on the experimental results are minimal or negligible, hence, no blockage corrections were applied to the results of this thesis [65].

4. RESULTS AND DISCUSSIONS

In this thesis, the effects of three different ice accumulations on the aerodynamic performance of the NACA 2415 airfoil is investigated. Force and velocity measurements, as well as two different flow visualization techniques (surface oil flow visualization and smoke-wire flow visualization), are performed at Re=1.2×10^5 to observe the aforementioned effect. The Angle of attack for force measurements are ranged from -7° to 23°. An attack angle of 23° was chosen to investigate the post-stall characteristics of ice accreted models. Glaze ice, rime ice, and horn ice accumulated airfoils are shortened to GIA,RIA, and HIA, respectively, to simplify the pronunciation of the airfoils. Attack angles for velocity measurements and flow visualization experiments were based on pre-stall, stall, and post-stall angles for all test models. Where 4°, 13°, 14° and 17° AoAs are stall angles of HIA, RIA, base and GIA models, respectively. A 20° attack angle was selected as post-stall angle for the GIA model.

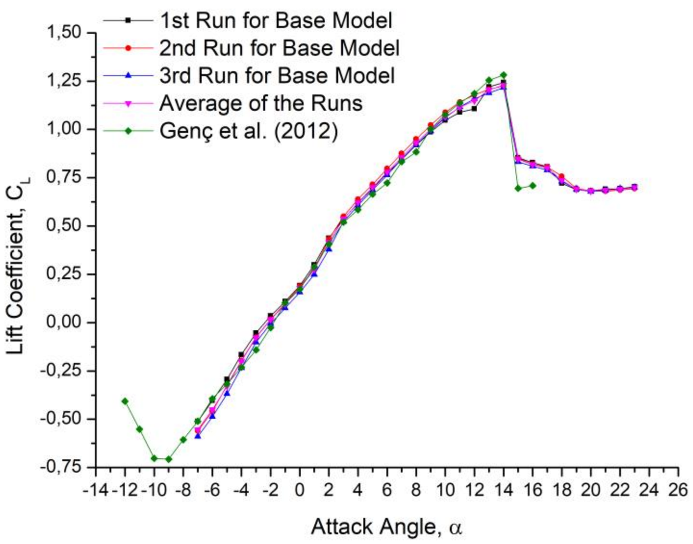

Figure 41. C_L vs. AoA graph for three repeated runs of the base model and literature

Figure 41 shows the lift coefficients against the angle of attack of the base model and NACA 2415 airfoil from the study of Genç et al. at Re=1.0×10^5 [66]. The stall characteristics of the baseline airfoil in the current thesis and the previous study are similar, as can be seen from the graph above. Three runs were performed for the NACA 2415 base airfoil for repeatability and uncertainty. Moreover, as seen in Figure 42, the current study and the study of [66] exhibit comparable drag profiles against AoA.

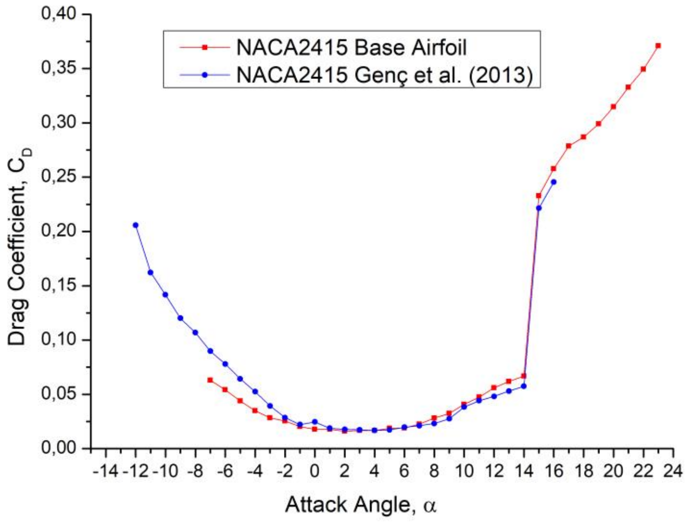

Figure 42. Drag coefficients of base model and literature versus angle of attack

The average lift-to-drag ratio of the base model is shown in Figure 43. For each model and angle of attack, the force measurements were repeated three times. All lift and drag coefficient data from the base model were merged into a single dataset, as shown in the figure below. Consequently, the merged data were used to compare the aerodynamic performances of ice accumulated models and the base model.

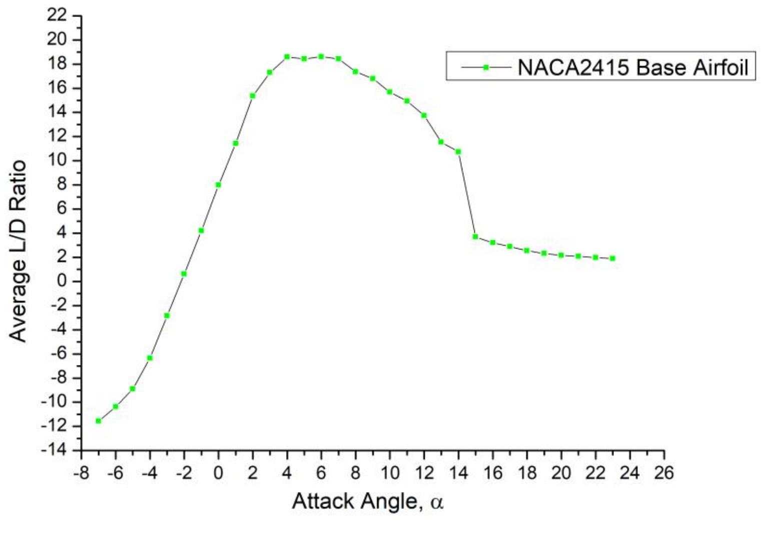

Figure 43. Average L/D ratio vs. AoA of the base model

Figure 44 shows the lift coefficients of the GIA model and base model against the attack angle. Results showed that a 20% decrease in the maximum lift coefficient observed in airfoil with glaze ice compared to the base model. In contrast, a smoother stall characteristic was observed in the GIA airfoil compared to the base model. Additionally, the stall (critical) angle α_{stall} of the GIA model against the base model was shifted 3° from 14° to 17°. A sudden increase in the lift coefficient of the GIA airfoil at post stall has been observed and can be seen in figure below. Although, the exact reason seems to be unknown in the literature, one of the hypotheses is that glaze ice accumulation on the leading edge of the airfoil increases the camber of the airfoil [58]. Moreover, several other studies have indicated that are accreted ice on the leading edge acts as a nose droop [67] or from a localized laminar separation bubble [68].

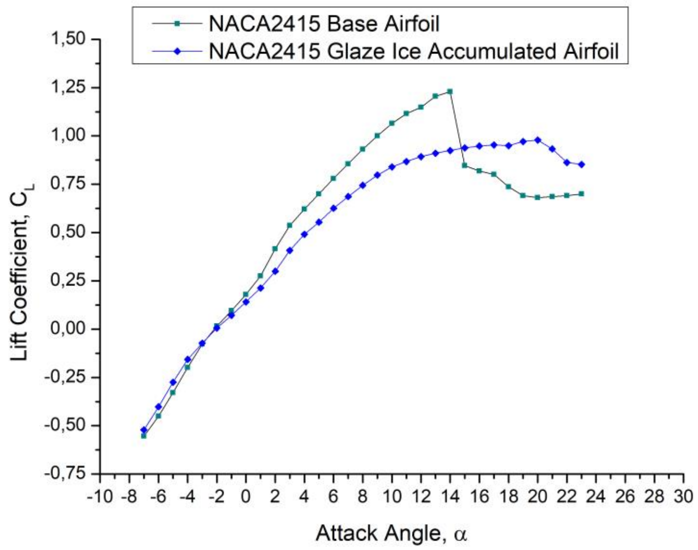

Figure 44. Lift coefficients of glaze ice accumulated airfoil and base airfoil against the AoA

The GIA airfoil and base airfoil drag coefficients as functions of the attack angle were shown in Figure 45. At 0° attack angle, 14% increase in C_D was observed for the GIA airfoil compared to the base airfoil. A sudden increase in the C_D graph of the GIA model can be seen at 17° AoA due to stalling. At post-stall conditions, it seems that the drag coefficient of GIA airfoil was less than that of the base airfoil.

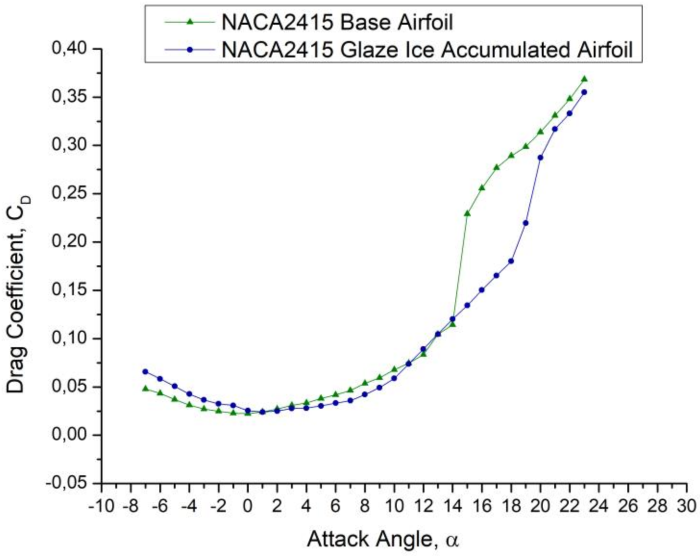

Figure 45. C_D of the GIA and base models versus AoA

Figure 46 illustrates the lift-to-drag ratio vs. attack angle of the GIA and base models. The base airfoil L/D ratio peaks at an attack angle of 5°, whereas for the GIA airfoil L/D ratio peaks at 8° angle of attack. A smoother stall characteristic of the GIA model can also be observed in Figure 46.

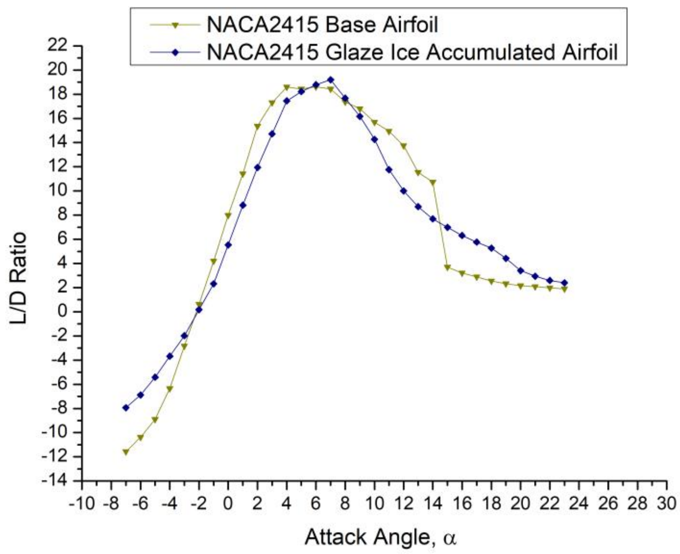

Figure 46. L/D ratios of the base and GIA airfoils to the attack angle

The GIA airfoil had a lower slope of the L/D ratio versus AoA around the stall than the base model, in contrast to the base airfoil where the L/D ratio abruptly decreases at the stall angle.

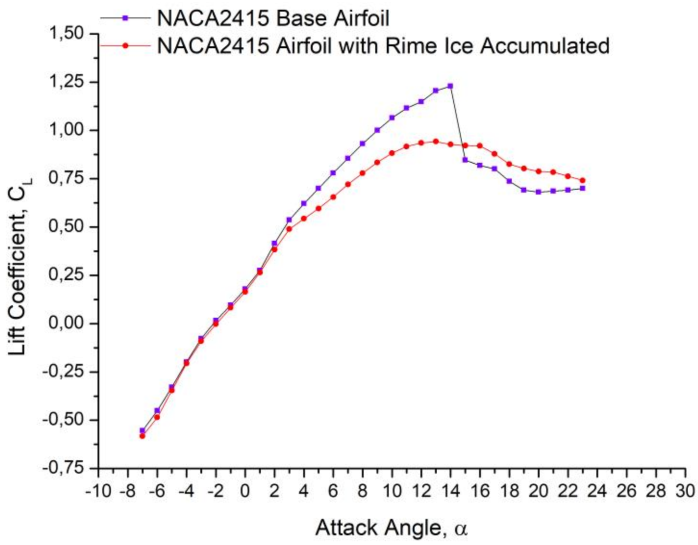

Figure 47. C_L vs. α graph of the RIA and base models

In Figure 47, the C_L versus attack angle graph of the RIA and base models was displayed. Results showed that C_{Lmax} is decreased around 23% for RIA airfoil compared to unmodified airfoil. Moreover, a shift in the stall angle about 1° was observed for RIA model where it stalled at 13° AoA. Overall, the lift coefficient of the RIA airfoil was smaller than that of the baseline airfoil at all attack angles. However, a smoother stall characteristic was also observed in the RIA model. The drag coefficients of the RIA and base models were shown in Figure 48. At lower attack angles, both airfoils exhibited similar drag coefficients. The C_D of the RIA airfoil increased promptly compared to the base airfoil as the angle of attack increased. The maximum increase in drag coefficient observed at approximately 29% at 14° AoA for the RIA model. Additionally, at post stall, the C_D of the rime ice accumulated model was higher than that of the base model.

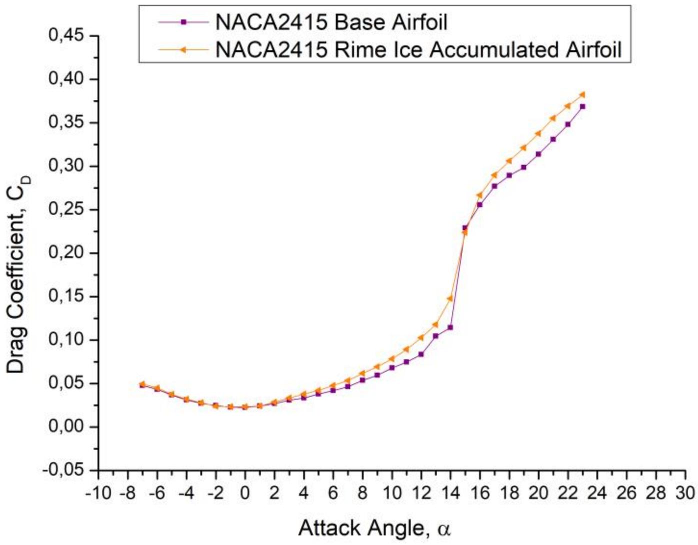

Figure 48. C_D vs. angle of attack for the RIA and base models

As shown in Figure 49, the L/D ratio of the RIA airfoil was smaller than that of the base model up to the stall angle. Where at the post-stall, both airfoils exhibited similar L/D ratios against attack angle. A maximum decrease in the L/D ratio of the RIA model compared to the base model was observed at 7° attack angle which was about 27%.

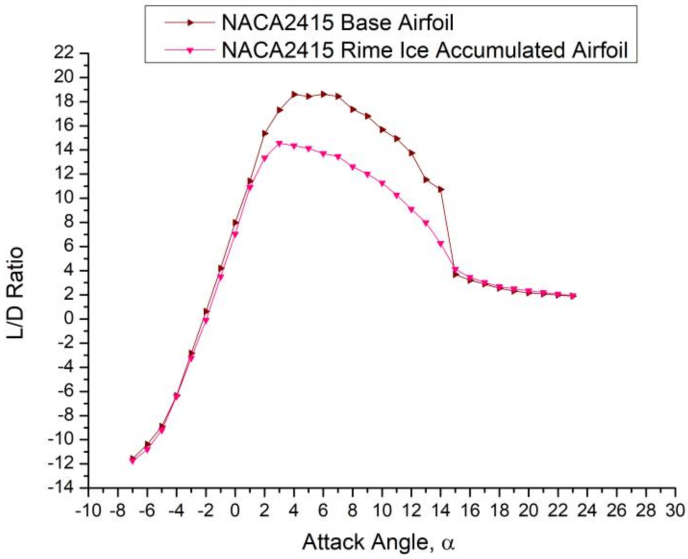

Figure 49. L/D ratio vs. attack angle of the RIA and base airfoils

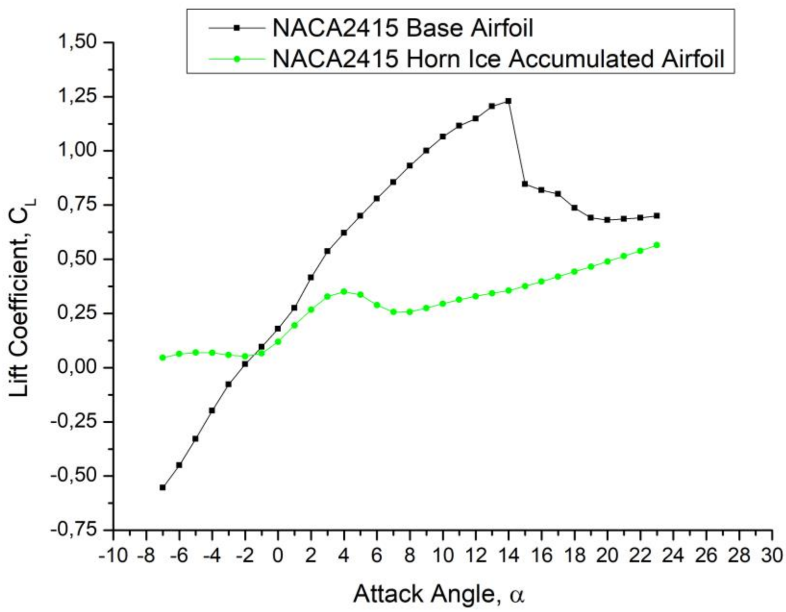

Figure 50. Lift coefficients of the HIA and base models against attack angle

Figure 50 shows the HIA and baseline model lift coefficients as functions of the attack angle. The protuberances or horns of the HIA model significantly affect the airflow on the airfoil, where at 4° angle of attack the airfoil were stalled. At 0° of AoA, a small separation bubble was observed around the leading edge of the HIA airfoil (see Figure 67). The lift coefficient of the HIA model decreased by approximately 44% and 71% at AoAs of 4° and 14°, respectively. The maximum lift coefficient was reduced about 88% for the HIA airfoil. Figure 51 illustrates a notable rise in the drag coefficient of the HIA model up to the base model' stall angle. Moreover, at post-stall, the C_D of the HIA airfoil were higher than that of the baseline airfoil. At 0° attack angle, an increase of 307% in drag coefficient of the HIA model was noted. The maximum increase in C_D was observed at -1° AoA.

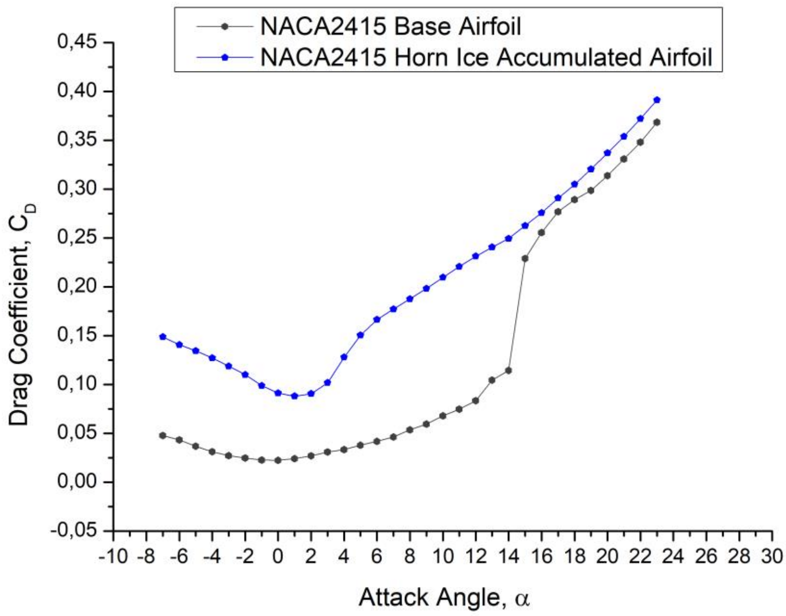

Figure 51. The drag coefficients of the HIA and base models against attack angle

As seen in Figure 52, the L/D ratio of the HIA model increased from 0° to 4° which latter is the stall angle. Afterwards, the L/D ratio decreased and then became linear up to 23° of AoA. The lost in L/D ratio was about 83% and 85% for 0° and 4° attack angles, respectively.

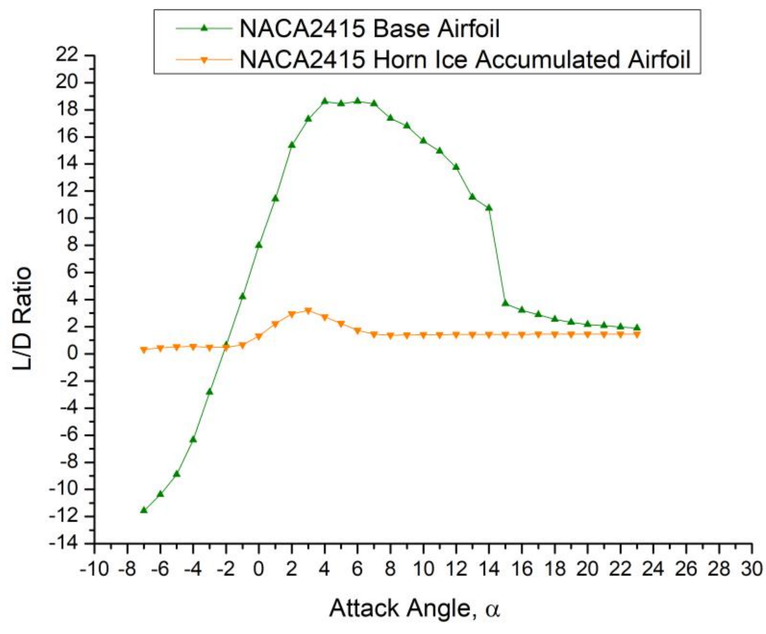

Figure 52. Lift-to-drag ratios of the HIA and base airfoils to AoA

The flow around the NACA 2415 base airfoil was captured by smoke-wire flow visualization. The flow structures or streamlines around the airfoil are presented in Figure 53 at various attack angles.

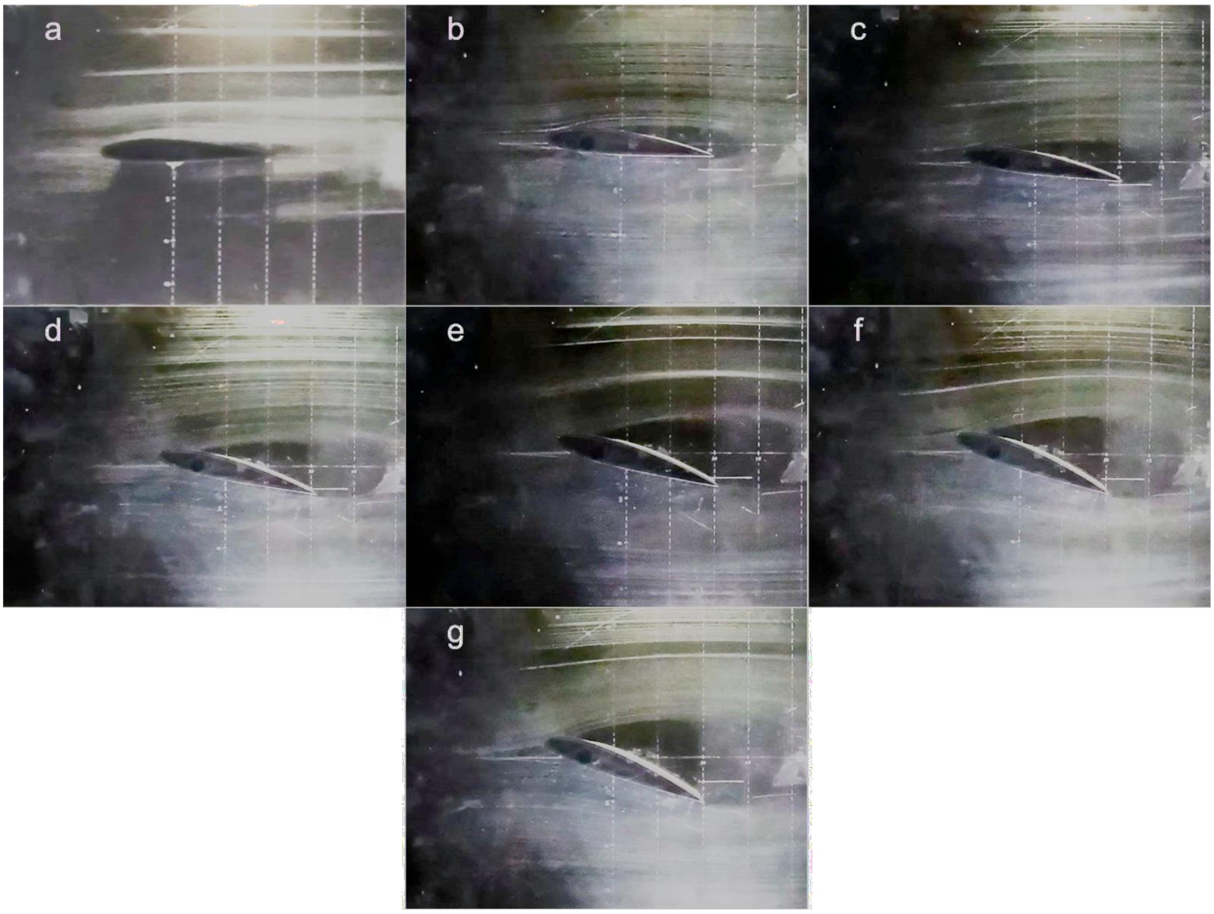

Figure 53. Smoke-wire experiments of the base model at different attack angles starting from (a) 0°, (b) 4°, (c) 8°, (d) 13°, (e) 14°, (f) 17°, and (g) 20°

Figure 53 shows that as the angle of attack increases, the flow separation on the base airfoil moves toward the leading edge from the trailing edge (TE). Moreover, at a high AoA, the flow is separated from the LE of the airfoil. Additionally, the wake width of the base airfoil grew as the attack angle increased. Figure 54 illustrates the photographs captured in the smoke-wire experiments of the GIA airfoil. Flow separation was observed to moving toward the LE from the TE as the attack angle increases. Moreover, the wake width of the GIA airfoil expanded as the angle of attack rised. Figure 53 (e) shows the baseline airfoil at a stall angle of $\alpha = 14°$, and Figure 54 (e) illustrates the flow structure around the GIA airfoil at this angle. Furthermore, it can be seen that in contrast to the base airfoil, the flow is still attached behind the LE of the GIA airfoil.

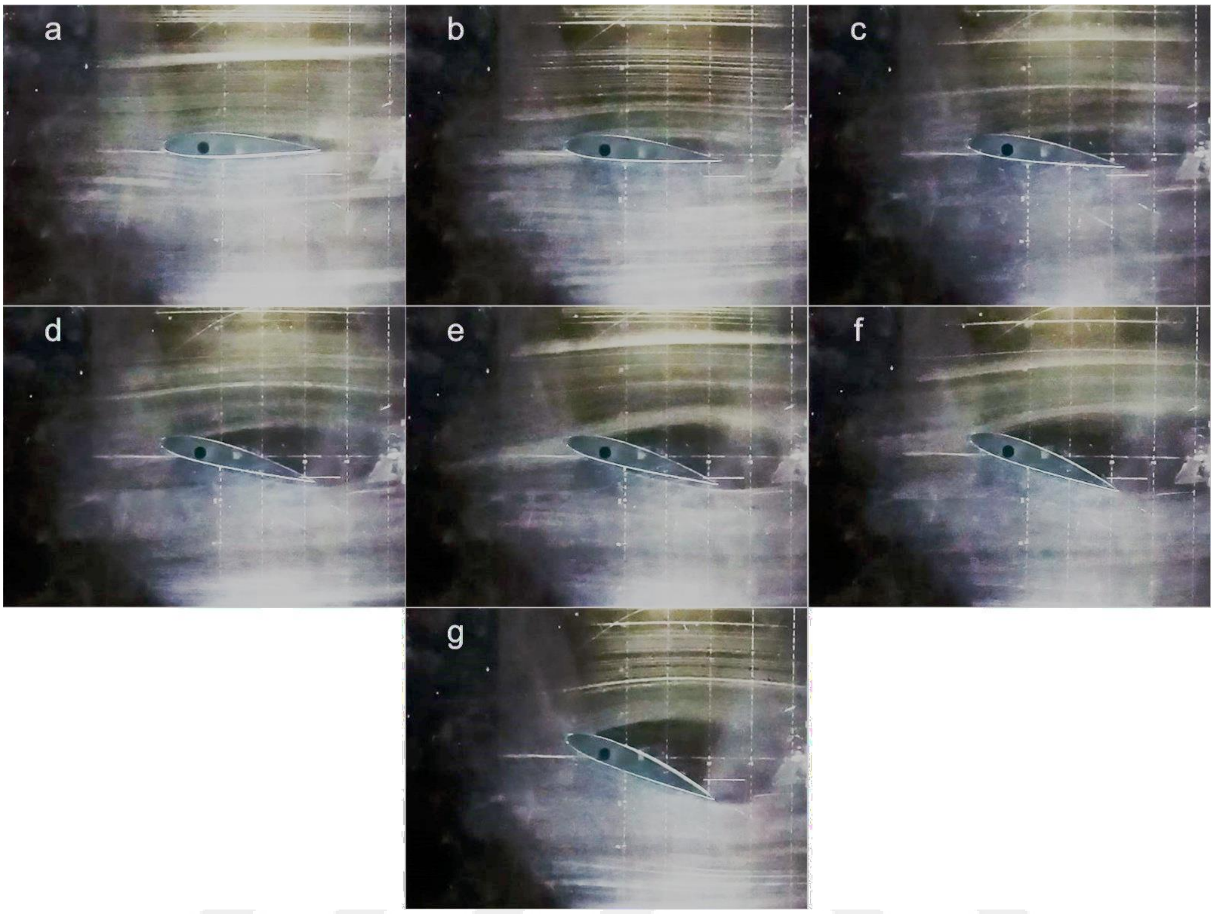

Figure 54. Smoke-wire experiments of the GIA model at different attack angles starting from (a) 0°, (b) 4°, (c) 8°, (d) 13°, (e) 14°, (f) 17°, and (g) 20°

A captures of the smoke-wire flow visualization experiments of the RIA airfoil were presented in Figure 55. As shown in Figure 55 (d), the flow separated from the LE of the RIA airfoil at 13° AoA as observed in the force measurements. Compared to the base and GIA models, the wake width of the RIA was larger at 20° AoA as observed in Figure 55 (g). Figure 56 represents the smoke-wire flow visualization photos of the HIA airfoil at seven different attack angles. Even at 0° AoA, it can be seen from Figure 56 (a) that, the flow separation was close to the LE of the the HIA airfoil with thicker boundary layer than the other models.

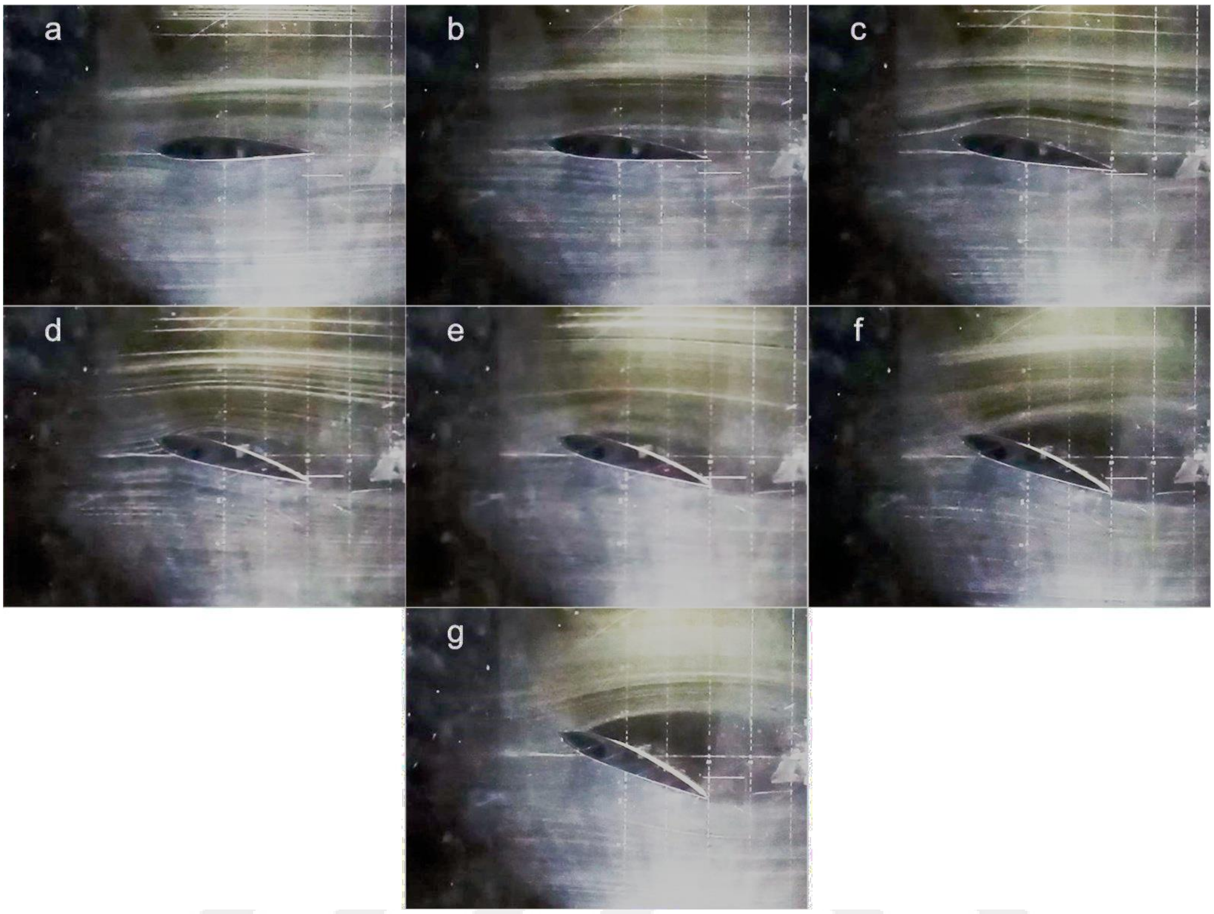

Figure 55. Photographs of smoke-wire experiments of the RIA model at different attack angles starting from (a) 0°, (b) 4°, (c) 8°, (d) 13°, (e) 14°, (f) 17°, and (g) 20°

Figure 56 (c) shows the flow structure around the HIA airfoil at 8° AoA. Since this model had a stall angle of 4°, it can be seen that the flow is completely separated from the suction side of the HIA airfoil. Additionally, compared to the other models, the wake width of the HIA airfoil was wider at all attack angles expect α=20° in the smoke-wire flow visualization experiments.

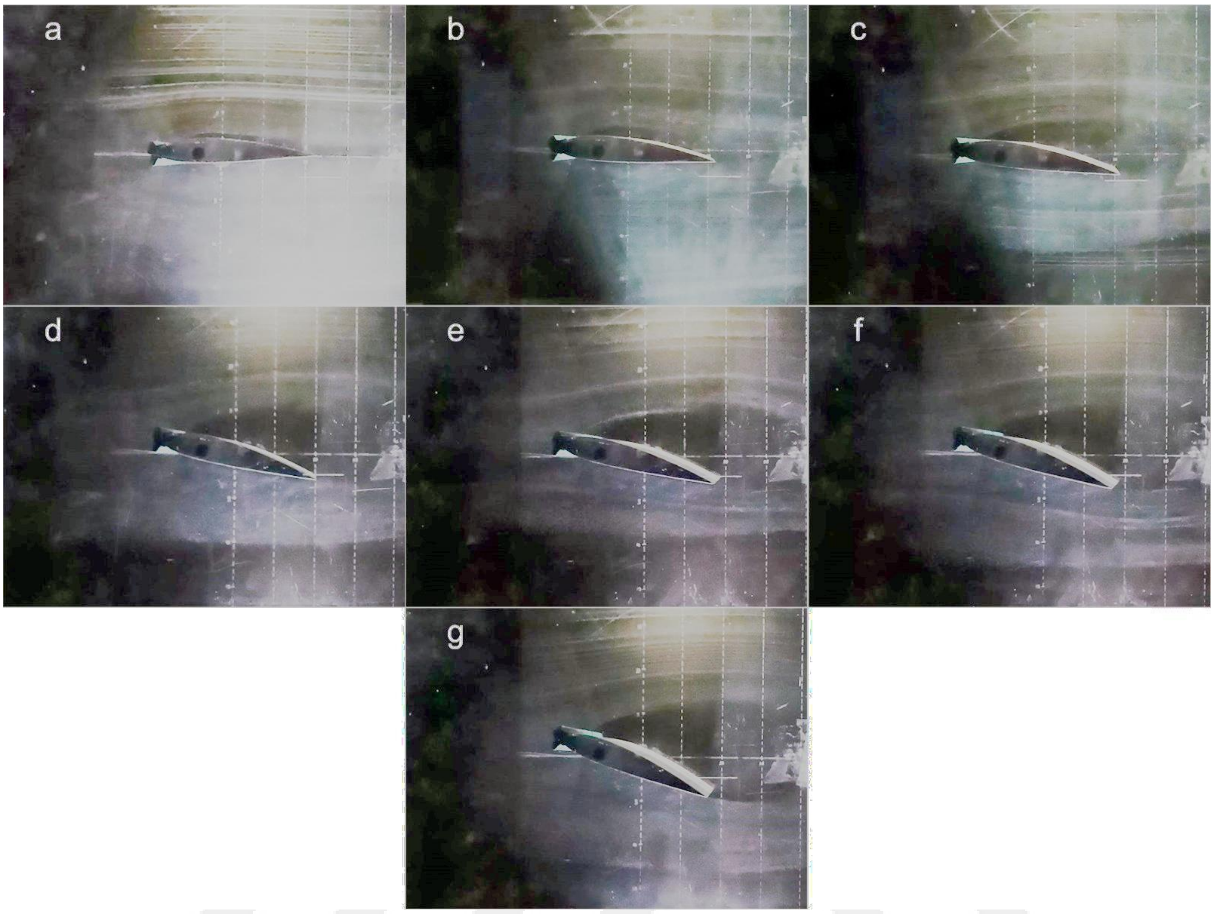

Figure 56. Smoke-wire experiments of the HIA model at different attack angles starting from (a) 0°, (b) 4°, (c) 8°, (d) 13°, (e) 14°, (f) 17°, and (g) 20°

The following figures show the wake profiles of the investigated models. In Figs. 57-63, the wake width graphs for U/U_0 are displayed for test models at seven different attack angles, same as in the smoke-wire experiments, as stated above. The velocity measurement stations were selected from the smoke-wire flow visualization experiments. In addition, each adjacent station was 10 mm away from each other. The hot-wire probe was placed at one chord length or 1C from the trailing edge of the test airfoils. As seen in Figs. 57-63, the wake width of the test airfoils tends to increase with increasing attack angle. Consequently, this increase in the wake width may cause an increase in the drag coefficient and a decrease in the lift coefficient of the investigated models, as confirmed by the force measurements. Furthermore, velocity measurements and smoke-wire flow visualization confirmed that the HIA model has the largest wake width except 20° AoA among all test models. Figure 57 shows the wake profiles of the test models at 0° angle of attack. According to the graph, HIA airfoil had the wider wake width, following RIA airfoil when compared to GIA and base airfoils. It seems that both the GIA and base model have similar wake widths at current attack angle.

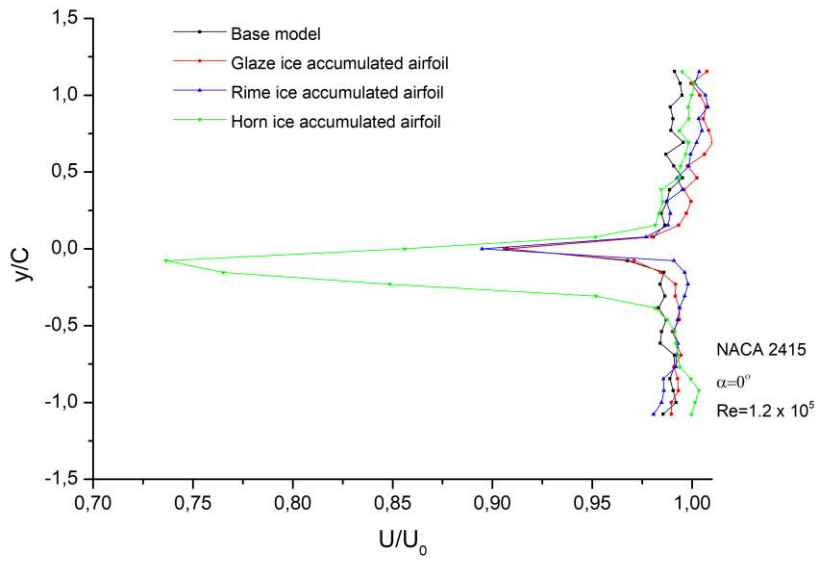

Figure 57. Wake profile of the test models at an angle of attack of 0°

Figure 58 illustrates the wake profiles of the investigated models at an angle of attack of 4°. The HIA airfoil has the widest wake profile at this attack angle. Similar to Figure 57, the RIA airfoil has the second-largest wake width. Moreover, at 4° AoA, the wake width of the GIA airfoil was wider than that of the base model.

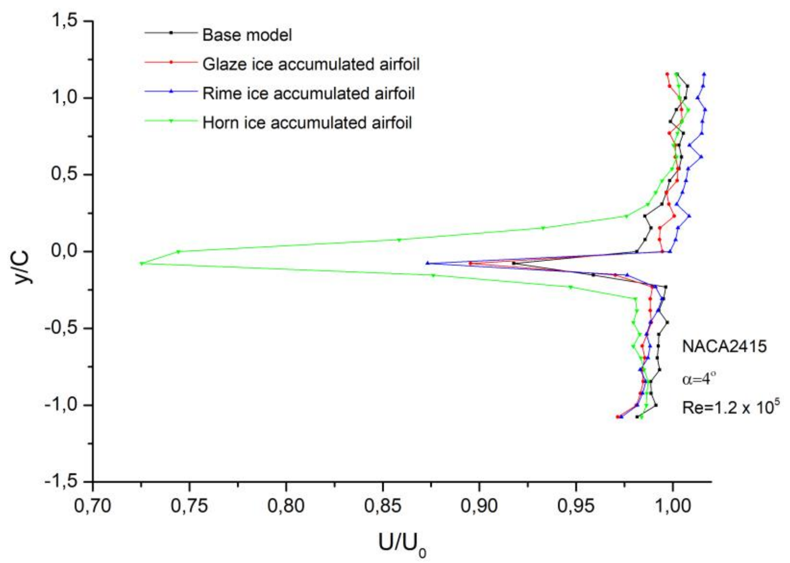

Figure 58. Wake profile of the test models at 4° attack angle

As shown in Figure 58, the wake regions of the RIA, GIA, and the base models has shifted downward as the AoA increased from 0° to 4°. Conversely, the wake profile of the HIA model shifted upwards at the stall angle. The lowest U/U_o value for the HIA airfoil occurred below the TE at both 0° and 4° attack angles.

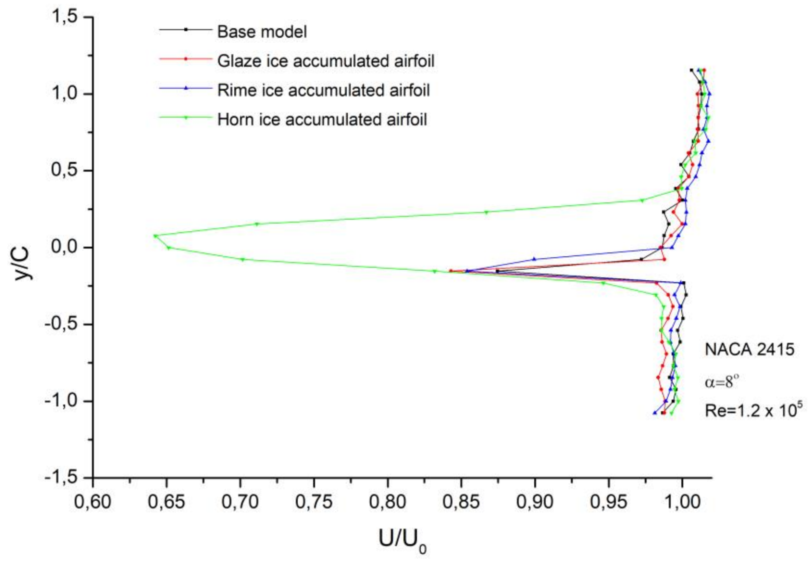

Figure 59. Wake profile of the test models at 8° attack angle

The wake profiles of the investigated airfoils at an 8° attack angle were represented in Figure 59. The wake profile of the HIA model seems to shifted upwards. Also, the wake width of this model has grew as the attack angle increased. Contrary to the wake profiles of the RIA and GIA at 4° AoA, the wake width of the GIA model was wider than that of the RIA model. Moreover, at 8° AoA, the wake width of the baseline model appeared to be narrower compared to other models.

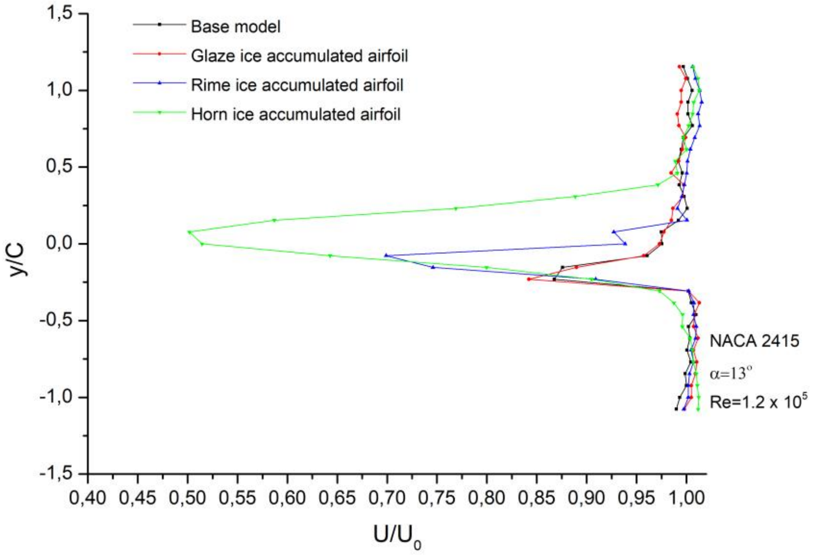

Figure 60. Wake profile of the test models at 13° angle of attack

The wake width of the RIA airfoil seems to increased substantially since α_{stall} = 13° in this model. As can be seen in Figure 60, the HIA model has the widest wake profile among all the models. A wider wake profile in the GIA model than in the base model continues at this angle of attack. For α = 13°, the RIA airfoil model exhibited a double-peak behavior in the wake profile, possibly due to distinct velocity gradients from the boundary layers of airfoil suction and pressure sides. Additionally, it can be stated that this double-peak behavior may have occurred due to the randomly accumulated ice on the airfoil model.

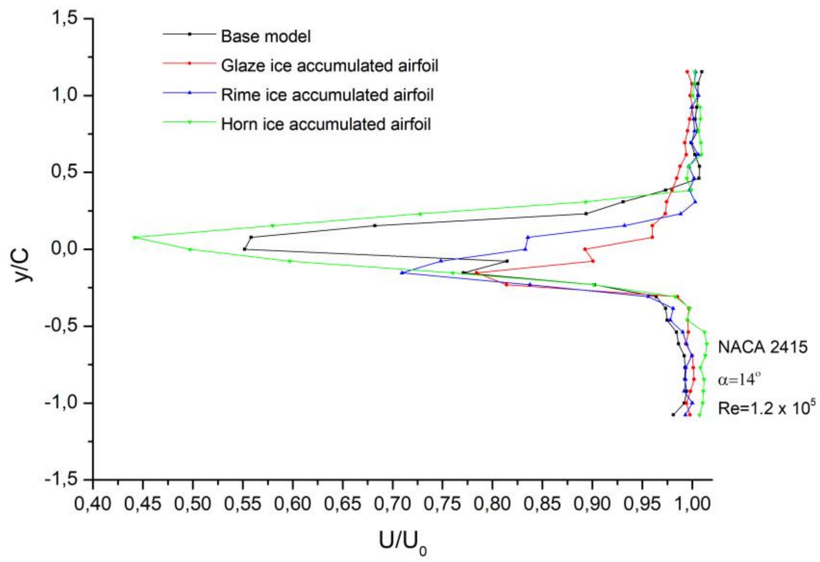

Figure 61. Wake profile of the test models at 14° angle of attack

Figure 61 represents the wake profile of the investigated airfoils at α = 14°. The HIA airfoil has the widest wake profile as evidenced by smoke-wire experiments. When compared with the 13° AoA, the wake width of the base airfoil increased significantly due to stall. Consequently, a large wake width for both the HIA and base models can be observed due to the flow separation on the suction side of the airfoils. The lowest U/U_o value of the HIA airfoil occurred above the TE. Furthermore, the GIA model had the narrowest wake width among the test models. A double-peak behavior in the wake profiles of both the GIA and base models as well as the RIA model was observed. Additionally, a very prominent double-peak behavior can be noted for the RIA airfoil at an attack angle of 17°, as shown in Figure 62. The width of the wake region in the test airfoil models grew as the angle of attack increased to 17°.

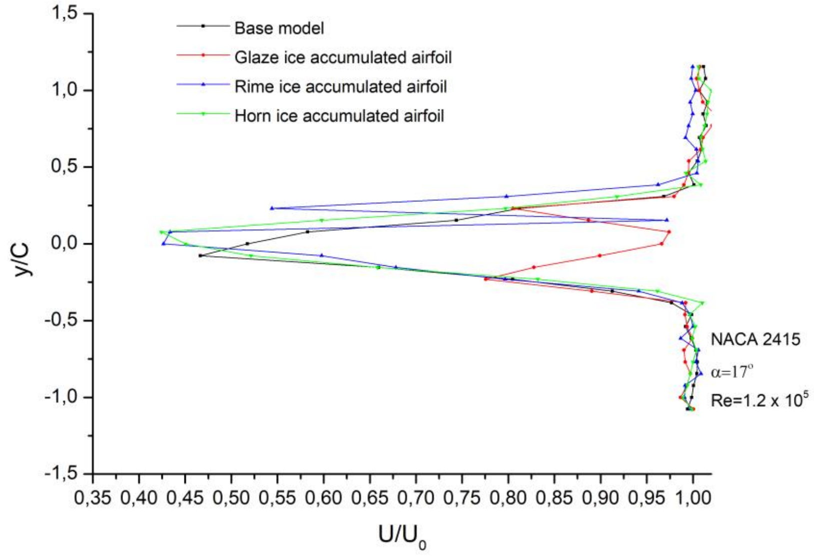

Figure 62. Wake profile of the test models at 17° angle of attack

The RIA, HIA and base models show the lowest U/U_o values close to the TE of the airfoils. While this value for the HIA was above the TE, for both the RIA and base models, it was below the TE. A wide double-peak behavior was observed for the GIA airfoil model at the stall angle. Finally, Figure 63 shows the wake profiles of the test models at α = 20°. A very weak double-peak behavior was spotted only for the RIA airfoil. All models had the lowest U/U_o values close to the TE. The narrowest wake width was attributed to the GIA airfoil. In addition, the largest wake width profile was observed in Figure 63 for the RIA model.

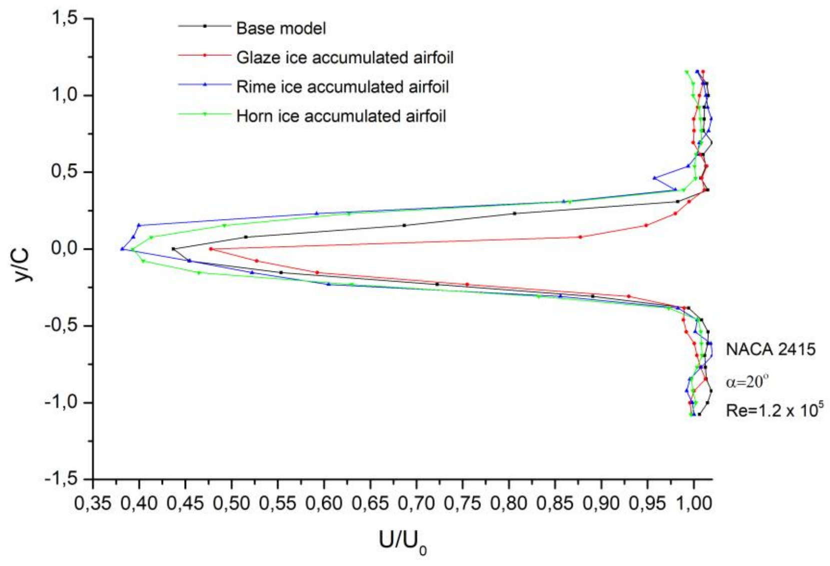

Figure 63. Wake profile of the test models at a 20° angle of attack

In this section, the following figures show the TiO_2 oil flow visualization results for all the test models at seven different attack angles, as stated above the models. The "S" in figures represents the suction side of the airfoil and "P" is to abbreviate the pressure side of the airfoil. Furthermore, S/C is defined as the span-over-chord, whereas x/C states any "x" location in terms of the chord length. U_∞ represents the free stream velocity, and the arrow below it shows the direction of the flow.

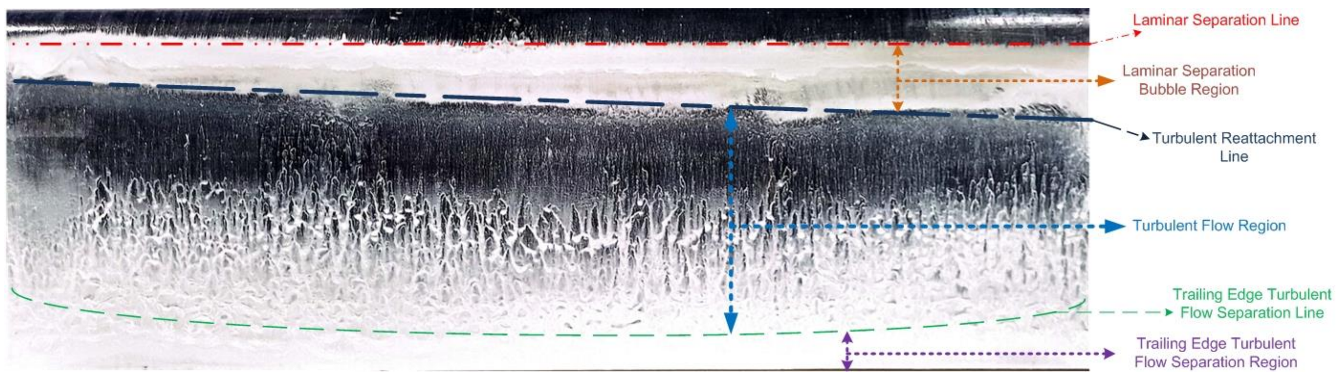

Figure 64. Oil flow visualization results of the baseline model at α = 8°

Figure 65 shows the oil flow visualization results of the baseline model. For the suction side at α = 0°, the black area extending up to x/C = 0.2 over the surface of the airfoil represents the laminar flow region. Afterwards, laminar separation bubble (LSB) can be observed at the midpoint of the airfoil until about x/C = 0.7 where turbulent reattachment points are shown.

The LSB is the region between the laminar flow separation and the turbulent reattachment line. Moreover, the turbulent flow region can be observed ahead of the turbulent reattachment points. The turbulent flow separation region can be observed around the TE of the baseline model. As angle of attack increased to 4°, the LSB and turbulent reattachment line were clearly obtained. By further increasing the attack angle to 8°, the LSB moved toward the LE and shrunk compared to previous attack angles. Additionally, the position of turbulent separation line moved toward the LE and the turbulent separation region widened. At α = 13°, the position of LSB shifted to close proximity to the LE of the airfoil. The turbulent flow region tends to shrink as attack angle increases. The turbulent flow separation line can be observed around x/C = 0.6. Moreover, the turbulent separation region increased substantially.

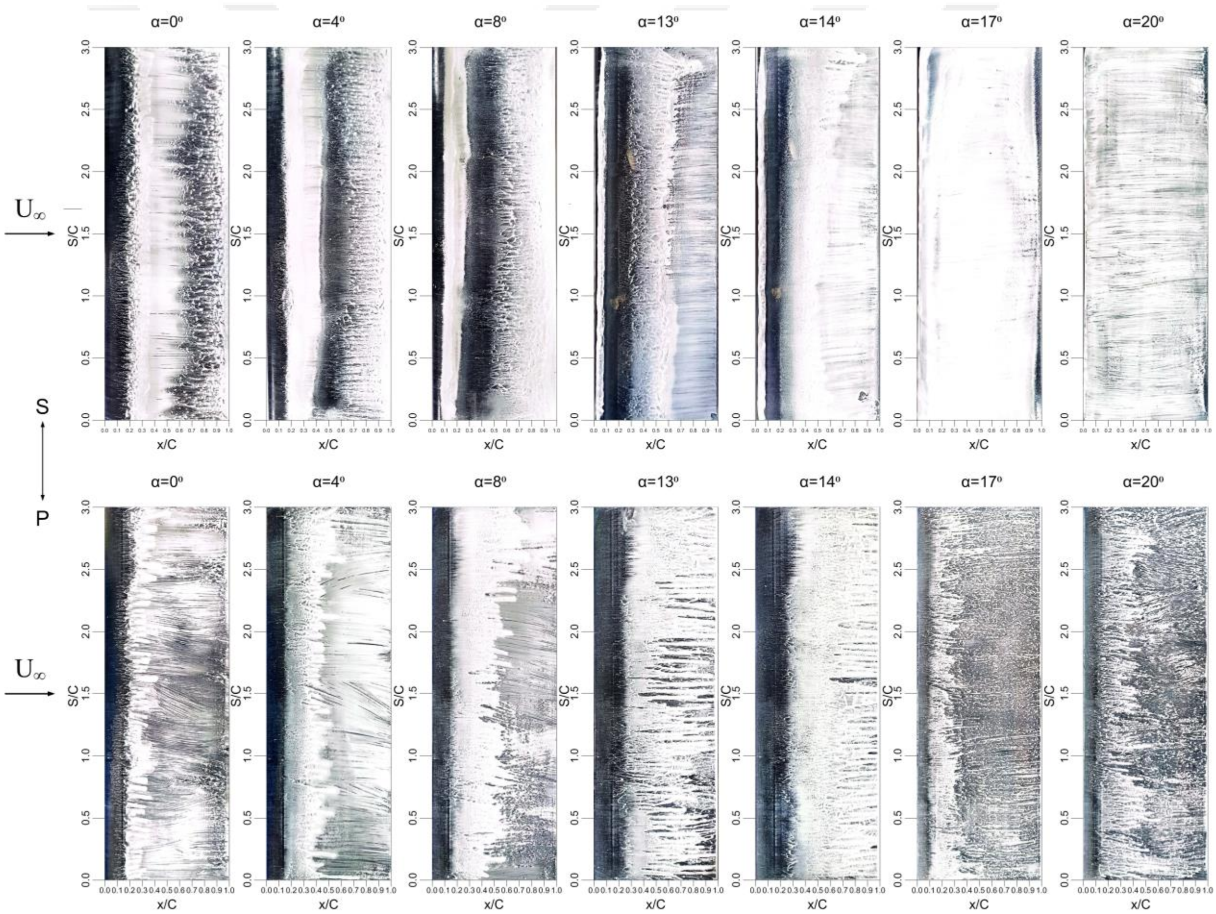

Figure 65. TiO_2 oil flow visualization of base model at different angles of attack

For an angle of attack of 14°, LSB remained almost unchanged. Whereas the width of turbulent flow region has decreased and turbulent flow separation region increased. Since α = 14° is the stall angle of the baseline model, the flow was separated from suction side of the airfoil for at 17° and 20° attack angles. The black regions at the TE of the airfoil at these angles are reverse flows induced from the pressure side of the airfoil. Figure 66 represents the oil flow visualization results of the GIA airfoil for selected angles of attack. At α = 0°, a laminar flow region can be observed between x/C = 0.1 and x/C = 0.2. The LSB structure was effective at the midpoint of the airfoil up to turbulent reattachment points scattered around 0.5 and x/C = 0.8. Finally, the turbulent flow region can be noticed afterwards. Increasing α = 4°, the laminar flow region grew and the LSB has shrunk. The turbulent flow region can be clearly observed around x/C = 0.4 to x/C = 0.9. Due to the randomness of glaze ice accumulation, the laminar separation line at α = 8° seems to be different spanwise in contrast to the former attack angles. The turbulent flow region of the GIA model is spread around the surface. Moreover, a turbulent flow separation region was observed between x/C = 0.6 and TE along the airfoil span.

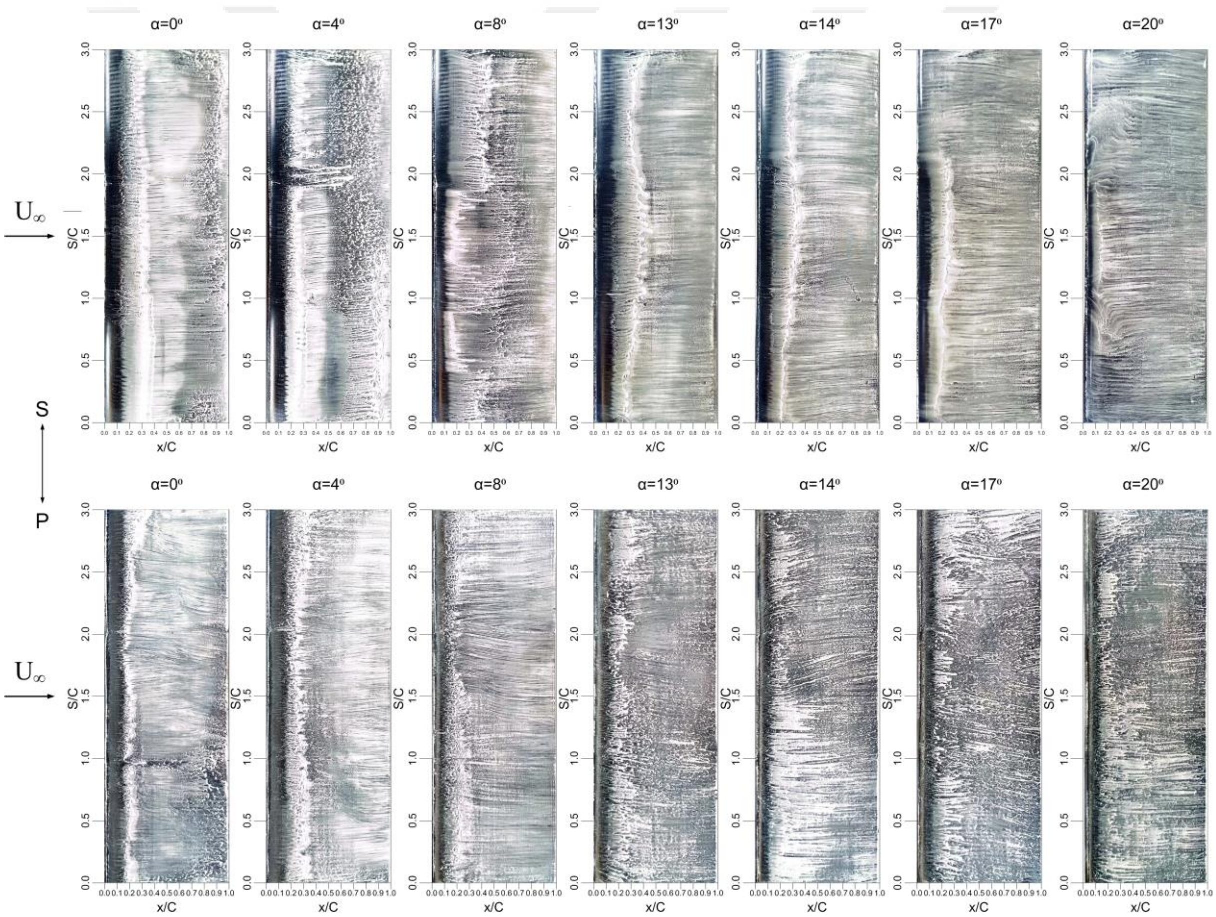

Figure 66. TiO_2 oil flow visualization of the GIA model at different attack angles

The laminar flow region decreased as the angle of attack increased from 13° to 14°. Conversely, the turbulent flow separation region was increased. Additionally, the position of the turbulent separation line moved toward the LE. In Figure 66, it can be observed that, a small pocket of laminar flow at an attack angle of 17° for the GIA airfoil. Consequently, this result clearly supports the force measurement results. Furthermore, at α = 20°, a relatively complete flow separation was observed for the GIA airfoil. Figure 67 shows the TiO_2 oil flow visualization images of the HIA airfoil. For an attack angle of 0°, a small LSB was observed around the LE of the airfoil. The position of turbulent flow reattachment line can be observed between x/C = 0.2 and x/C = 0.4. A large region of turbulent flow appears over the surface of the airfoil. Moreover, the turbulent flow separation region is prominent around x/C = 0.8 to x/C = 1.0. When the angle of attack was increased to 4°, the size of the LSB increased. The turbulent reattachment points moved toward the LE and the turbulent flow region decreased for the HIA airfoil. A large region of turbulent flow separation can be observed starting from x/C = 0.4 to x/C = 1.0 at an attack angle of 4°.

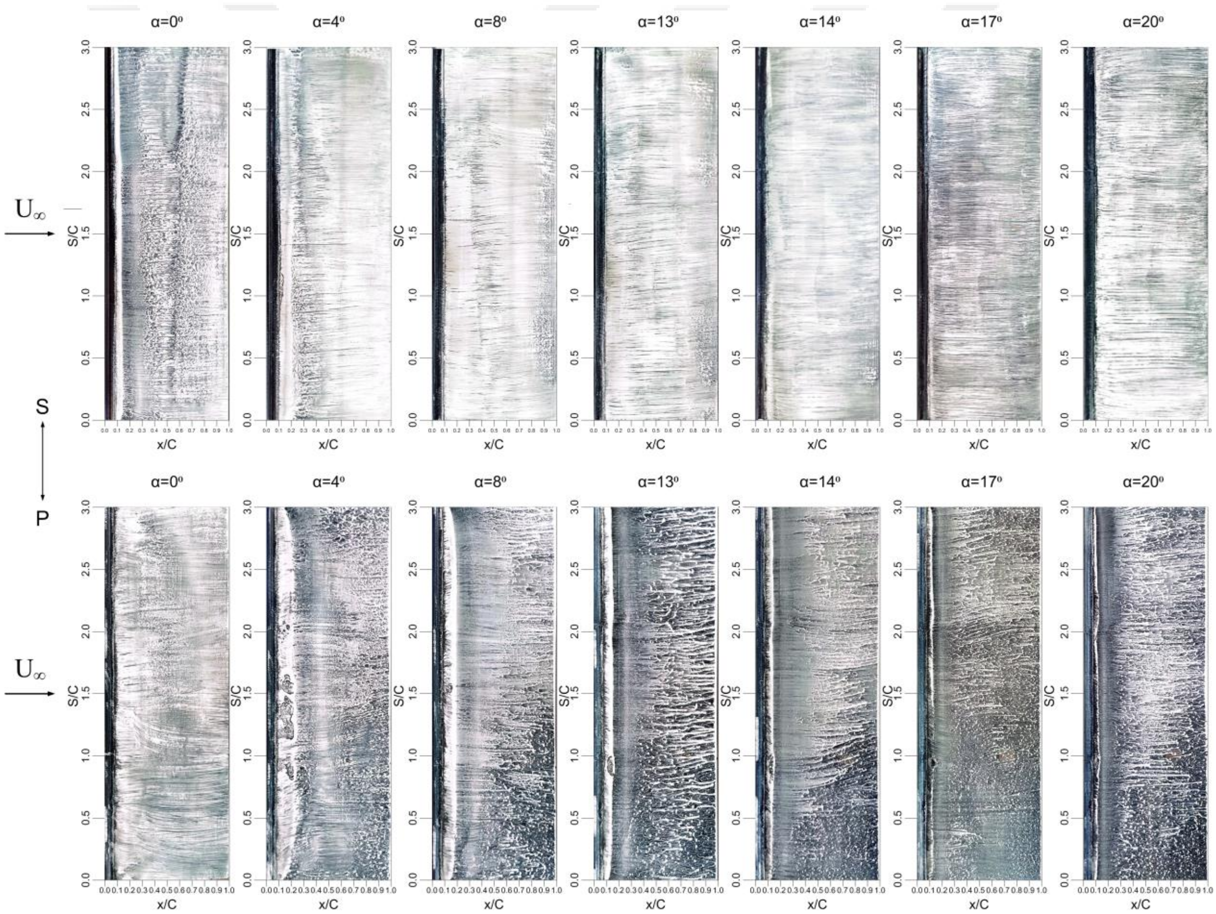

Figure 67. TiO_2 oil flow visualization of HIA model at different attack angles

Further angles of attack for the HIA airfoil will not be discussed since flow separates completely from the surface of the airfoil. Figure 68 illustrates the oil flow visualization results of the RIA model. At α = 0°, a laminar separation line can be clearly observed at x/C = 0.2. Turbulent reattachment points are spread from x/C = 0.6 to x/C = 0.9. The LSB is on the right side of the upper surface appeared to be more prominent. When the angle of attack was increased to 4°, the laminar separation line moved toward the TE of the RIA airfoil model. In addition, the turbulent reattachment points are shifted to the LE. The turbulent flow separation line starts closer to LE on the left side of the upper surface. At α = 8°, the position of laminar separation line shifted toward the LE of the RIA airfoil. The LSB can be precisely observed on the surface of the airfoil. Furthermore, the size of the LSB observe to be smaller on the left side than on the right side. This condition also affects the turbulent flow region. Between S/C = 0.0 and S/C = 1.0 small regions of turbulent flow can be noticed. However, exceeding S/C = 1.0, the turbulent flow region inclined to disappear around S/C = 0.8.

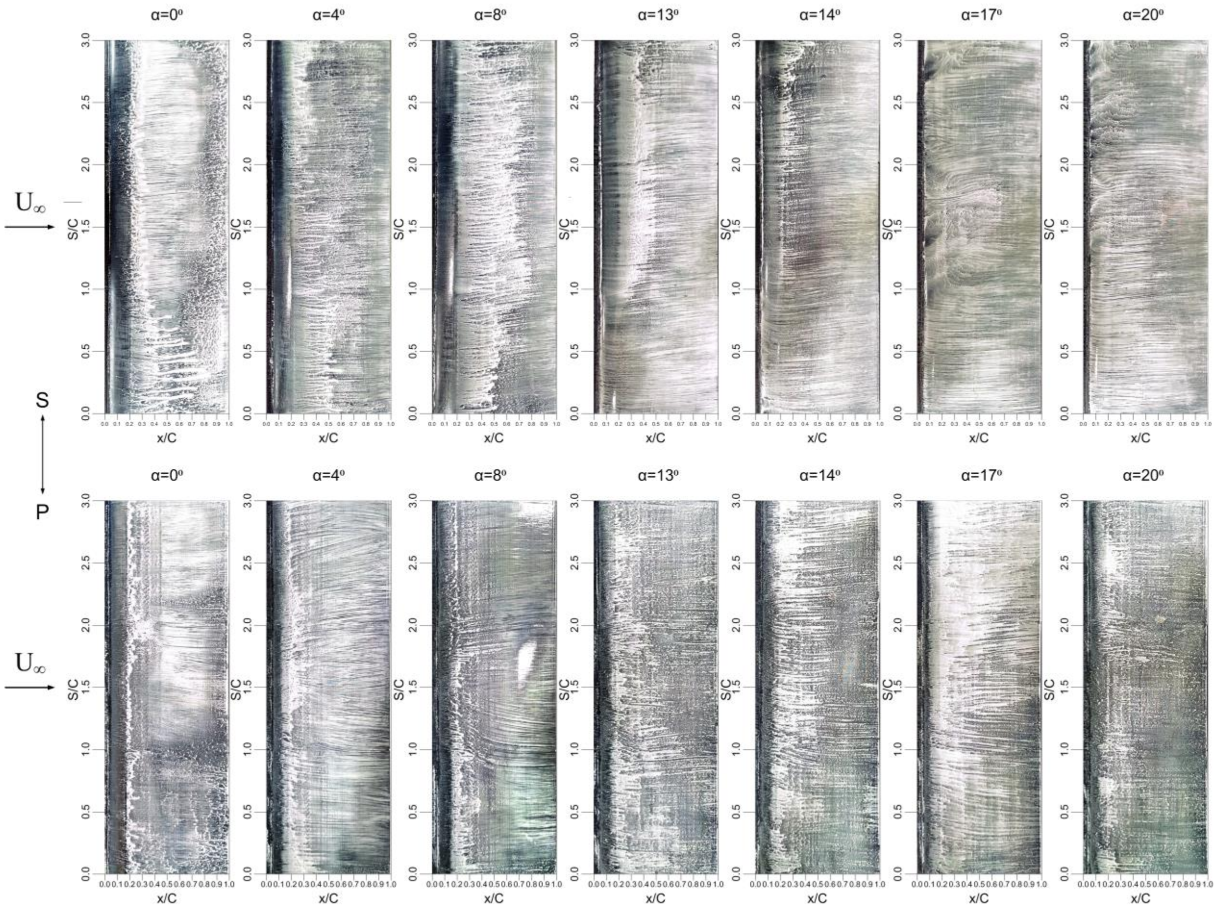

Figure 68. TiO_2 oil flow visualization of the RIA model at different attack angles

Additionally, some small pockets of the turbulent flow region can be observed on the right side of the airfoil where the size of the LSB shrinks. As the angle of attack increased to 13°, the laminar flow region decreased along the range between S/C = 1.0 to S/C =3.0 and disappeared below 1.0 S/C. At α = 14°, a small region of laminar flow was observed around S/C = 2.5 to S/C = 3.0. From S/C = 1.0 to S/C = 3.0, the laminar separation line was distinguishable. A very small LSB can seen between S/C = 2.0 and S/C = 3.0. Moreover, small pockets of turbulent flow region can be observed around S/C = 1.5 and S/C = 3.0. For further attack angles, the flow over the suction side of the RIA airfoil was separated. Some disturbances in the oil were caused, possibly due to production errors.

5. CONCLUSIONS

The degradation of the aerodynamic performance due to three different types of ice accumulation on the NACA 2415 airfoil was investigated in this thesis. Icing environments, icing types, the effects of icing on airfoil, and aircraft components as well as anti-icing and deicing methods are briefly discussed. The experiments were conducted on the base airfoil and glaze, rime, and horn ice accumulated airfoils at $Re = 1.2 \times 10^5$. In this thesis, force and velocity measurements and oil and smoke-wire flow visualization techniques were performed. Attack angles ranging between -7° and 23° were selected for the force measurement experiments. Moreover, seven different angles of attack including 0°, 4°, 8°, 13°, 14°, 17°, and 20° were chosen from the force experiment results for velocity measurements and flow visualization experiments to represent both the pre-stall, stall and post-stall conditions of the investigated models.

The force measurement results showed that, a shift in the stall angle was observed for all the ice accumulated models compared with the baseline model. A positive shift of 3° was noted in the GIA model, whereas a negative shifts of 1° and 8° were observed in the RIA and HIA models, respectively. Both the GIA and RIA airfoils showed smoother stall characteristics than the base airfoil. In general, the C_{Lmax} values of the ice accumulated models decreased as expected. A 20%, 23%, and 88% decrease in the maximum lift coefficient was observed in the GIA, RIA, and HIA models, respectively. The increase in drag coefficients at $\alpha = 0°$ for the GIA, RIA and HIA airfoils were 14%, 4% and 307%, respectively.

Velocity measurements and smoke-wire flow visualization results confirm that the HIA airfoil has the widest wake profile expect at $\alpha = 20°$. Double-peak behavior was observed in the GIA, RIA and base models at higher attack angles. Overall, the lowest U/U_o values for the HIA airfoil was noted around the TE of the airfoil. Moreover, the RIA and base models showed the second widest wake profiles among all models at stall angles of 13° and 14°, respectively.

TiO_2 oil flow visualization results showed that for base airfoil, as the angle of attack increased, the size of LSB decreased and the position of LSB moved toward the LE of the airfoil. Additionally, the size of the turbulent flow region also decreased. In contrast, the turbulent flow separation region grew significantly as the attack angle increased. For the GIA model, the appearance of the LSB on the surface of the airfoil was weak, possibly due to the laminar to turbulent transition induced by glaze ice accumulation on the LE of the airfoil model. At α =

8°, the turbulent flow region was observed to be distributed around the upper surface of the GIA airfoil. As the angle of attack increased from 13° to 17°, the laminar flow region on the surface of the GIA airfoil shrunk. For attack angles of 0° and 4°, a small LSB formed around the LE of the HIA airfoil. At $\alpha = 0°$, the turbulent flow region dominated over the suction side of the HIA airfoil. This was significantly reduced when the attack angle was increased to 4°. The RIA airfoil showed a similar laminar flow region between the attack angles of 0° to 8°. Due to the randomness of the rime ice shape, the left and right sides of the airfoil exhibited different flow characteristics.

6. FUTURE WORKS AND RECOMMENDATIONS

Further investigations should be carried out to test the ice accumulation on the airfoil for considering a larger range of Reynolds numbers and moment coefficients. Moreover, the pressure measurements can be performed to enlighten aerodynamic performance changes.

REFERENCES

[1] Bragg M.B., Gregorek G.M. and Lee J.D. (1986). “Airfoil aerodynamics in icing conditions”, Journal of Aircraft, 23, pp. 76-81.

[2] Gray V.H. (1958). "Correlations among ice measurements, impingement rates, icing conditions, and drag coefficients for unswept NACA 65A004 airfoil", NACA TN 4151.

[3] Gray V.H. and von Glahn U.H. (1957). "Aerodynamic effects caused by icing of an unswept NACA 65A004 airfoil”, NACA TN 4155. by Icing of an Unswept NACA 65A004 Airfoil," NACA TN 4155.

[4] https://www.ecfr.gov/current/title-14/chapter-I/subchapter-C/part-25/appendix-Appendix%20C%20to%20Part%2025

[5] www.britannica.com/science/weather

[6] https://www.weather.gov/source/zhu/ZHU_Training_Page/icing_stuff/icing/icing.htm

[7] Thomas S.K., Cassoni R.P. and MacArthur C.D. (1996). “Aircraft anti-icing and de-icing techniques and modeling”, Journal of Aircraft, 33(5), pp. 841-854.

[8] Aircraft Icing Handbook (1991), DOT/FAA/CT-88/8- I.

[9] Ruff G.A. and Berkowitz B.M. (1990). “Users manual for the NASA lewis ice accreation prediction code (LEWICE)”, NACA CR 185129.

[10] Avery A.S. and Jacob J.D. (2017). “Evaluation of low altitude icing conditions for small unmanned aircraft”, 9th AIAA Atmospheric and Space Environments Conference, Denver, Colorado, pp. 1-13.

[11] https://safetyfirst.airbus.com/look-out-for-ice-ridges-on-the-lower-nose-fuselage/#:~:text=Ice%20ridges%20on%20the%20lower%20nose%20fuselage%20can%20cause%20Computed,how%20to%20prevent%20such%20situation.

[12] https://skybrary.aero/articles/flight-icing

[13] https://aircrafticing.grc.nasa.gov/2_2_2_1.html

[14] Preston G.M. and Blackman C.C. (1948). “Effects of ice formations on airplane performance”, NACA TN 1598, pp. 1-37.

[15] https://aeropeep.com/anti-ice/

[16] https://aircrafticing.grc.nasa.gov/1_2_4_2.html

[17] Steuernagle J., Roy K. and Wright D. (2008). “Aircraft icing”, Aircraft owners and Pilots Association Safety Advisor, Weather No. 1, Frederick, MD.

[18] Fortin G. and Perron J. (2009). “Wind turbine icing and de-icing”, 47th AIAA Aerospace Sciences Meeting Including the New Horizons Forum and Aerospace Exposition, Orlando, Florida, pp. 1-23.

[19] Anderson D.N. and Reich A.D. (1997). "Tests of performance coatings for low ice adhesion", 35th AIAA Aerospace Sciences Meeting and Exhibit, Reno, NV, pp. 1-12.

[20] Laforte J.L., Allaire M.A. and Laflamme J. (1998). "State-of-the-art on power line de-icing", Atmospheric Research, 46, pp. 143-158.

[21] Kraj A.G. and Bibeau E.L. (2006). "Impact of mitigation strategies on icing accumulation rate for wind turbines in cold climates", Canadian Wind Energy Association, Ottawa, ON, pp. 1-26.

[22] Pauw D.D. and Dolatabadi A. (2017). "Effect of superhydrophobic coating on the anti-icing and deicing of an airfoil", Journal of Aircraft, 54(2), pp. 1-10.

[23] Laakso T., Baring-Gould I., Durstewitz M., Horbaty R., Lacroix A., Peltola E., Ronsten G., Tallhaug L. and Wallenius T. (2003). "State-of-the-art of wind energy in cold climates", VTT Working Papers, 1459, pp. 1-71.

[24] Battisti L., Fedrizzi R., Brighenti A. and Laakso T. (2006). "Sea ice and icing risk for offshore wind turbines", Owemes, Citavecchia, Italy, pp. 1-10.

[25] Seifert H. (2003). "Technical requirements for rotor blades operating in cold climate", BOREAS VI. FMI, Pyhätunturi, Finland, pp. 1-13.

[26] Lacroix A. and Manwell J.F. (2000). "Wind energy: cold weather issues", Enviromental Science, pp. 1-17.

[27] Moghtadernejad S., Tembely M., Jadidi M., Esmail N. and Dolatabadi A. (2015). "Shear driven droplet shedding and coalescence on a superhydrophobic surface", Physics of Fluids, 27(3), pp. 1-19.

[28] Zeng D., Li Y., Liu H., Yang Y., Peng L., Zhu C. and Zhao N. (2023). "Superhydrophobic coating induced anti-icing and deicing characteristics of an airfoil", Colloids and Surfaces A: Physicochemical and Engineering Aspects, 660, pp. 1-10.

[29] Planquart P., Borre G.V. and Buchlin J.M. (2005). "Experimental and numerical optimization of a wing leading edge hot air anti-icing system", 43rd AIAA Aerospace Sciences Meeting and Exhibit, Reno, NV, pp. 1-8.

[30] Hannat R. and Morency F. (2014). "Numerical validation of conjugate heat transfer method for anti-/de-icing piccolo system", Journal of Aircraft, 51(1), pp. 104-116.

[31] Reid T., Baruzzi G.S. and Habashi W.G. (2012). "FENSAP-ICE: Unsteady conjugate heat transfer simulation of electrothermal de-icing", Journal of Aircraft, 49(4), pp. 1101-1109.

[32] Bu X., Lin G., Yu J., Yang S. and Song X. (2012)." Numerical simulation of an airfoil electrothermal anti-icing system", Journal of Aerospace Engineering, 227(10), pp. 1608-1622.

[33] Al-Khalil K.M., Ferguson T.W. and Phillips D.M. (1997). "A hybrid anti-icing ice protection system", 35th AIAA Aerospace Sciences Meeting and Exhibit, Reno, NV, pp. 1-8.

[34] Uranai S., Fukudome K., Mamori H., Fukushima N. and Yamamoto M. (2020). "Numerical simulation of the anti-icing performance of electric heaters for icing on the NACA 0012 airfoil", Aerospace, 7(9), pp. 1-15.

[35] Zhou W., Liu Y., Hu H., Hu H. and Meng X. (2018). "Utilization of thermal effect induced by plasma generation for aircraft icing mitigation", AIAA Journal, 56(3), pp. 1-8.

[36] Chen J., Liang H., Wu Y., Wei B., Zhao G., Tian M. and Xie L. (2018). "Experimental study on anti-icing performance of NS-DBD plasma actuator", Applied Sciences, 8(10), pp. 1-15.

[37] Tian Y., Zhang Z., Cai J., Yang L. and Kang L. (2018). "Experimental study of an anti-icing method over an airfoil based on pulsed dielectric barrier discharge plasma", Chinese Journal of Aeronautics, 31(7), pp. 1449-1460.

[38] Pellicano P. and Riley J.T. (2007). "Residual and inter-cycle ice for lower-speed aircraft with pneumatic boots", 45th AIAA Aerospace Sciences Meeting and Exhibit, Reno, NV, pp. 1-8.

[39] Abdelghany E.S., Farghaly M.B., Almalki M.M., Sarhan H.H. and Essa M.E.M. (2023). "Machine learning and iot trends for intelligent prediction of aircraftwing anti-icing system temperature", Aerospace, 10(8), pp. 1-34.

[40] Akbıyık H., Yavuz H. and Akansu Y.E. (2017). "Comparison of the linear and spanwise-segmented dbd plasma actuators on flow control around a naca0015 airfoil", IEEE Transactions on Plasma Science, 45(11), pp. 2913-2921.

[41] Meng X., Cai J., Tian Y., Han X., Zhang D. and Hu H. (2016). "experimental study of deicing and anti-icing on a cylinder by dbd plasma actuation", 47th AIAA Plasmadynamics and Lasers Conference, Washington, D.C., pp. 1-14.

[42] Unfer T. and Boeuf J.P. (2009). "Modelling of a nanosecond surface discharge actuator", Journal of Physics D: Applied Physics, 42, pp. 1-12.

[43] Weisend Jr. N.A. (1989). "Design of an advanced pneumatic deicer for the composite rotor blade", Journal of Aircraft, 26(10), pp. 947-950.

[44] Hochart C., Fortin G. and Perron J. (2008). "Wind turbine performance under icing conditions", Wind Energy, 11, pp. 319-333.

[45] Etemaddar M., Hansen M.O.L and Moan T. (2014). "Wind turbine aerodynamic response under atmospheric icing conditions", Wind Energy, 17, pp. 241-265.

[46] Gao L., Liu Y. and Hu H. (2019). "An experimental investigation of dynamic ice accretion process on a wind turbine airfoil model considering various icing conditions", International Journal of Heat and Mass Transfer, 133, pp. 930-939.

[47] Shin J. and Bond T.H. (1992). "Experimental and computational ice shapes and resulting drag increase for a naca 0012 airfoil", The Fifth Symposium on Numerical and Physical Aspects of Aerodynamic Flows, California State University, pp. 1-10.

[48] Chung J.J. and Addy Jr. H.E. (2000). "A numerical evaluation of icing effects on a natural laminar flow airfoil", 38th AIAA Aerospace Sciences Meeting and Exhibit, Reno, NV, pp. 1-13.

[49] Addy Jr. H.E., Broeren A.P., Zoeckler J.G. and Lee S. (2003). "A wind tunnel study of icing effects on a business jet airfoil", 41st AIAA Aerospace Sciences Meeting and Exhibit, Reno, NV, pp. 1-19.

[50] Broeren A.P., Bragg M.B. and Addy Jr. H.E. (2004). "Effect of intercycle ice accreations on airfoil performance", Journal of Aircraft, 41(1), pp. 165-174.

[51] Alvarado-Robles G., Osornio-Ríos R.A., Solís-Muñoz F.J. and Morales-Hernández L.A. (2021). "An approach for shadow detection in aerial images based on multi-channel statistics", IEEE Access, 9, pp. 34240-34250.

[52] Inoue J. and Curry J.A. (2004). "Application of Aerosondes to high-resolution observations of sea surface temperature over Barrow Canyon", Geophysical Research Letters, 31, pp. 1-4.

[53] Hacker P.T. and Dorsch R.G. (1951). "A summary of meteorological conditions associated with aircraft icing and a proposed method of selecting design criterions for ice-protection equipment", NACA TN 2569, pp. 1-33.

[54] Li T., Zhang B., Cheng X., Hui F. and Li Y. (2021). "Leveraging the UAV to support Chinese Antarctic expeditions: a new perspective", Advances in Polar Science, 32, pp. 67-74.

[55] Li L., Liu Y., Zhang Z. and Hu H. (2019). "Effects of thermal conductivity of airframe substrate on the dynamic ice accretion process pertinent to UAS inflight icing phenomena", 131, pp. 1184-1195.

[56] Szilder K. and McIlwain S. (2011). "In-flight icing of uavs - the influence of Reynolds number on the ice accretion process", SAE International, pp. 1-13.

[57] Szilder K. and Yuan W. (2017). "In-flight icing on unmanned aerial vehicle and its aerodynamic penalties", Progress in Flight Physics, 9, pp. 173-188.

[58] Hann R., Hearst R.J., Sætran L.R. and Bracchi T. (2020). "Experimental and numerical icing penalties of an s826 airfoil at low reynolds numbers", Aerospace, 7(4), pp. 1-18.

[59] Houghton E.L. and Carpenter P.W. (2003). "Aerodynamics for Engineering Students", Butterworth-Heinemann, 5th edition, Oxford, Great Britain.

[60] Barlow J.B., Rae W.H. and Pope A. (1999). "Low-speed wind tunnel testing", 3rd edition, John Wiley & Sons, New York Usa.

[61] Maltby and Keating 1962. "The surface oil flow technique for use in low speed wind tunnels", Flow Visualization In Wind Tunnels Using Indicators, pp. 1-29.

[62] Sudhakar S., Karthikeyan N. and Suriyanarayanan P. (2019). "Experimental studies on the effect of leading-edge tubercles on laminar separation bubble", AIAA Journal, 57(12), pp. 1-11.

[63] Seyhan M. and Sarioglu M. (2021). “Investigation of drag reduction performance of half NACA 0009 and 0012 airfoils placed over a trailer on the flow around truck-trailer”, Journal of Mechanical Science and Technology, 35(7), pp. 2971-2979.

[64] Coleman H.W. and Steele W.G. (1995). “Engineering application of experimental uncertainty analysis”, AIAA Journal, 33(10), pp. 1888-1896.

[65] Akbıyık H., Yavuz H. and Akansu Y.E. (2020). “Aerodynamic and energy-efficiency-based assessment of plasma actuator's position on a NACA0015 airfoil”, Contribution to Plasma Physics, 60(2), pp. 1-15.

[66] Genç. M.S., Karasu I. and Açıkel H.H. (2012). “An experimental study on aerodynamics of NACA2415 aerofoil at low Re numbers”, Experimental Thermal and Fluid Science, 39, pp. 252-264.

[67] Ericsson L.E. and Reding J.P. (1969). “Unsteady airfoil stall”, NASA Report CR-66787, Hannover, MD, USA.

[68] Lissaman P.B.S. (1983). “Low-reynolds-number airfoils”, Annular Review of Fluid Mechanics, 15, pp. 223-239.

APPENDIX

In this study, the uncertainty values of the measured and calculated parameters were determined by the methods presented by Coleman and Steele [64]. The experimental parameters are functions of the form of equation E-3.

$$r = kX_1^a X_2^b X_3^c \ldots \tag{E-3}$$

The uncertainty expression of the function in this form is expressed in equation E-4.

$$u_r = \frac{w_r}{r} = \left[a^2\left(u_{x_1}\right)^2 + b^2\left(u_{x_2}\right)^2 + c^2\left(u_{x_3}\right)^2 + \cdots\right]^{1/2} \tag{E-4}$$

Within the scope of this study, parameters such as velocity, force, density, temperature etc. were measured experimentally and calculated for the Re number and lift and drag coefficients using these measurement results.

Determination of the uncertainty of the parameters used in this thesis

The uncertainties of dependent and independent variables used in this thesis such as, atmospheric pressure (P), temperature (T), airfoil chord and span length, drag and lift force, dynamic viscosity, velocity measured by hot-wire anemometer are to be measured. Here, the user manuals of measurement devices used to determine the uncertainties of independent variables.

An error of 1 kPa may occur in the measurement of 85 kPa atmospheric pressure. In this case, the uncertainty of atmospheric pressure is obtained as 1.1%.

$$u_{Patm} = \frac{w_{Patm}}{P_{atm}} \cong \frac{1000}{85000} = 0.011 = \%1.1 \tag{E-5}$$

It is stated in the user manual that the temperature probe of the Manoair500 model micromanometer used in temperature measurement has an error of 0.2°C in the range of 0-

70°C. In this case, in the measurement of temperature at 27°C, the temperature uncertainty is obtained as 0.0666%.

$$u_T = \frac{w_T}{T} \cong \frac{0.2}{300} = 0.000666 = \%0.0666 \qquad \text{(E-6)}$$

The uncertainty caused by a 0.3 mm error in measuring the chord lengths (C) of a 150 mm and 130 mm airfoil is 0.2% and 0.23%, respectively.

$$u_C = \frac{w_C}{C} \cong \frac{0.3}{150} = 0{,}002 = \%0.2 \qquad \text{(E-7)}$$

$$u_C = \frac{w_C}{C} \cong \frac{0.3}{130} = 0{,}0023 = \%0.23 \qquad \text{(E-8)}$$

The uncertainty caused by a 0.5 mm error in measuring the span lengths (S) of a 450 mm and 390 mm airfoil is 0.11% and 0.13%, respectively

$$u_S = \frac{w_S}{S} \cong \frac{0.5}{450} = 0{,}0011 = \%0.11 \qquad \text{(E-9)}$$

$$u_S = \frac{w_S}{S} \cong \frac{0.5}{390} = 0{,}0013 = \%0.13 \qquad \text{(E-10)}$$

The uncertainty in the dynamic viscosity of air at 25°C with a 2°C change is 0.51%.

$$u_\mu = \frac{w_\mu}{\mu} \cong 0.00508 = \%0.51 \qquad \text{(E-11)}$$

The uncertainty for density depends on the atmospheric pressure and temperature. Equation for uncertainty of density;

$$u_\rho = \frac{w_\rho}{\rho} = \left[(1)^2\left(\frac{w_{Patm}}{Patm}\right)^2 + (-1)^2\left(\frac{w_T}{T}\right)^2\right]^{1/2} \qquad \text{(E-12)}$$

By writing the uncertainty values of atmospheric pressure and temperature in Equation E-12, the uncertainty of the density is obtained as uρ ≅ 0.011 or 1.1%.

Uncertainty values affecting the drag and lift force coefficient were obtained for U_o = 14.48 m/s (Re = 1.2 x 10^5).

The uncertainty value of the load cell in force measurement is 1% in the x and y-direction.

$$u_{X_1} = \frac{w_{X1}}{X_1} \cong 0.01 = \%1 \qquad \text{(E-13)}$$

The uncertainty in force measurement due to a 1° error in the angle of attack is 0.6%.

$$u_{X_2} = \frac{w_{X2}}{X_2} \cong 0.006 = \%0.6 \qquad \text{(E-14)}$$

The uncertainty due to data acquisition card resolution is 0.34%.

$$u_{X_3} = \frac{w_{X3}}{X_3} \cong 0.0034 = \%0.34 \qquad \text{(E-15)}$$

During the calibration process, the uncertainties in the calculation of the forces acting on the end plate and model holder rod were taken as approximately 3%.

$$u_{X_4} = \frac{w_{X4}}{X_4} \cong 0.03 = \%3 \qquad \text{(E-16)}$$

Taking these uncertainties into consideration, the total uncertainty in drag and lift force measurement is;

$$u_{F_D} = \frac{W_{F_D}}{F_D} = \left[(\frac{w_{X_1}}{X_1})^2 + (\frac{w_{X_2}}{X_2})^2 + (\frac{w_{X_3}}{X_3})^2 + (\frac{w_{X_4}}{X_4})^2\right]^{1/2} \qquad \text{(E-17)}$$

$$u_{F_D} = \frac{W_{F_D}}{F_D} = [(0.01)^2 + (0.006)^2 + (0.0034)^2 + (0.03)^2]^{1/2} = 0.032 = \%3.2$$

$$u_{F_L} = \frac{W_{F_L}}{F_L} = \left[(\frac{w_{X_1}}{X_1})^2 + (\frac{w_{X_2}}{X_2})^2 + (\frac{w_{X_3}}{X_3})^2 + (\frac{w_{X_4}}{X_4})^2\right]^{1/2} \qquad \text{(E-18)}$$

$$u_{F_L} = \frac{W_{F_L}}{F_L} = [(0.01)^2 + (0.006)^2 + (0.0034)^2 + (0.03)^2]^{1/2} = 0.032 = \%3.2$$

Uncertainty values affecting speed measurement with hot-wire anemometer were obtained for U_0 = 14.42 m/s (Re = 1.2 x 10^5).

Uncertainties related to the anemometer; Uncertainties due to noise, repeatability and frequency perception are around 0.5%

$$u_{X_5} = \frac{w_{X_5}}{X_5} \cong 0.005 = \%0.5 \tag{E-19}$$

In the calibration process, at a speed of 14.42 m/s, the uncertainty in the calibration device is 5.1%.

$$u_{X_6} = \frac{w_{X_6}}{X_6} \cong 0.051 = \%5.1 \tag{E-20}$$

Uncertainty resulting from the linearization or calibration curve process is 0.3%.

$$u_{X_7} = \frac{w_{X_7}}{X_7} \cong 0.003 = \%3 \tag{E-21}$$

The uncertainty in velocity due to a 1° error in the probe position is 0.009%.

$$u_{X_8} = \frac{w_{X_8}}{X_8} \cong 0.00009 = \%0.009 \tag{E-22}$$

The uncertainty in velocity due to a 2°C temperature change in the probe operating temperature is 1.53%.

$$u_{X_9} = \frac{w_{X_9}}{X_9} \cong 0.0153 = \%1.53 \tag{E-23}$$

The uncertainty in velocity due to a 2°C temperature change in air density is 0.39%.

$$u_{X_{10}} = \frac{w_{X_{10}}}{X_{10}} \cong 0.0039 = \%0.39 \tag{E-24}$$

The uncertainty in velocity due to a 1 kPa change in atmospheric pressure is 0.68%.

$$u_{X_{11}} = \frac{w_{X_{11}}}{X_{11}} \cong 0.0068 = \%0.68 \quad \text{(E-25)}$$

Taking the uncertainties above into consideration, the total uncertainty in velocity measurement is;

$$u_{U_{CTA}} = \frac{W_{U_{CTA}}}{U_{CTA}} = \left[(\frac{w_{X_5}}{X_5})^2 + (\frac{w_{X_6}}{X_6})^2 + (\frac{w_{X_7}}{X_7})^2 + (\frac{w_{X_8}}{X_8})^2 + (\frac{w_{X_9}}{X_9})^2 + (\frac{w_{X_{10}}}{X_{10}})^2 + (\frac{w_{X_{11}}}{X_{11}})^2\right]^{1/2} \quad \text{(E-26)}$$

$$u_{U_{CTA}} = \frac{W_{U_{CTA}}}{U_{CTA}} = [(0.005)^2 + (0.051)^2 + (0.003)^2 + (0.00009)^2 + (0.0153)^2 + (0.0039)^2 + (0.0068)^2]^{1/2} \cong 0.05413 = \%5.4$$

Calculation of uncertainty values of dimensionless numbers

The uncertainty value for the Re number varies depending on the value of ρ, U_{CTA}, C and μ.

$$u_{RE} = \frac{W_{RE}}{RE} = \left[(u_\rho)^2 + (u_{U_{CTA}})^2 + (u_C)^2 + (u_\mu)^2\right]^{1/2} \quad \text{(E-27)}$$

The uncertainty value of the Reynolds number is determined above; It is calculated by substituting the uncertainty of density, velocity, characteristic length and dynamic viscosity into equation E-27.

$$u_{RE} = \frac{W_{RE}}{RE} = [(0.011)^2 + (0.05413)^2 + (0.002)^2 + (0.00508)^2]^{1/2} = 0.055 = \%5.5$$

To determine the uncertainty of lift and drag coefficients;

$$u_{C_L} = \frac{W_{C_L}}{C_L} = \left[(u_\rho)^2 + (u_{U_{CTA}})^2 + (u_{F_L})^2\right]^{1/2} \quad \text{(E-28)}$$

$$u_{C_D} = \frac{W_{C_D}}{C_D} = \left[(u_\rho)^2 + (u_{U_{CTA}})^2 + (u_{F_D})^2\right]^{1/2} \quad \text{(E-29)}$$

The value of the uncertainty of the lift coefficient is determined above; The uncertainty of the drag force coefficient is calculated by substituting the uncertainty of the lift force, density and velocity in equation E-28. Furthermore, the value of the uncertainty of the drag coefficient is determined above; The uncertainty of the drag force coefficient is calculated by substituting the uncertainty of the drag force, density and velocity in equation E-29.

$$u_{C_L} = \frac{w_{C_L}}{C_L} = [(0.011)^2 + (0.05413)^2 + (0.032)^2]^{1/2} = 0.0638 = \%6.4$$

$$u_{C_D} = \frac{w_{C_D}}{C_D} = [(0.011)^2 + (0.05413)^2 + (0.032)^2]^{1/2} = 0.0638 = \%6.4$$